박사 학위논문

Ph. D. Dissertation

스페클 조명과 배열 신호 처리 기법을 이용한 초고해상도 나노현미경 개발

Nanometer Resolution Fluorescence Microscopy using Speckle Illumination and Array Signal Processing

KAIST
한국과학기술원
KOREA ADVANCED INSTITUTE OF SCIENCE AND TECHNOLOGY
SINCE 1971

장 재 덕 (張 在 德 Jang, Jaeduck)

바이오및뇌공학과

Department of Bio and Brain Engineering

KAIST

2011

스페클 조명과 배열 신호 처리 기법을 이용한 초고해상도 나노현미경 개발

Nanometer Resolution Fluorescence Microscopy using Speckle Illumination and Array Signal Processing

KAIST

Nanometer Resolution Fluorescence Microscopy using Speckle Illumination and Array Signal Processing

Advisor : Professor Ye, Jong Chul

by

Jang, Jaeduck

Department of Bio and Brain Engineering

KAIST

A thesis submitted to the faculty of KAIST in partial fulfillment of the requirements for the degree of Doctor of Philosophy in the Department of Bio and Brain Engineering . The study was conducted in accordance with Code of Research Ethics[1].

2011. 05. 11.

Approved by

Professor Ye, Jong Chul

[Advisor]

[1]Declaration of Ethical Conduct in Research: I, as a graduate student of KAIST, hereby declare that I have not committed any acts that may damage the credibility of my research. These include, but are not limited to: falsification, thesis written by someone else, distortion of research findings or plagiarism. I affirm that my thesis contains honest conclusions based on my own careful research under the guidance of my thesis advisor.

스페클 조명과 배열 신호 처리 기법을 이용한 초고해상도 나노현미경 개발

장 재 덕

위 논문은 한국과학기술원 박사학위논문으로
학위논문심사위원회에서 심사 통과하였음.

KAIST

2011년 05월 11일

심사위원장 예 종 철 (인)

심사위원 박 제 균 (인)

심사위원 정 기 훈 (인)

심사위원 최 철 희 (인)

심사위원 민 달 희 (인)

DBIS
20065143

장 재 덕. Jang, Jaeduck. Nanometer Resolution Fluorescence Microscopy using Speckle Illumination and Array Signal Processing. 스페클 조명과 배열 신호 처리 기법을 이용한 초고해상도 나노현미경 개발. Department of Bio and Brain Engineering . 2011. 67p. Advisor Prof. Ye, Jong Chul. Text in English.

ABSTRACT

In this thesis, we focus on the nanometer resolution imaging of cells that are highly transparent. The conventional techniques for cellular imaging exploit inhomogeneities and bio-chemical characteristics of cells for phase and fluorescence microscopy, respectively. Phase microscopy is widely used for qualitative visualization of cellular structures in real time by using the inhomogeneities of height and refractive index without the need for specialized stains or dyes. The inhomogeneities make different optical path length deviation allowing high contrast imaging.

Recently, researchers are interested in quantitative phase microscopy that allows the nanometer accuracy measurements of optical phase length by using interferometric techniques. However, the conventional methods require precise optical alignment due to the heterogenous phase noise. Thus we propose novel self-reference quantitative phase microscopy to minimize the phase noise. We demonstrate the performance of the proposed quantitative phase microscopy using polymer structures and various cells. It is also readily applied to microfluidic devices for cell cultivation.

Additionally, fluorescence microscopy is applied to structural and functional imaging of cells by using staining of fluorescence proteins and dyes. However, the resolution of far-field optical microscopy is limited by diffraction limit. Recent breakthroughs in far-field fluorescence microscopy have achieved nanometer resolution imaging by exploiting non-linear properties of optical elements or fluorescence phenomena. In STED microscopy, two precisely aligned high power laser beams generate an effective nanoscale point spread function, and PALM/STORM applied photoswitchable fluorophores to achieve single molecule localization of high accuracy. These methods have a common principle that a sparse subset of fluorophore is switched on and off. Even though the conventional nanoscopy reach lateral resolution of $10 \sim 20nm$, they have to be applied with extraordinary techniques such as complicated optics, photoswitching molecules and localization algorithms.

Here, we present novel nanometer resolution microscopy using speckle illumination and array signal processing, which does not require photoswitchable fluorescent probes and extraordinary optical systems. If the emission signals from multiple targets are not coherent, then the targets can be resolved by array signal processing techniques. Without photoswitchable probes and specialized optics we can achieve the incoherency of target signals by using dynamic speckle illuminations. By simply modifying the conventional epi-fluorescence microscopy to generate dynamic speckle illuminations, conventional fluorescent dyes and proteins can be imaged at nanometer resolution using a conventional low power CW laser. After enough snapshots are acquired, we can reconstruct a nanometer resolution image. Finally, we

demonstrate the proposed nanometer resolution microscopy using nano-patterns and subcellular structures of cells.

Keywords: Super Resolution, Nanoscopy, Speckle, Array Signal Processing

KAIST

Contents

Abstract i
Contents iii
List of Tables v
List of Figures vi

Chapter 1. Introduction 1

Chapter 2. Quantitative Phase microscopy 6
2.1 Background 6
2.2 Optical setup for quantitative phase microscopy 7
2.3 Experimental results 9
2.4 Discussion 11

Chapter 3. Nanometer Resolution Microscopy (Nanoscopy) 14
3.1 Background 14
3.2 Near-field optical microscopy 14
3.3 Nanoscopy by point spread function engineering 15
3.4 Nanoscopy by stochastic reconstruction 17
3.5 Discussion 20

Chapter 4. Theory of Nano-MUSIC 21
4.1 Nano-MUSIC 21
4.2 Speckle Illumination 24

Chapter 5. Fundamental Limit Characterization of Nano-MUSIC 28
5.1 Cramér-Rao bound 28
5.2 Nano-MUSIC 31

Chapter 6. Experimental Results 34
6.1 Implementation 34
6.2 Methods and Materials 35
6.2.1 Phantom preparation 35
6.2.2 HeLa cell preparation 35
6.3 Reconstruction results 36

KAIST

Chapter 7. Conclusion **55**
7.1 Summary 55
7.2 Future directions 56
7.2.1 Multi-color imaging 56
7.2.2 Multi-dimensional imaging 57
7.2.3 Resolution improvement 60

References **62**

Summary (in Korean) **68**

KAIST

List of Tables

6.1 Specifications of radial nano-patterns 35

7.1 Characteristics of the conventional nanoscopy [67] and Nano-MUSIC 55

KAIST

List of Figures

1.1 General structure of an animal cell. The animal cell as an eukaryotic cell is surrounded by plasma membrane and has nucleus, cytoskeleton and other organelles. 3

1.2 The concept of signal array processing. When the sensor array detects the signal from an emitter such as airplane, we can detect the location of a target by using the array signal processing methods. 4

2.1 (a) In PSI (phase shifting interferometry) setup, SLM (spatial light modulator) with a polarizer (P) and analyzer (A) is used for phase modulation. Here, M3 is mechanically scanned to realize the eDOF (extended depth-of-field) without moving objective lens MO1 or sample. (b) A simple mirror M4 is used for HPM (Hilbert phase microscopy) setup. Due to the image inversion, double interferograms are formed. 8

2.2 Calculated phase maps using our (a) PSI (phase shifting interferometry) and (b) HPM (Hilbert Phase Microscopy) setups. The measurements are obtained without moving objective lens or specimen, but rather by scanning the mirror in the objective arm. The corresponding bright-field images show severe blurring. 10

2.3 Phase maps of a micropatterned PDMS sample using (a) WLSI (white light scanning interferometry), (b) PSI (phase shifting interferometry), and (c) HPM (Hilbert phase microscopy) setup, respectively. (d) Average line profiles of a pattern using various methods. 11

2.4 Experimental results of RBCs using PSI setup: (a) microfluidic device for RBCs, a 100μm scale bar is shown; (b) calculated phase image of the channel with RBCs, (c) 3-D profile of the RBCs within white box in (b), and (d) thickness measurements at horizontal and vertical arrow directions in (c). 12

2.5 Experimental results of RBCs using HPM setup: (a), (b) quantitative phase images from the object and reference images, (c) quantitative phase image from averaging of (a) and (b), (d) a typical phase image from HPM measurement; a 10μm scale bar is shown, and (e) thickness measurements of the arrow directions in (a), (b), and (c). 12

2.6 Experimental results of bovine embryo: (a) a phase contrast image of two cell stage bovine embryo in a microchannel using inverted microscopy (IX71, Olympus). (b) A simultaneously formed double interferogram using our setup. (c) Calculated OPL (optical path length) deviation, and (d) the OPL profile along the white dashed line in (c). 13

KAIST

3.1 The variety of near-field optical microscopy. (a) NSOM with scanning tip of illumination and detection; (b) NSOM with scanning tip and objective lens for illumination and detection, respectively; (c) TIRFM with illumination of prism; (d) TIRFM with the objective lens of illumination and detection. 16
3.2 The optical setup of STED microscopy and the principe of nanoscale effective PSF. The doughnut-shaped STED beam (red) de-excites the fluorescence molecules at the rim of excitation PSF (green). The excited fluorescence molecules emit the fluorescence signals (orange) within nanoscale PSF. 17
3.3 Saturated Structure Illumination Microscopy (SSIM). (a) The generation of a structured illumination pattern; (b) The observable region of a spatial frequency space by conventional microscopy. (c) The illumination pattern for spatial modulation of (b). (d) The extended spatial frequency space of (b) by (c). (e) The observable regions when the total imaging procedure is finished. 18
3.4 PhotoActivation Localization Microscopy (PALM) and STochastical Optical Reconstruction Microscopy (STORM). (a) PALM/STORM reconstruct a super-resolution image by stochastic reconstruction; when weak illumination sparsely switched on individual probes, the detected photon (N) enables the centroid calculation for individual probes. (b) For the given target sample, STORM achieved a super-resolution image by localizing activated sparse subsets of photoswitching probes for total imaging cycles. 19

4.1 Fluorescence emission acquision of PALM/STORM and nano-MUSIC. 21
4.2 The image formation concept of optical microscope system. Comparing to Fig. 1.2, we consider the sensor array and airplanes as camera and fluorescence signals, respectively. . 22
4.3 Simplified illumination optical geometry. The distances **b** and **f** are back focal length and front focal length, respectively. Such simplified optics represents modified Köller illuminator for a speckle field. 24
4.4 The normalized correlation function $\boldsymbol{\mu}_e(\Delta\alpha, \Delta\beta)$ for several different roughness of diffusor. 26
4.5 Measured speckle patterns and their characteristics. (a) Measured speckle patterns for 1000 snapshots, (b) and (c) mean and correlation matrix of measured speckle patterns, (d) averaged off-diagonal elements along with diagonal elements of (c). 27

6.1 The proposed optical system of modified epi-fluorescence microscopy. (a) The implementation of nano-MUSIC on conventional epi-fluorescence microscopy. (b)An excitation laser (S) is scattered by the diffusor (D1) in front of illumination optics (L1-L3), and then the scattered light is focused on the sample plane by the objective lens (O). The emission fluorescence signal is going back through the dichroic mirror (F2) and emission filter (F3) set and also magnified with the tube lens (L4) in front of the detector (D2). 40

KAIST

6.2 Experimental result of silica nano-particles with RITC. (a-c) SEM, conventional, and nano-MUSIC images of phantom 1, respectively, (d-f) blue and red line profiles represent line numbers 1-3 in (b) and (c), respectively. Scale bars in (a-c) are $200nm$. 41
6.3 Experimental result of silica nano-particles with RITC. (a-c) SEM, conventional, and nano-MUSIC images of phantom 2, respectively, (d-f) line profiles represent line numbers 1-3 in (c), respectively. Scale bars in (a-c) are $200nm$. 41
6.4 Experimental result of silica nano-particles with RITC. (a-c) SEM, conventional, and nano-MUSIC images of phantom 3, respectively. Scale bars in (a-c) are $200nm$. 42
6.5 Experimental result of silica nano-particles with RITC. (a-c) Conventional, nano-MUSIC, and SEM images of randomly scattered nano particles, (d-f) magnified images of the white line box in (a-c), respectively, (g) line profile of dashed lines in (d) and (e). Blue and red lines represent conventional and nano-MUSIC results, respectively. The FWHM of the single particle is measured $\sim 90nm$ where the real size of this particle is $\sim 100nm$ in SEM image (f). Scale bars in (a-b) and (d-e) are $2\mu m$ and $500nm$, resepectively. 43
6.6 Experimental result of a nano pattern with a minimum distance (m) of $120nm$. (a-c) Conventional, nano-MUSIC, and SEM images, respectively, (d-e) arc profiles along the character 1-2 in (a) and (b). Red and blue lines are conventional and nano-MUSIC profiles, respectively. Scale bars in (a-b) are $1\mu m$ 44
6.7 Experimental result of a nano pattern with a minimum distance (m) of $80nm$. (a-c) Conventional, nano-MUSIC,SEM images, respectively, (d-e) arc profiles along the character 1-2 in (a) and (b). Red and blue lines are conventional and nano-MUSIC profiles, respectively. Scale bars in (a-b) are $1\mu m$ 44
6.8 Experimental result of a nano pattern with a minimum distance (m) of $60nm$. (a-c) Conventional, nano-MUSIC, SEM images, respectively, (d-e) arc profiles along the character 1-2 in (a) and (b). Red and blue lines are conventional and nano-MUSIC profiles, respectively. Scale bars in (a-b) are $1\mu m$ 45
6.9 Structures of smooth and rough endoplasmic recticulum consist of ER cisternae, ER lumen, and ribosomes. 45
6.10 A mitochondrion structure consist of outer and inner membrane, inter-membrane space, and matrix. 45
6.11 The experimental result of F-actin stained with a fluorescent dye. (a) Conventional image generated by a mean image of measured snapshots. (b) Confocal image of (a). (c) l_∞-MUSIC reconstruction image of (a). (d) l_2-MUSIC reconstruction image of (a). The white boxes in (a-d) are magnified in the inset images of (a-d). Scale bars in (a-d) and insets of (a-d) are $10\mu m$ and $1\mu m$, respectively. 46

6.12 The experimental result of F-actin in filopodia stained with a fluorescent dye. (a) Conventional image generated by a mean image of measured snapshots. (b) l_∞-MUSIC reconstruction image of (a). (c) l_2-MUSIC reconstruction image of (a). The white boxes in (a-c) are magnified in the inset images of (a-c), respectively. Scale bars in (a-c) and insets of (a-c) are $2\mu m$ and $500nm$, respectively. 47

6.13 The experimental result of ER stained with a fluorescent dye. (a) Conventional image generated by a mean image of measured snapshots. (b) l_∞-MUSIC reconstruction image of (a). (c) l_2-MUSIC reconstruction image of (a). (d-f) Magnified images of the white line boxes in (a-c). (g-i) Magnified images of the white dash line boxes in (a-c). Scale bars in (a-c) and (d-i) are $2\mu m$ and $500nm$, respectively. 48

6.14 The experimental result of ER stained with a fluorescent protein (DsRed-ER). (a) Conventional image generated by a mean image of measured snapshots. (b) l_∞-MUSIC reconstruction image of (a). (c) l_2-MUSIC reconstruction image of (a). (d, f, and h) Magnified images of the white line boxes in (a-c). (e, g, and i) Magnified images of the white dash line boxes in (a-c). Scale bars in (a-c) and (d-i) are $2\mu m$ and $500nm$, respectively. 49

6.15 The experimental result of mitochondria stained of Tom20 with a fluorescent dye. (a) Conventional image generated by a mean image of measured snapshots. (b) l_∞-MUSIC reconstruction image of (a). (c) l_2-MUSIC reconstruction image of (a). (d-f) Magnified images of the white line boxes in (a-c). (g-i) Magnified images of the white dash line boxes in (a-c). Scale bars in (a-c) and (d-i) are $2\mu m$ and $500nm$, respectively. 50

6.16 The experimental result of mitochondria stained of inner membrane with a fluorescent protein (DsRed-mito). (a) Conventional image generated by a mean image of measured snapshots. (b) l_∞-MUSIC reconstruction image of (a). (c) l_2-MUSIC reconstruction image of (a). (d, f, and h) Magnified images of the white line boxes in (a-c). (e, g, and i) Magnified images of the white dash line boxes in (a-c). Scale bars in (a-c) and (d-i) are $2\mu m$ and $500nm$, respectively. 51

6.17 The experimental result of mitochondria stained of cytochrome-c with a fluorescent dye. (a) Conventional image generated by a mean image of measured snapshots. (b) Confocal image of (a). (c) l_∞-MUSIC reconstruction image of (a). (d) l_2-MUSIC reconstruction image of (a). (d-g) Magnified images of the white line boxes in (a-d). (h-k) Magnified images of the white dash line boxes in (a-d). Scale bars in (a-d) and (d-k) are $2\mu m$ and $500nm$, respectively. 52

6.18 The experimental result of F-actin stained with a fluorescent dye. (A-E) Conventional image from $1\mu m$ z-axis scanning. (F-J) Conventional image generated by variance from $1\mu m$ z-axis scanning. (K-O) l_2-MUSIC reconstruction image of (A-E). 53

6.19 The experimental result of F-actin stained with a fluorescent dye. (A-C) Conventional image generated by mean of stack images. (D-F) Projection image generated by maximum of stack images. 54

7.1 (a) STED needs four color laser systems to acquire two-color images, (b) PALM/STORM needs two-color laser systems for a single fluorescence color image. 57

7.2 Nano-MUSIC system can further extends to multi-color, multi-dimension and real-time imaging systems. Moreover, by exploiting near-field illumination optics such as TIRFM, we can improve the resolution of the system. 58

7.3 (a) Objective lens type of TIR illumination, (b) the normalized intensity along with perpendicular distance from glass surface. If we exploit the TIRFM instead of far-field optical system in Fig. 7.2, the effect of signal correlation matrix should be reduced in the nano-MUSIC. 60

KAIST

Chapter 1. Introduction

At the beginning of optical microscopy in the 17th century, Robert Hooke [1] and Antonie van Leeuwenhoek [2] introduced compound and single lens optical imaging systems, respectively. Using those techniques, Van Leeuwenhoek could resolve a structure as small as $1\mu m$. Their optical system could only describe a microscopic appearance of a stained object. In 1930s, Fritz Zernike published a description of a method coined 'phase contrast (PhC)' that transforms the phase difference between diffracted light and un-diffracted light due to the inhomogeneity of a sample [3]. The most recent microscopy still incorporates this system that allows *in-vivo* imaging without the need for specialized staining or dyes. After that, an alternative technique coined 'differential-interference contrast (DIC)' was designed for high resolution and high contrast imaging of unstained and living cells and organisms [3]. Similar to PhC microscopy, DIC microscope system exploits the phase differences of two slightly separated beams that are passed through a sample depending on its optical density. The merit of DIC is in overcoming the 'halo' artefact in phase contrast images. This system is also called Nomarski microscopy since Nomarski set up the theoretical basis for modern DIC microscope system. The PhC and DIC systems are the techniques relevant to qualitative phase microscopy. They are well established in commercial microscopy with simple optical systems nowadays. However, recently quantitative phase microscopic imaging methods are introduced based on interference or holography techniques [4, 5, 6, 7, 8].

In the early 20th century August Köhler found out that certain objects emitted light of longer wavelength than incident light (UV) [9], and then in 1911, Oskar Heimstädt [10] used this result as the basis of the first (auto) fluorescence microscopy that uses a dark-field illumination technique to avoid incident light. In the next two decades, Max Haitinger applied the exogenous fluorescent chemical probes coined 'fluorochrome' to induce fluorescence in tissues [9]. Even though the prototype of the epi-fluorescence microscopy was introduced by Philipp Ellinger and August Hirt using a series of traditional filters [11], the modern epi-fluorescence microscope system was introduced in 1960s by Johan S. Ploem based on the dichromatic mirror without the absorption of incident light [12]. After such fluorescence microscopy based on a dichromatic mirror was established, the epi-fluorescence microscope system became a universal tool for biologist. However, the invention of Albert Coons in 1941 became a major development in fluorescence microscopy, which is known as the immuno-fluorescence staining [13]. Following the invention of immuno-fluorescence staining, the interest of cell biologist moved from tissue to sub-cellular level, and the system is still applied for sub-cellular imaging systems nowadays. Moreover, the discovery of green fluorescent protein (GFP) in 1962 by Shinomura and colleagues was a breakthrough for *in-vivo* imaging of bacteria and cells. According to M. Chalfie's report, GFP was expressed from the promoter of a gene, and its spatial and temporal expression in specific proteins mimicked the endogenous gene ex-

pression [14]. Thus, GFP became a reliable marker for monitoring specific protein patterns. Multi color images were acquired by many researchers by modifying GFP to emit blue, cyan and yellow fluorescence light except red and orange. Finally, in 1999, red fluorescence protein (RFP) was discovered from coral and Anthozoa species [15], and photoactivated or photoconverted fluorescent proteins were introduced with switching operation, which led to nanometer resolution imaging techniques later. The fluorescence image sometimes encountered with unwanted signals coming from out-of-focus planes, which negated the resolution achievement. The focused excitation light not only excites the fluorescence molecules in a focal plane but also the molecules in a defocused plane simultaneously since all molecules within the light pathway are affected. Confocal microscopy avoids such a problem by matched pinholes placed in illumination and detection optics, which restricts both the field of illumination and the light reaching the objective to a single point at an in-focus plane. Thanks to the confocal system we can clearly observe the sub-cellular process and reduce the need of tissue sectioning. Together with confocal microscopy and the discovery of fluorescence proteins, we can observe the inner structure of living cells clearly.

Even though the conventional optical microscope systems ushered in an era of unstained real time imaging and sub-cellular imaging of cells, the biological information conveyed by optical microscopy is still restricted by physical limitations since the light passing through the finite size of a lens is diffracted, corrupting spatial resolution. Hence, far-field optical microscopy cannot visualize sub-cellular structures below the diffraction limit, also known as Abbe's criterion ($\lambda/2\mathrm{NA}$) [16].

As shown in Fig. 1.1, the whole size of an animal cell is $10 \sim 100\mu m$, and the diameter of nucleus and mitochondria are $1 \sim 10\mu m$ and $0.2 \sim 1\mu m$, respectively. Organelles of those size can be resolved by optical microscopy. However, other organelles such as ribisomes and endoplasmic reticulum are smaller than the diffraction limit ($< 200nm$) and cannot be resolved by optical microscopy. Typically, the exact structures of organelles and molecules are revealed by electron microscopy with the resolution of $0.1 \sim 0.2nm$. However, to use electron microscopy, we need specialized preparation sequence such as fixation and microtome, so this method cannot acquire *in-vivo* imaging and functional imaging. Thus, recently, scientists are concentrating on breaking the diffraction limit of optical microscopy based on non-linear imaging physics.

For the last decade, nanometer resolution microscopy coined 'nanoscopy' have been developed to overcome the diffraction limit. These microscopy exploit the non-linearity within imaging physics. For example, in STED microscopy [17], the STED beam consists of Gaussian and doughnut shaped patterns that are aligned on-axis, which take the roles of excitation and de-excitation beams for photoswitching of fluorophores, respectively. Applying the aligned STED beam to fluorescence tagged samples, this nanoscopy technique generates nanoscaled effective point spread function (PSF) de-exciting the outer fluorophores of the Gaussian beam. The resolution of STED is determined by the intensity of STED beam. Hence, a super resolution ($10 \sim 20nm$) image can be obtained without additional mathematical processing in STED. In structure illumination microscopy (SIM) [18], an interference pattern generated

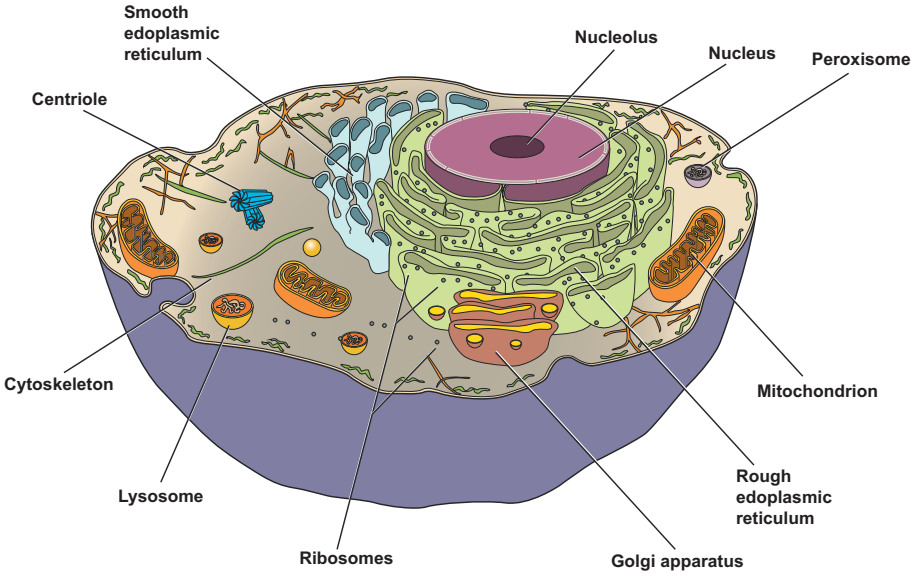

Figure 1.1: General structure of an animal cell. The animal cell as an eukaryotic cell is surrounded by plasma membrane and has nucleus, cytoskeleton and other organelles.

by interferometry is illuminated on a sample, which shifts the spatial frequency of optical system. By combining the images from multiple shifts, we can increase the numerical aperture and reduce effective PSF. The resolution of SIM is claimed not limited; however it is limited ($\sim 100nm$) in practice since the spatial frequency of the pattern is limited by optical resolution.

In single molecule imaging, the localization methods such as Gaussian model approximation [19, 20, 21] and statistical signal processing [22, 23] provide sub-diffraction resolution. These methods calculate the centroid of individual molecules in the sequence of fluorescence images using conventional microscopy. Although the localization methods located well the centroid of single molecules within sub-diffraction limit, they have some limitations in the application of aggregated molecules especially when resolving the in axial and lateral directions, and also the statistical methods can be implemented using specific probes such as quantum dot due to its blinking statistics. Recently, advanced single molecule imaging methods such as photoactivation localization microscopy (PALM) [24] and stochastic optical reconstruction microscopy (STORM) [25] are introduced to overcome the diffraction limit by separating the unresolved individual molecules temporally using specially designed probes. More specifically, for each imaging frames, the subset of fluorophores is achieved by excitation, localization and de-excitation of individual photoswitchable fluorophores. Similar to conventional single molecule imaging it then localizes the centroid of fluorescent signals for each imaging cycle, and finally the overall image provides a super resolution ($< 20nm$) fluorescence image. However, the applications of PALM/STORM are not general since these are based on the non-linear imaging physics of photoswitches. In most of biological experiments, non-switchable fluorescent materials are frequently used for sub-cellular organelles in monitoring and visualizing with conventional fluorescence microscopy. Thus for widespread use of super

resolution microscopy as an everyday investigation method, a more simplified hardware and software systems are required.

Until now we briefly reviewed on conventional microscopy and nanoscopy. Thanks to the phase microscopy (PhC and DIC), we can see the biological phenomena in living cells. However, they does not provide quantitative information due to their imaging physics. Thus recently researchers are proposed quantitative phase microscopy [4, 5, 6, 7, 8] based on interferometry and holography. In fact the accurate measurement of phase delay is connected directly with the structural information, however conventional methods are very sensitive to optical alignment. Thus we propose a novel self-reference quantitative phase microscopy that minimizes heterogeneous phase noise. Based on modified Michelson interferometry, the self-reference field can be generated by inverting the relative position of the specimen and background. Furthermore, the system can be readily implemented Hilbert phase microscopy and phase shift interferometry. The performance of this system is verified using polymer beads, micro-pattern and embryo cells.

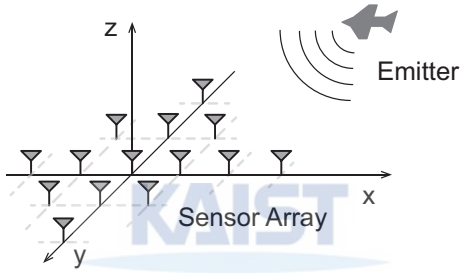

Figure 1.2: The concept of signal array processing. When the sensor array detects the signal from an emitter such as airplane, we can detect the location of a target by using the array signal processing methods.

In this thesis, we show that sensor array signal processing algorithms used for radar target detection problem as shown in Fig. 1.2 are very useful for nanoscopic imaging. It has been mathematically shown that if the scattered waves from the two targets are not coherent, the two targets can be resolved using various techniques such as maximum likelihood method, subspace methods and so on [26, 27, 28, 29, 30, 31]. Furthermore, mathematical analysis based on Cramér-Rao bound discovered that the achievable resolution from the uncorrelated multiple sources is exactly the same as that of detecting single target without any interfering background target [28]. Since the Cramér-Rao bound from a single target determines the ultimate resolution that can be achieved using the sensor systems, this implies that the same best resolution can be achieved even with multiple sources as long as they are uncorrelated [28, 30]. Since the fluorescence emission from photo-switching probes are not overlapped in time; so they are uncorrelated. Hence, the mathematical theory of sensor array signal processing gives a renewed insight of PALM/STROM why they can achieve the same best resolution by the single molecule imaging using the photo-switching probes. Similar conclusion can be made for the super-resolution microscopy that are based on blinking statistics of quantom-dots [22], as long as the blinking statistics are uncorrelated

to each other.

As a routine work of nanoscopy to cell biologist, a nanometer resolution imaging modality for conventional bio-chemical experimental protocols should be implemented. For conventional experimental protocols and instruments, we propose a novel nanoscopy. This thesis realizes this by speckle illumination scheme using standard fluorescence molecules and by array signal processing technique.

We are aware that speckle phenomena have been exploited from various aspects in microscopy. Waterman-Storer and Salmon [32, 33] discovered that the fluorescence emission signals of microtubules appeared as speckled light when X-rhodamin tubulin is injected into cells. This method is extended with a variety of labelling methods and microscope systems [34] and applied for researches on dynamics and movements of microtubules and actin [35, 36]. Speckle illumination was also implemented for optical sectioning and quasi-confocal microscopy [37, 38, 39, 40], since the speckle fields between in-focus and out-of-focus planes are uncorrelated. However, our approach is fundamentally different from these approaches where the spatial incoherency of speckle illumination is exploited to achieve nanometer resolution.

One limitation of the proposed approach in generating uncorrelated source statistics is that the span of spatial incoherency is usually restricted by the full-width at half-maximum of the squared point spread function of the illumination unit. This is because the perfectly incoherent speckle fields become blurred as they pass through the illumination optics. However, such a limitation can be effectively reduced using l_∞-MUSIC algorithm, which has been developed by modifying the popular MUSIC algorithm in array signal processing to improve the robustness. By utilizing spatially incoherent speckle illumination and the proposed array processing algorithm, we can demonstrate that the sub-diffraction resolution can be easily achieved using conventional fluorescence probes and proteins.

The contents of this dissertation are as follows. In Chapter 2, we explain the quantitative phase microscopy that are advanced phase microscopy techniques, and then, in Chapter 3 we briefly review on conventional nanometer resolution imaging schemes. In Chapter 4 and 5, we explain the theoretical basis and fundamental limit of the proposed nanoscopy, and in Chapter 6, the implementation and experimental results of the proposed nanoscopy are introduced. We verify the proposed nanoscopy by using experimental results of phantoms and cells in Chapter 6. Finally, in Chapter 7, we summary of the proposed nanoscopy and introduce the further extension of proposed nanoscopy.

Chapter 2. Quantitative Phase microscopy

2.1 Background

Phase microscopy is commonly used to visualize transparency samples without the assistance of exogenous contrast agent. Due to inhomogeneous refractive index in the sample and background, the phase information reflects the optical path length (OPL) of the transmitted light through a sample. Phase contrast (PhC) and differential interference contrast (DIC) have traditionally been used to obtain phase contrast by changing OPL using specialized optical components. For example, the phase contrast (PhC) microscopy introduced by Zernike [3] utilizes the phase plate which is mounted at the back focal plane of the objective lens to enhance the difference of the scattered and unscattered light. Moreover the differential interferometry contrast (DIC) microscopy introduced by Nomarski [3] applies the interfered phase difference between two polarized light by use of Wollaston prisms placed at illumination and detection optics. At illumination optics, Wollaston prism is placed at the front focal plane of the condenser lens, and splits the incident light into s- and p-polarized beams which have slightly different beam paths on the specimen by a condenser lens. Finally the split beams are combined at the back focal plane of the objective lens by the 2nd Wollaston prism. Since the s- and p-polarized light have slightly different OPL, the combined and interfered light transforms the difference of refractive index or thickness property into a contrast image. However, these types of conventional phase microscopy fail to measure the quantitative phase image.

Recently, several quantitative phase microscopes (QPM) have been extensively applied in biological research areas [4, 5, 6, 7, 8, 41]. Fourier phase microscopy (FPM) applies the principle of PhC microscopy and phase shifting interferometry (PSI) [4]. The programmable phase modulator (PPM) is used to control the phase of the scattered light from a sample with respect to unscattered light. In the case of Hilbert phase microscopy (HPM), the optical system delivers light using an optical fiber to minimize the phase noise, and Hilbert transform reconstruction improves the temporal resolution up to a few milliseconds using a single interferogram recording [5]. Surface plasmon resonance (SPR) technique is also integrated with QPM to quantify the phase profile of DNA microarray [42]. Digital holographic microscopy (DHM) allows three dimensional imaging based holography [7]. Many QPMs generate interferograms using an isolated reference field from non-scattered light through separate optical paths. To remove heterogeneous phase noise due to distinct beam paths, diffraction phase microscopy (DPM) [8] splits a specimen image with a diffraction grating through which the first order diffracted field becomes the object field, whereas the zeroth order field is used as the reference field.

We also develop a novel self-reference interferometry especially suitable for monitoring microfluidic

devices. Our system uses the light through the non-channelized areas of microfluidic devices as a reference field. More specifically, using Michelson interferometry, incident beams through the channel and non-channel areas are split onto the reference and the object arms (Figs. 2.1(a) and (b)). Unlike conventional Michelson interferometry, the 2nd objective lens is used for imaging inversion optics in the object arm. Since the reference arm and the object arm switch the relative position of the specimen and the homogeneous background, a double interferogram can be obtained as shown in insets of Fig. 2.1(a)(b). Two distinct setups, PSI and HPM, can be readily implemented by changing the reflection optics in the reference arm. In the PSI setup, a reflection type SLM (Spatial Light Modulator) controllably shift the phase of the reference fields (Fig. 2.1(a)). The main advantage is to replace the scanning of the objective lens or the specimen with a mirror scanning in the object arm to facilitate the increase of the depth-of-field [43]. This increased depth-of-field is especially important in such applications with limited working distance between objective lens and specimen. In the HPM setup, a simple mirror is used instead of SLM (Fig. 2.1(b)). Since our setups form double interferograms simultaneously, a higher signal-to-noise ratio (SNR) phase map can be obtained by averaging the two phase reconstructions. Even though our system has the limitation of smaller field-of-view (FOV), it is still suitable for monitoring microfluidic devices since microfluidic devices usually have a wide non-channelized area compared with the microchannel.

2.2 Optical setup for quantitative phase microscopy

KAIST

Figures 2.1(a)(b) illustrate the PSI and HPM setups for our experiment. Two types of 40× objective lens (0.55 and 0.75 NA) and a 100× objective lens (1.30 NA) are used at MO1. To implement the eDOF optics, a pair of objective lenses (MO1 and MO2) with identical tube lenses (L1 and L2) are used. In the object arm, the MO2 (M=20×, 0.5 NA) inverts the relative position of the specimen and background images. In the reference arm, SLM (LC-R 2500, Holoeye) is used for the PSI setup, whereas a mirror (M4) is used for the HPM setup. The phase of the reflected light from the SLM is shifted in $0 \sim 2\pi$ with the 8 bit resolution. To acquire phase shifts, the gray level of the SLM is controlled by an external computer interface, and the polarizer and the analyzer convert the gray level variation into phase shifts. In the HPM setup, the polarizer (P) and analyzer (A) are not necessary. A CMOS detector (450D, Canon) of 4272×2848 pixels with $5.2\mu m$ pitch has been used. The focal length of the adaptor lens (L3) is $200mm$.

The CMOS measurement is then described as follows

$$I_i(x) = |I_R|^2 + |I_O|^2 + |I_R I_O| \cos(q(x) + \Delta\phi(x) + \delta_i), \tag{2.1}$$

where I_R and I_O are the reference and object fields, respectively; and $q(x)$ is the spatial modulation pattern controlled by the tilting angle of each arm. In Eq. (2.1), δ_i's correspond to the phase shifts due to the SLM or the mirror. In the PSI setup, the conventional multiple step phase shift algorithm is used

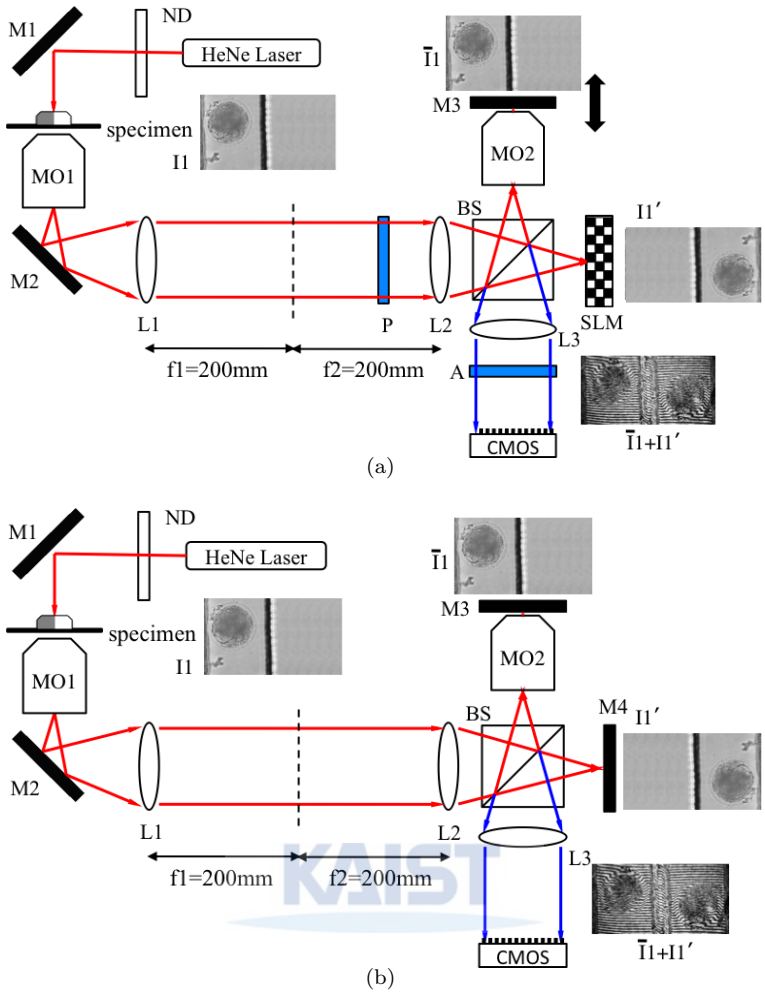

Figure 2.1: (a) In PSI (phase shifting interferometry) setup, SLM (spatial light modulator) with a polarizer (P) and analyzer (A) is used for phase modulation. Here, M3 is mechanically scanned to realize the eDOF (extended depth-of-field) without moving objective lens MO1 or sample. (b) A simple mirror M4 is used for HPM (Hilbert phase microscopy) setup. Due to the image inversion, double interferograms are formed.

as

$$\Delta\phi = \tan^{-1}\left[\frac{I_4(x) - I_2(x)}{I_3(x) - I_1(x)}\right] - q(x), \tag{2.2}$$

where using the four phase shifts $\{\delta_i\}_{i=1}^4 = \{0, \frac{1}{2}\pi, \pi, \frac{3}{2}\pi\}$ [4]. In the HPM setup, a single phase shift $\delta_1 = 0$ is needed, and the phase is calculated based on the Hilbert transform [5]:

$$z(x) = \frac{1}{2}\tilde{I}_1(x) + i\frac{P}{2\pi}\int \frac{\tilde{I}_1(x')}{x - x'}dx', \tag{2.3}$$

where $\tilde{I}_1(x')$ is obtained by removing the low spatial frequency background signal [5]. The phase measurement is then calculated by taking

$$\Delta\phi = \tan^{-1}\frac{Im[z(x)]}{Re[z(x)]} - q(x), \tag{2.4}$$

where $z(x)$ is complex value. Since our setup forms double interferograms simultaneously, two phase maps

can be calculated. Therefore, the phase noise can be reduced by averaging the two phase reconstructions.

2.3 Experimental results

We first verify the eDOF performance of our system. The diameter of the $3\mu m$ polystyrene bead (n=1.59) is measured using the PSI setup with a 100X (NA=1.30) objective lens (MO1). The bead mixed by PDMS is placed between two cover slides. Figure 2.2 illustrates the quantitative phase images when the beads are located at various distances from the focal plane of the objective lens. At the out-of-focus locations, the bright-field images from the 100X objective lens are severely blurred as shown in the image inset of Fig. 2.2. However, thanks to the eDOF optics, the diameter of the bead is measured at about $3\mu m$ at every distance, even without scanning the objective lens or the specimen, and the corresponding phase maps are quantitatively accurate. The calculated maximum height of the bead also confirmed the reliability of the phase map at various distances.

Next, we measured the micropatterned array fabricated by the PDMS molding technique [44]. A mixture of PDMS and curing agent (Sylgard 184, Dow Corning, MI) in a ratio of 10:1 was poured onto the patterned structure, and was removed it after curing. The height of the pattern is $1 \pm 0.1\mu m$, found with the atomic force microscopy (AFM) (XE120, PSIA) and white light scanning interferometry (WLSI) (PWM-T250, Pemtron). We measure the thickness of the sample using the formula: $h(x, y) = \Delta\phi \frac{\lambda}{2\pi\Delta n}$, where$\Delta$ n is the refractive index difference. Here, the refractive index of PDMS is 1.4 [45]. The calculated phase images in Figs. 2.3((b) and (c)) are acquired using the phase unwrapping algorithm described in [46], after the subtraction of the background image using 2-D weighted polynomial fitting. The thickness profiles are shown in Fig. 2.3(d), which illustrates that our measurements are within the range of WLSI and AFM measurements.

We also applied our system for the monitoring of red blood cells (RBCs) in microfluidic devices. Note that a microfluidic device is commonly developed for cell culturing or as analysis, and that people are interested in real-time monitoring of samples [47, 48], since the staining process often disturbs the continuous cultivation or analysis of a cell for a prolonged period of time. The RBCs samples were obtained from the Republic of Korea National Red Cross Organization (Daejeon, Korea) in compliance with safety regulations. Using the aforementioned PSI and HPM methods, we acquired the phase image of RBCs as shown in Figs. 2.4 and 2.5. In Fig. 2.4(a), the FOV of specimen image contains the microchannel area with non-channelized area. RBCs diluted by phosphate buffered saline (PBS) solution are injected into the microchannel. Then, the black box area (denoted by A in Fig. 2.4(a)) above the microchannel is used as the reference field, whereas the black box area denoted by B corresponds to the specimen area in the microchannel. In PSI results, the phase map of the white box in Fig. 2.4(b) is shown in Fig. 2.4(c). The thickness profiles in Fig. 2.4(c) along two arrow directions are shown in Fig. 2.4(d). In

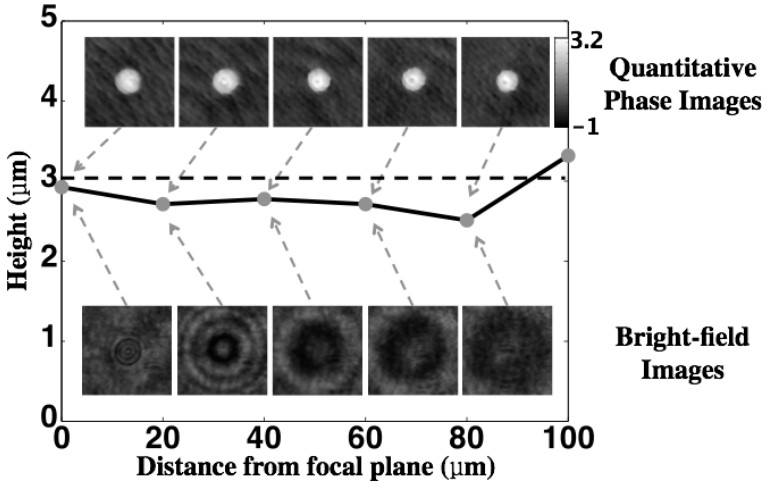

(a)

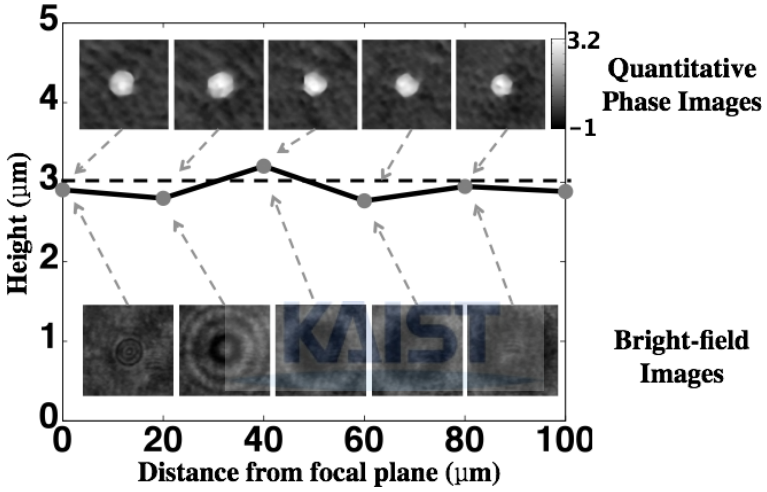

(b)

Figure 2.2: Calculated phase maps using our (a) PSI (phase shifting interferometry) and (b) HPM (Hilbert Phase Microscopy) setups. The measurements are obtained without moving objective lens or specimen, but rather by scanning the mirror in the objective arm. The corresponding bright-field images show severe blurring.

HPM results, Figs. 2.5((a) and (b)) illustrate the reconstruction results using the measurement of sample and reference areas, respectively, whereas Fig. 2.5(d) illustrates the thickness profiles along the arrow directions in Figs. 2.5(a-c). Due to the averaging, the phase noise is significantly reduced in Fig. 2.5(c). The refractive index of the surrounding media and the RBCs were set to $n_m = 1.34$ and $n_{cell} = 1.40$, respectively [49]. The measured phase maps of the RBCs coincides with that found in the literatures (approximately $2\mu m$ in human) [5, 8, 50].

Finally, Fig. 2.6(a) illustrates the microfluidic device for cultivation of a fertilized bovine embryo [51]. The microchannel is filled by PBS for cultivation of bovine embryo. The width of the microchannel is $180\mu m$, and the diameter of the bovine embryo is similar to the size of the microchannel. Figure 2.6(b) illustrates a typical double interferogram measurement from our setup. Compared with the phase contrast

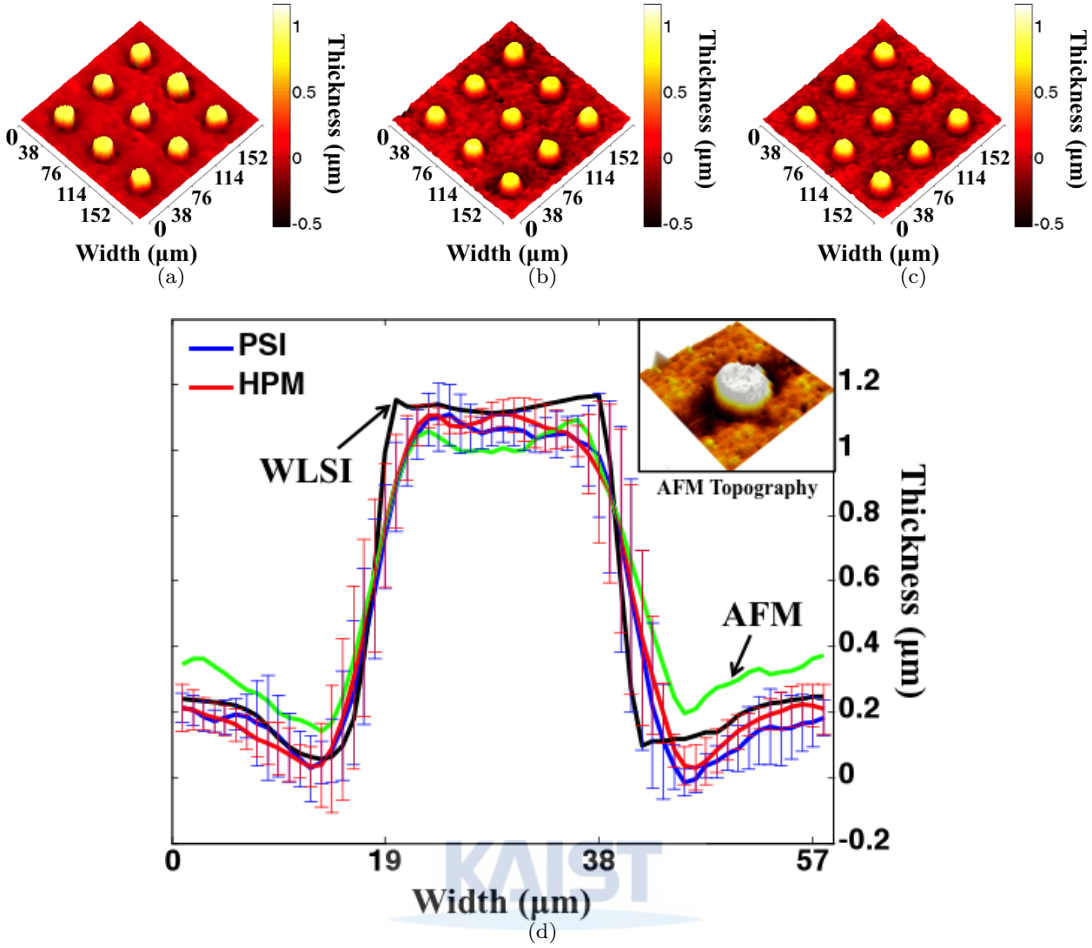

Figure 2.3: Phase maps of a micropatterned PDMS sample using (a) WLSI (white light scanning interferometry), (b) PSI (phase shifting interferometry), and (c) HPM (Hilbert phase microscopy) setup, respectively. (d) Average line profiles of a pattern using various methods.

image in Fig. 2.6(a), the quantitative phase image from the PSI setup in Fig. 2.6(c) reveals the 3D morphology as well as the OPL deviation more clearly. Figure 2.6(d) illustrates the profile along the white dashed line in Fig. 2.6(c) corresponding to the zona pellucida that surrounds the embryo for developing cells. The OPL deviations of the zona pellucida and the single cell were reported previously for the case of a mouse embryo [52]. However, we are not aware of any results for bovine embryos. The height deviations of the measured OPL deviations in Fig. 2.6(d) are slightly higher than the previous reported result for a mouse embryo, which may reflect different embryo sizes between species.

2.4 Discussion

We developed a novel quantitative phase microscopy based on the extended depth-of-focus. The modified Michelson interferometry splits the measured specimen image onto the reference arm and the object arm. The additional microscope objective lens switches the specimen image in the object arm, and then the homogenous background area in the specimen image was used as self-reference field. Si-

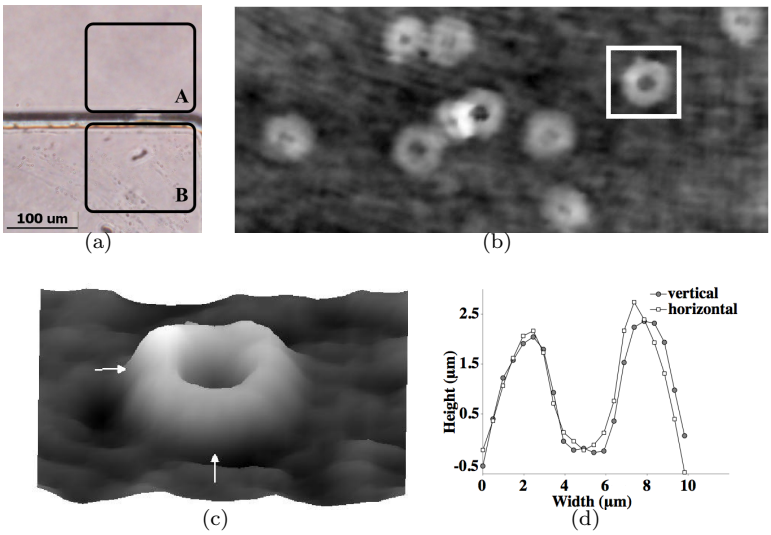

Figure 2.4: Experimental results of RBCs using PSI setup: (a) microfluidic device for RBCs, a 100μm scale bar is shown; (b) calculated phase image of the channel with RBCs, (c) 3-D profile of the RBCs within white box in (b), and (d) thickness measurements at horizontal and vertical arrow directions in (c).

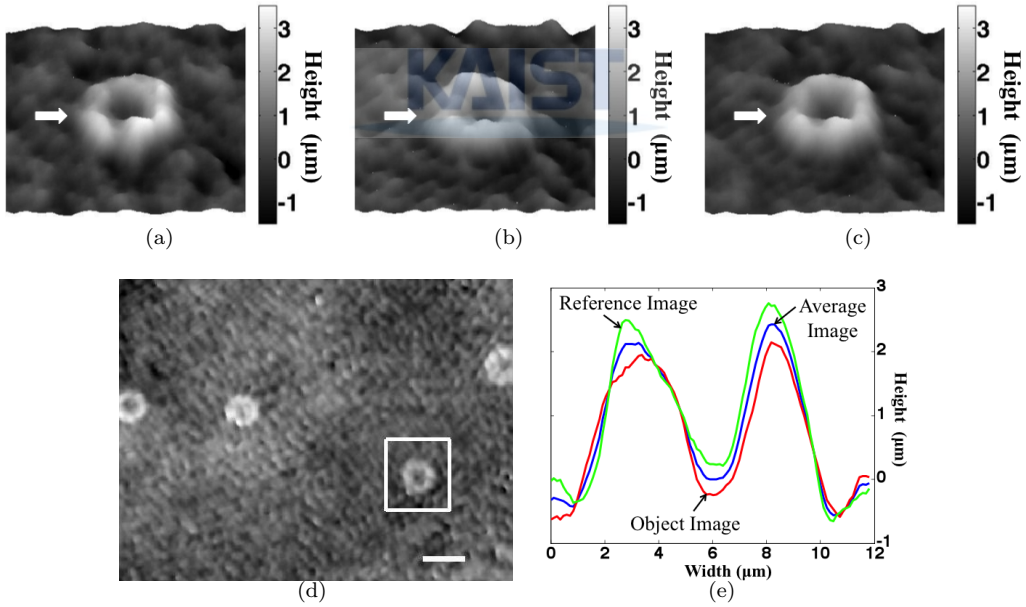

Figure 2.5: Experimental results of RBCs using HPM setup: (a), (b) quantitative phase images from the object and reference images, (c) quantitative phase image from averaging of (a) and (b), (d) a typical phase image from HPM measurement; a 10μm scale bar is shown, and (e) thickness measurements of the arrow directions in (a), (b), and (c).

multaneously, a pair of objective lens increases the depth-of- field thanks to the extended depth-of-focus optics. Using the proposed quantitative phase microscopy, we achieved phase shifting interferometry and Hilbert phase microscope systems, simultaneously. The quantitative phase image is also acquired

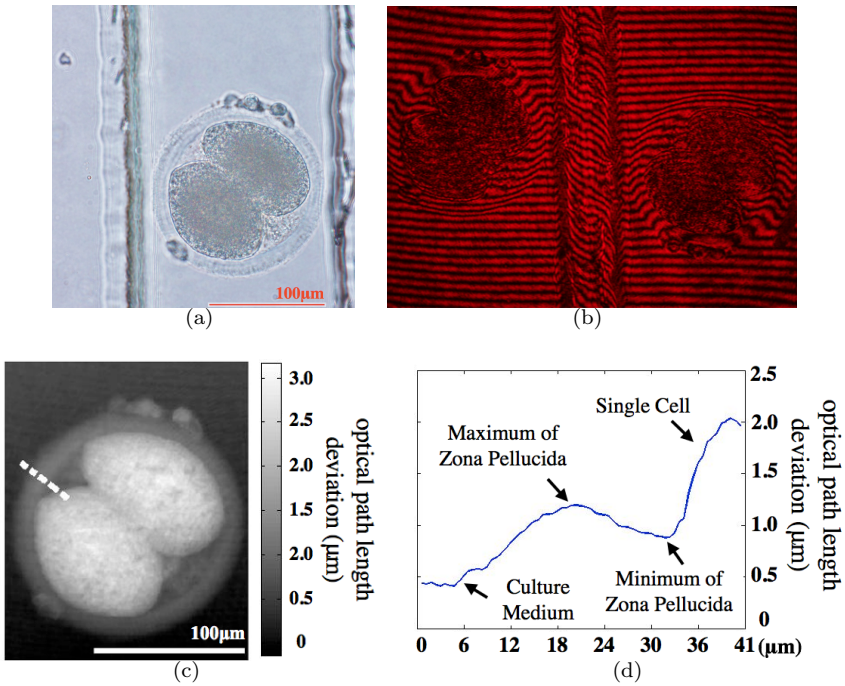

Figure 2.6: Experimental results of bovine embryo: (a) a phase contrast image of two cell stage bovine embryo in a microchannel using inverted microscopy (IX71, Olympus). (b) A simultaneously formed double interferogram using our setup. (c) Calculated OPL (optical path length) deviation, and (d) the OPL profile along the white dashed line in (c).

KAIST

by both systems. Moreover, our system is suitable for microfluidic device, since the device has wide non-channelized area and the target sample is far away from objective lens. The proposed method is confirmed by polystyrene beads, red blood cells, and bovine embryo cells in microfluidic device.

Chapter 3. Nanometer Resolution Microscopy (Nanoscopy)

3.1 Background

The far-field fluorescence microscopy cannot visualize the sub-cellular structure of biological cells even though we labeled its specific target proteins, since Abbe's criterion[16] (λ/2NA) is valid in this region. For the last decade, far-field nanometer resolution fluorescence microscopy operating beyond the diffraction limit have been extensively investigated. These methods are implemented on different hardware and software systems such as complicated optics, advanced fluorescent techniques, and signal processing. The fundamental principle of diffraction unlimited resolution is based on non-linearity which is originated from switching of fluorophore states as well as excitation optical techniques. Meanwhile, in near-field imaging, the diffraction limit does not affect the achievement of a sub-diffraction image, and the near-field optical microscopy has become a single molecule illumination technique as a part of some nanoscopy.

KAIST

3.2 Near-field optical microscopy

Near-field optics exploits evanescent waves, which decay exponentially from the intermediate surface of different substrates. Thus, at the end of the near-field, a sub-diffraction area is formed to excite molecules. Near-field scanning optical microscopy (NSOM) [53, 54] in Figs. 3.1((a) and (b)) achieves nanometer resolution signal in front of the scanning tip apex. NSOM is a microscope system without lens optics. Instead lenses, it exploits a scanning tip with a tiny aperture (**a**) smaller than the wavelength (λ). When the light is incident from an aperture of such a scale, we can observe exponentially decaying electromagnetic wave called evanescent wave within the distance (**h**) less $\ll \lambda$ from the aperture. When the NSOM is applied for illumination system in fluorescence imaging, the emission signal can be acquired by the same aperture tip and additional objective lens as shown in Figs. 3.1((a) and (b)), respectively. In biological application NSOM should be treated with cautions such as the maintenance of a tip position and the form of the tip. To achieve sub-diffraction illumination the distance (**h**) between aperture and sample should be maintained within λ. Therefore, the position of the aperture tip needs precision controls in x, y, and z axis. Such controls can be achieved by using Piezo actuators. Moreover, the curved shape of the tip has a number of advantages in biological applications [55] but is a great disadvantage in fabrication.

In total internal reflection microscopy (TIRFM), the evanescent wave at near-field is generated by

total internal reflection phenomena instead of a nanoscale aperture. Depending on the illumination optics, TIRFM can be implemented by a prism and objective lens as shown in Figs. 3.1((c) and (d)), respectively. The limited illumination depth ($< 100nm$) is helpful in exciting surface bounded fluorescence molecules on some occasions as following [56].

(a) Selective visualization of cell/substrate contact regions

(b) Visualization and spectroscopy of single molecule fluorescence near a surface

(c) Measurements of the kinetic rates of binding of extracellular and intracellular proteins to cell surface receptors and artificial membranes

(d) Comparison of membrane-proximal ionic transients with simultaneous transients deeper in the cytoplasm

Practically, the limited imaging depth is helpful in imaging with vert low background fluorescence, virtually no out-of-focus fluorescence signals, and minimal exposure of cells to light at any other planes in the sample. Thanks to its single molecule excitation and detection, the recent nanoscopy have been applied withTIRFM for sub-diffraction illumination. The evanescence wave with weak illumination achieved the excitation of sparse subsets of fluorophore probes in localization based nanoscopy.

3.3 Nanoscopy by point spread function engineering

KAIST

In stimulate emission depletion (STED) microscopy and saturated structure illumination microscopy (SSIM), they achieved nanoscale effective PSF. For example, in STED microscopy [17], the STED beam consists of Gaussian and doughnut shaped patterns that are aligned on-axis, which take the roles of excitation and de-excitation beams, respectively. The doughnut-shaped STED beam is generated by specific phase plate to quench the fluorophores at the rim of the excitation focal spot with a wavelength of the red edge of the fluorophore emission spectrum. When the aligned STED beam is illuminated on the fluorescence tagged samples, it generates nanoscale effective PSF corresponding to the actual excitation areas as shown in Fig. 3.2. The resolution of STED is determined by the intensities of STED beams as follows :

$$\frac{\lambda}{2NA\sqrt{1 + I_{max}/I_{sat}}} \tag{3.1}$$

where I_{max} is the maximum intensity of de-excitation beam, and I_{sat} is the intensity of dropping the fluorescence signal to $1/e$ of the initial value. Simply speaking, a super resolution ($10 \sim 20nm$) image of STED is the direct result of the scanning process without additional mathematical processing.

In practice, the optical setup requires cautions with STED beams, that is correct timing, duration of pulse, and a good quality of the doughnut-shape. According to Eq. (3.1), to achieve $10 \sim 20nm$

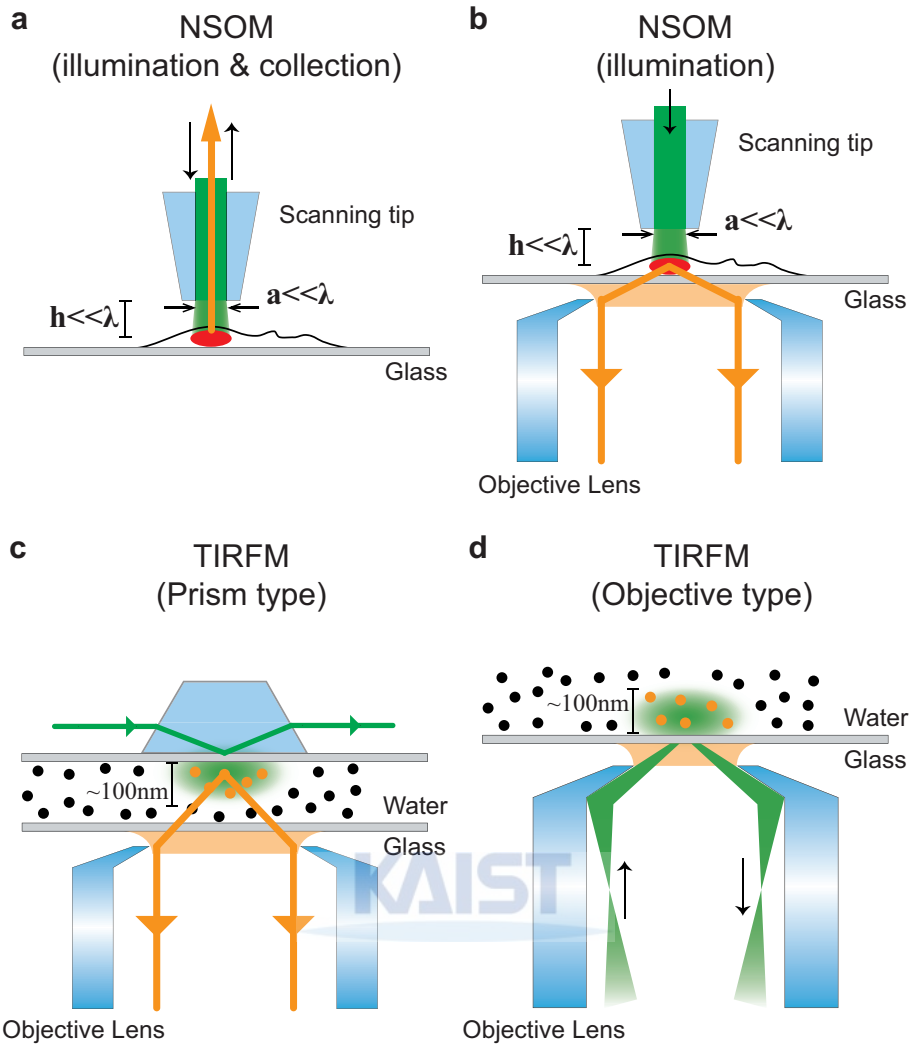

Figure 3.1: The variety of near-field optical microscopy. (a) NSOM with scanning tip of illumination and detection; (b) NSOM with scanning tip and objective lens for illumination and detection, respectively; (c) TIRFM with illumination of prism; (d) TIRFM with the objective lens of illumination and detection.

lateral resolution, it requires an intense (picosecond) pulsed laser ($\approx 100MW/cm^2$) de-exciting the fluorescence dye to a ground state by stimulated emission. Thus, they introduce reversible saturable optical fluorescence transitions (RESOLFT) as a generalized description of STED microscopy by using a low power laser and photoswitchable probes [57]. Finally, STED microscopy is combined with dual lens optics called iso-STED [58] for $20 \sim 100nm$ axial resolution and is also demonstrated with two color imaging [59].

In SSIM [18], the spatial modulation pattern is illuminated to a sample expanding the spatial frequency of optical system as well as reducing effective PSF as shown in Fig. 3.3. The structured illumination pattern is formed by interference phenomena and spatial modulation. The former is implemented by common-path inteferometry by using diffraction grating as shown in Fig. 3.3(a). The modulation frequency is controlled by the optical scanning system. Additionally, the recent SSIM is applied with

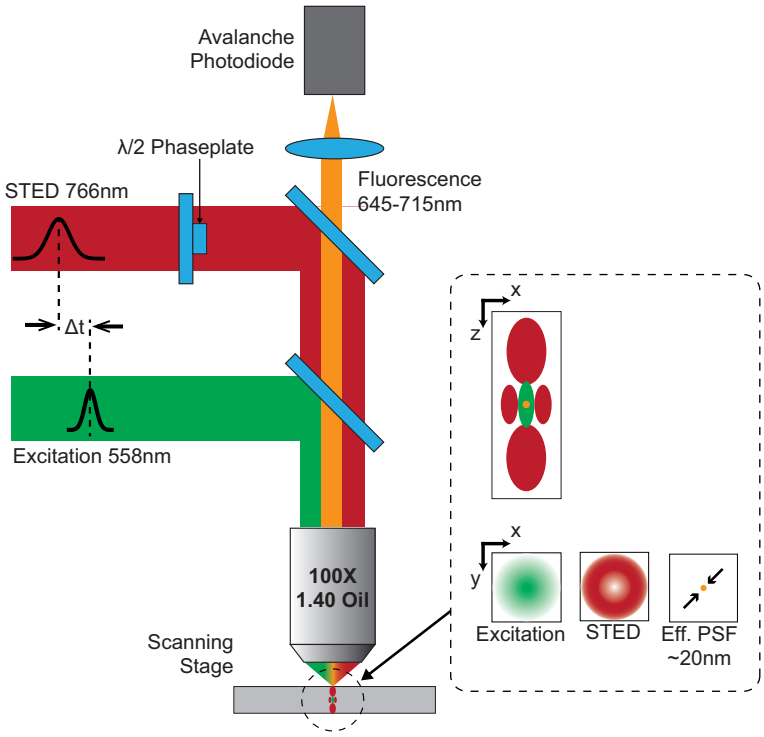

Figure 3.2: The optical setup of STED microscopy and the principe of nanoscale effective PSF. The doughnut-shaped STED beam (red) de-excites the fluorescence molecules at the rim of excitation PSF (green). The excited fluorescence molecules emit the fluorescence signals (orange) within nanoscale PSF.

a spatial light modulator (SLM) to achieve structured patterns to easily generate modulation patterns [60]. The range of observable spatial frequency of the optical system is depicted in Fig. 3.3(b). By using spatial modulation pattern in Fig. 3.3(c), the range of observable spatial frequency can be extended to modulation frequency. After the available modulations are applied, the final extended spatial frequency of SSIM is acquired as shown in Fig. 3.3(e). The resolution of SIM is theoretically unlimited, but practically, the resolution of linear SIM and saturated SIM (SSIM) is limited to $\sim 100nm$ and $\sim 55nm$, respectively. Even though the performance of SSIM is better than linear SIM, SSIM applied a high power laser that yields photobleaching. Recently, the linear SIM technique is extended to 3D and multi-color imaging [60].

3.4 Nanoscopy by stochastic reconstruction

The localization of single molecules provides sub-diffraction limited resolution such as Gaussian model approximation [19, 20, 21] and statistical signal processing [22, 23]. It calculate the centroid of individual molecules in the sequence of fluorescence images using conventional microscopy. Fluorescence imaging with one-nanometer accuracy (FIONA) [21] calculates the curve-fitting of PSF of individual

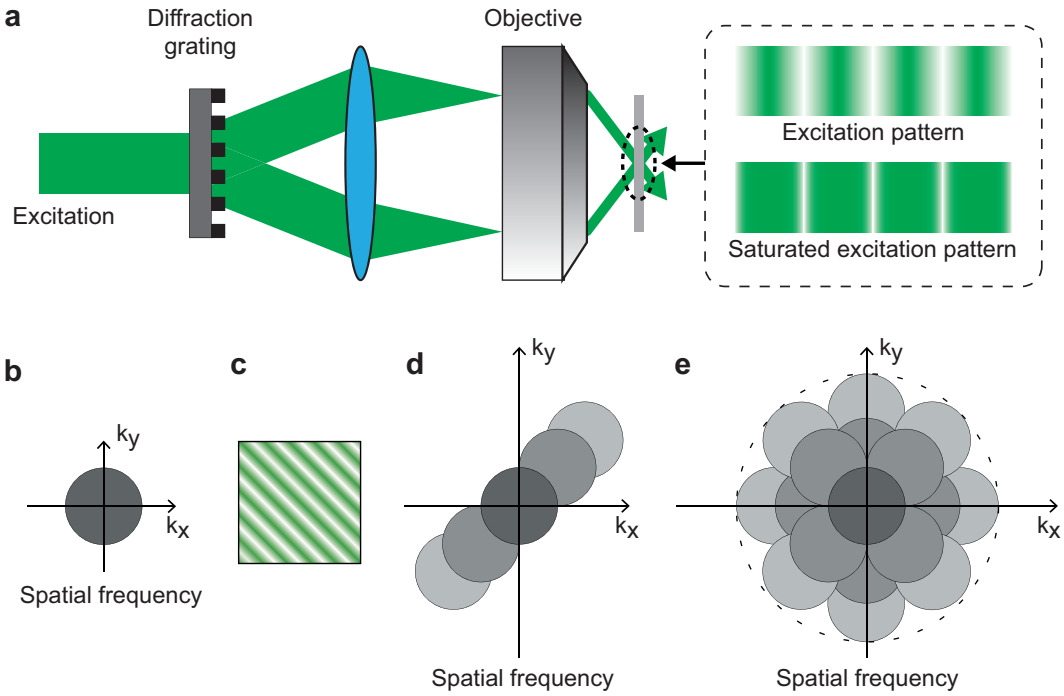

Figure 3.3: Saturated Structure Illumination Microscopy (SSIM). (a) The generation of a structured illumination pattern; (b) The observable region of a spatial frequency space by conventional microscopy. (c) The illumination pattern for spatial modulation of (b). (d) The extended spatial frequency space of (b) by (c). (e) The observable regions when the total imaging procedure is finished.

molecules, then the standard error of the center is defined as following [20] :

$$\sqrt{\frac{\sigma^2}{N} + \frac{a^2}{12N} + \frac{8\pi\sigma^4 b^2}{a^2 N^2}}, \tag{3.2}$$

where σ and N are standard deviation of Gaussian model as PSF and the number of detected photons, and a and b are the effective pixel size of detectors and the noise from background signals and detectors, respectively.

The accuracy of FIONA reaches a 1.5nm localization error. Specifically, the localization accuracy given by Eq. (3.2) is achieved by the fundamental limit of single molecule target detection within various noise. In the photon noise-free case, the standard deviation (σ) of PSF determines the localization error in the first term. In addition, the pixelation (a) noise from the uncertainty of the photon arrival can be considered using the second term. Finally, for the pure background noise (b), the final term is inserted. Therefore, to achieve nanometer localization accuracy, severe conditions should be satisfied. Fundamentally, the number of the collected photons (N) is the most important factor. In most single molecule microscopy, to achieve enough number of collected photons from a single molecule, a high quantum yield of molecules and high quantum efficiency of the detectors are required.

Recently, photoactivation localization microscopy (PALM) [24] and stochastic optical reconstruction

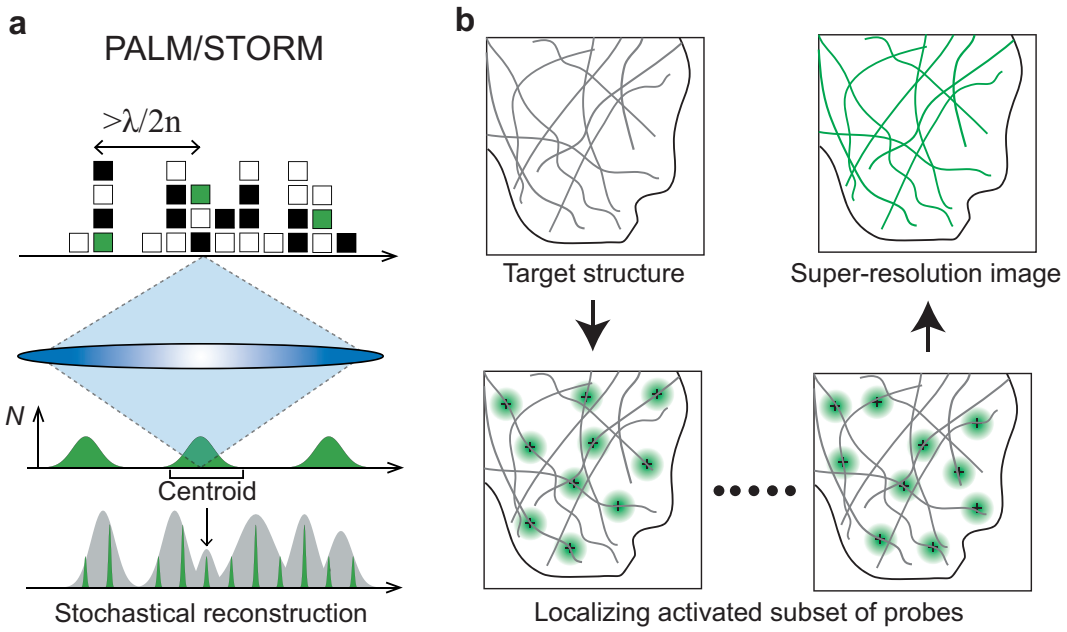

Figure 3.4: PhotoActivation Localization Microscopy (PALM) and STochastical Optical Reconstruction Microscopy (STORM). (a) PALM/STORM reconstruct a super-resolution image by stochastic reconstruction; when weak illumination sparsely switched on individual probes, the detected photon (N) enables the centroid calculation for individual probes. (b) For the given target sample, STORM achieved a super-resolution image by localizing activated sparse subsets of photoswitching probes for total imaging cycles.

KAIST

microscopy (STORM) [25] have broken the diffraction limit by separating the unresolved individual molecules temporally from the spatial domain. For each imaging cycle, the sparse subset of fluorophores is achieved by excitation, localization and de-excitation of individual photoswitchable fluorophores as shown in Figs. 3.4((a) and (b)). The imaging sequence is repeated when the fluorophores are photobleached. To avoid concurrence events in the diffraction limited distance which causes inaccurate localization, PALM/STORM consecutively switch on the fluorophores at stochastic positions based on TIRFM and weak illumination. It then localizes the centroid of fluorescent signals for each imaging cycle, and finally the overall image provides a nanometer resolution ($\sim 20nm$) fluorescence image. The resolution of these methods highly depends on the number of detected photons (N) as shown in Fig. 3.4(a).

$$\frac{\lambda}{2NA\sqrt{N}} \tag{3.3}$$

Using red fluorophores that can be switched on and off by red and green laser, respectively, a strong red laser pulse is firstly switched to the dark state of all fluorophores as depicted in the black boxes in Fig. 3.4(a). After that, a weak green laser pulse is used to switch on only a fraction of the fluorophores (green boxes), and then the red laser is again illuminated to switch off the turned-on fluorophores (white boxes) allowing their center positions. Then the overall super resolution image is reconstructed from all

fluorophore positions measured from multiple imaging cycles. The total acquisition time of stochastic methods is highly dependent on the number of fluorophores in the concerned sample, while STED microscopy linearly counts the intensity of fluorophores. PALM/STROM can be implemented using photo-activated fluorescence proteins (PA-FP) and synthesized dye pairs as optical switch, respectively. The available fluorescent molecules for PALM/STORM are limited due to its non-linear imaging physics of photoswitching. Further extension to 3 dimensional imaging and two color imaging are achieve by using astigmatism of a lens [61] and combination of synthetic dye pairs [62], respectively.

Furthermore, the statistical property of a fluctuated fluorescent signal is applied to resolve the individual molecules. For example, a quantum dot is often used for super resolution imaging due to its non-linear blinking statistics [22, 23]. Recently, super-resolution optical fluctuation imaging (SOFI) [23] has applied high order statistics of fluctuated signals coming from quantum dot blinking and intermittency. Then the n_{th} order cumulants of the measured signal is given by

$$C_n(\mathbf{r}, \tau_1, \cdots, \tau_{n-1}) = \sum_k U^n(\mathbf{r} - \mathbf{r}_k)\epsilon_k^n w_k(\tau_1, \cdots, \tau_{n-1}) \tag{3.4}$$

where, U, ϵ, and w are PSF, molecular brightness, and correlation-based weighting function, respectively. Then the effective PSF of n_{th} order of U leads to $\sqrt{n}$-fold of optical resolution improvement. Practically, the calculation of high order cumulants causes high computation complexity; thus, they achieve the resolution of $55 \pm 3nm$.

KAIST

3.5 Discussion

We briefly reviewed conventional nanoscopy methods which are realized by non-linear behaviors to resolve sub-diffraction images. The nanoscopy engineering effective PSF exploits a complicated optical system or high intensity lasers. The nanoscopy based on single molecule imaging techniques exploit photoswitching probes and localization algorithms. Furthermore, single molecule imaging techniques utilize conventional sub-diffraction illumination. Although they have achieved nanometer resolution imaging, non-specialized fluorescence probes and conventional fluorescence microscopy are commonly required for cellular imaging. Thus, for the widespread use of nanoscopy as a routine work for biologist, the nanoscopy imaging modality for conventional experimental protocols and microscopy is recommended.

Chapter 4. Theory of Nano-MUSIC

4.1 Nano-MUSIC

We present a novel nanometer resolution imaging method using Speckle Illumination and Multiple Signal Classification (nano-MUSIC). The main idea of the nano-MUSIC system is that two fluorophores within diffraction limit can be separated, if the temporal fluctuations of the two fluorescence emission are uncorrelated. As shown in Fig. 4.1, even though the fluorescence emission can be spatially overlapped in some time instances, if the cross correlation of the two emission are uncorrelated, the two dye can be separated using array signal processing technique such as multiple signal classification (MUSIC) [27]. The key idea is that such uncorrelated emission can be easily obtained by illuminating spatially incoherent light such as speckle illumination. By allowing spatial overlap between two adjacent probes, one of the main advantage of the nano-MUSIC is that the fluorophore does not need to be photoswitchable. Moreover, parallel excitation of larger number of fluorophore can be easily implemented. Using such spatially incoherent speckle illumination and advanced signal processing technique, the imaging problem can be converted to target detection problem, and sub diffraction limit resolution can be achieved.

KAIST

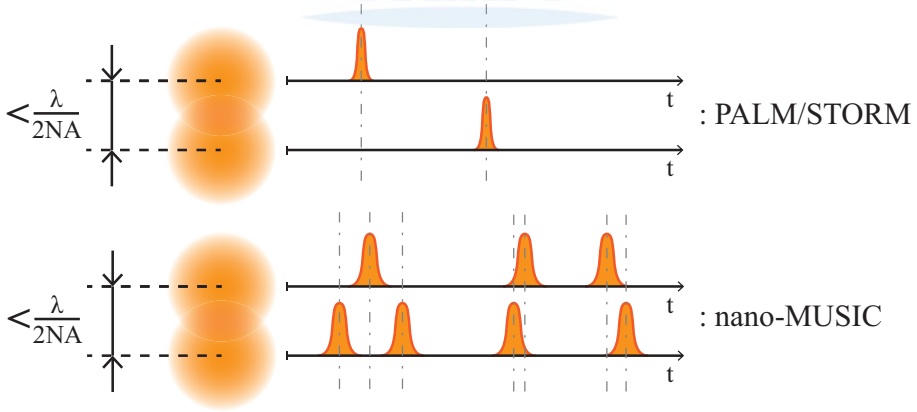

Figure 4.1: Fluorescence emission acquision of PALM/STORM and nano-MUSIC.

More specifically, suppose there exist a single fluorescence molecule at $\boldsymbol{\theta} = (x, y)$. An image intensity measured at the l-th CCD pixel at snapshot t is then given by

$$y_l(t) = a_l(\boldsymbol{\theta})x(t), \tag{4.1}$$

where $a_l(\boldsymbol{\theta})$ is a detector PSF from the fluorephore to the CCD pixel, and $x(t)$ denotes the corresponding fluorescence emission signal. For a subset of CCD elements composed of L pixel as shown in Fig. 4.2, (4.1) can be represented in a vector form

$$\mathbf{y}(t) = \mathbf{a}(\boldsymbol{\theta})x(t) \tag{4.2}$$

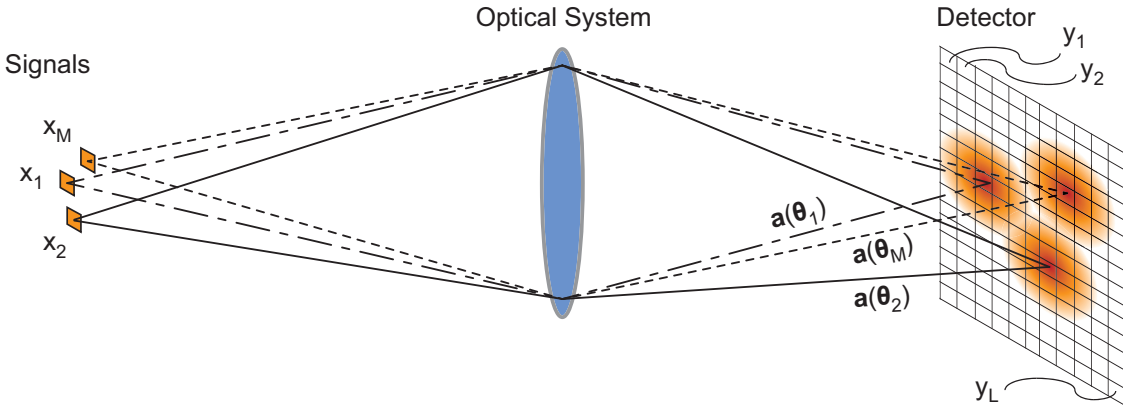

Figure 4.2: The image formation concept of optical microscope system. Comparing to Fig. 1.2, we consider the sensor array and airplanes as camera and fluorescence signals, respectively.

where $\mathbf{y}(t) = [y_1(t), y_2(t), \cdots, y_L(t)]^T$ is a sensor array measurement composed of multiple CCD pixels at snapshot t, and $\mathbf{a}(\boldsymbol{\theta}) = [a_1(\boldsymbol{\theta}), a_2(\boldsymbol{\theta}), \cdots, a_L(\boldsymbol{\theta})]^T$. If photons from multiple fluorephores at $\boldsymbol{\Theta} = [\boldsymbol{\theta}_1, \cdots, \boldsymbol{\theta}_M]^T$ impinges on the sensor array, (4.2) can be represented as

$$\mathbf{y}(t) = \sum_{m=1}^{M} \mathbf{a}_m(\boldsymbol{\theta}_m) x_m(t). \tag{4.3}$$

The sensor array measurement can be put in a more compact form by defining a point spread function (PSF) matrix and a vector of fluorescence emission:

$$\begin{aligned} \mathbf{A}(\boldsymbol{\Theta}) &= [\mathbf{a}(\boldsymbol{\theta}_1), \cdots, \mathbf{a}(\boldsymbol{\theta}_M)] \in \mathbb{R}^{L \times M} \\ \mathbf{x}(t) &= [x_1(t), \cdots, x_M(t)]^T . \end{aligned}$$

Note that in the noiseless case, the sensor array measurement is then confined to an M-dimensional subspace of the L space if $M < L$. In real experiments, there always exists an additive noise $\mathbf{n}(t)$ to each sensor measurements. Accordingly, the noisy measurement vector is given by

$$\mathbf{y}(t) = \mathbf{A}(\boldsymbol{\Theta})\mathbf{x}(t) + \mathbf{n}(t) \tag{4.4}$$

For a sufficiently large number of snapshots, the correlation between sensor elements can be represented by a spatial covariance matrix :

$$\mathbf{R}_\mathbf{y} = \overline{< \mathbf{y}(t), \mathbf{y}(t) >} = \mathbf{A}(\boldsymbol{\Theta})\mathbf{R}_\mathbf{x}\mathbf{A}(\boldsymbol{\Theta})^H + \sigma^2\mathbf{I}, \tag{4.5}$$

where the signal covariane matrix is $\mathbf{R}_\mathbf{x} = \overline{< \mathbf{x}(t), \mathbf{x}(t) >}$, and $\overline{< \mathbf{n}(t), \mathbf{n}(t) >} = \sigma^2\mathbf{I}$ denotes the noise covariance. Assuming that $\mathbf{R}_\mathbf{x}$ is of full rank, the spatial covariance matrix can be then decomposed by

$$\mathbf{R}_\mathbf{y} = \mathbf{A}\mathbf{R}_\mathbf{x}\mathbf{A}^H + \sigma^2\mathbf{I} = \mathbf{U}\boldsymbol{\Lambda}_s\mathbf{U}^H + \sigma^2\mathbf{Q}\mathbf{Q}^H \tag{4.6}$$

where $\mathbf{\Lambda}_s$ denotes the diagonal matrix composed of eigenvalues $\{\lambda_i\}_{i=1}^{L}$, $\mathbf{U}$ denotes the eigenvectors corresponding the M largest eigenvalues of $\mathbf{R_y}$ such that $\lambda_1 \geq \lambda_2 \geq \cdots \lambda_M \geq \sigma^2$, and $\mathbf{Q}$ is the remaining $L-M$ eigenvectors spanning the "noise subspace" [27].

One of the most popular and successful array signal processing algorithm known as MUSIC (MUltiple Signal Classification) [27] exploits the fact that the noise subspace is orthogonal to $\mathbf{A}(\mathbf{\Theta})$:

$$\mathbf{P_Q a}(\boldsymbol{\theta}) = \mathbf{0}, \quad \boldsymbol{\theta} = \{\boldsymbol{\theta}_1, \cdots, \boldsymbol{\theta}_M\}. \tag{4.7}$$

where $\mathbf{P_Q} = \mathbf{Q}(\mathbf{Q}^*\mathbf{Q})^{-1}\mathbf{Q}^*$ denotes the orthogonal projector on the noise subspace and $\mathbf{Q}^*$ denotes Hermitian transpose. Then, the MUSIC plots the following spatial spectrum

$$p_2(\boldsymbol{\theta}) = \frac{1}{\|\mathbf{P_Q a}(\boldsymbol{\theta})\|_2^2}, \tag{4.8}$$

where $\|\cdot\|_2$ denotes the l_2-norm, and find the M peaks as target locations. If the signal covariance matrix $\mathbf{R_x}$ is diagonal and SNR is high enough, it is well-known that the MUSIC estimator achieves the maximum likelihood (ML) estimator [30], and the ML estimator of multiple target performance achieves the ultimate performance limit of the single target estimation [28].

Note that PALM/STORM satisfies the condition $\overline{< x_i(t), x_j(t) >} = 0$ for $i \neq j$ due to the non-overlapping photo-switching fluorophores. Hence, $\mathbf{R_x}$ is diagonal matrix and the sensor arrays signal processing theory guarantees that its fundamental performance limitation approaches to that of single target detection; hence it approaches the accuracy of single molecule imaging. Similar explanation can be given if the quantum-dot blinking statistics are totally uncorrelated such that $\overline{< x_i(t), x_j(t) >} = 0$ for $i \neq j$. As discussed before, these approach, however, require new type of fluorophores to make the signal covariance matrix diagonal.

Rather than using new type of fluorephores, nano-MUSIC exploits the spatial incoherence of speckle illumination to generate a near-diagonal signal covariance matrix. More specifically, when a coherent CW laser source is transmitted through a diffusor, randomized beam paths yield construction and destruction of light and produces speckle pattern at random positions [63]. Furthermore, by changing the rotation angle of the diffusor, multiple snapshot of randomized speckle patterns can be dynamically generated on specimen. Hence, the signal intensity $x_m(t)$ can be represented as convolution

$$x_m(t) = x_f \int \mathrm{PSF}_{\mathrm{ill}}(\theta^x - \alpha, \theta^y - \beta) e(\alpha, \beta; t) d\alpha d\beta, \tag{4.9}$$

where $\mathrm{PSF}_{\mathrm{ill}}(\theta^x - \alpha, \theta^y - \beta)$ denotes a illumination optics PSF from (α, β) on diffusor to (θ^x, θ^y) on specimen, x_f denotes the fluorescence yield for each fluorophore, and $e(\boldsymbol{\rho}; t)$ denotes electric field distribution of scatter on the diffusor plane. One of the most important observations is that the cross-correlation for the electric field distribution approaches the delta function for fully developed speckle [63] :

$$\overline{< e(\alpha, \beta; t), e(\alpha', \beta'; t) >} = |e_o|^2 e^{-\sigma_o^2 \left(1 - e^{-\frac{\sqrt{(\alpha-\alpha')^2 + (\beta-\beta')^2}}{r_o}}\right)^2} \longrightarrow |e_o|^2 \delta(\alpha - \alpha', \beta - \beta') \tag{4.10}$$

where constants r_o and σ_o^2 depend on the phase variance related to surface height [63]. In **Section 4.2** we discuss this in detail. Hence, the cross-correlation of the fluorescene emission is given by

$$\begin{aligned} R_{\mathbf{x}}(m,n) &= \overline{< x_m(t), x_n(t) >} \\ &\longrightarrow | \quad x_f|^2 |e_o|^2 R_{PSF}(\theta_m^x - \theta_n^x, \theta_m^y - \theta_n^y). \end{aligned}$$

where the illumination PSF autocorrelation function is

$$R_{PSF}(\theta_m^x, \theta_m^y) = (\mathrm{PSF}_{\mathrm{ill}} * \mathrm{PSF}_{\mathrm{ill}})\,(\theta_m^x, \theta_m^y).$$

This implies that the $\mathbf{R_x}$ is the not perfectly diagonal and the width of the off-diagonal term is determined by the FWHM of the autocorrelation function. Similar to PALM/STORM, the effect of autocorrelation function from the illumination optics can be significantly reduced using total internal reflection fluorescence (TIRF) optics. However, even without TIRF optics, there have been extensive investigations in array signal processing literature to improve resolution. Note that the l_2-norm in (4.8) in standard MUSIC can be any norm other than l_2 since the orthogonality holds in any norm. We found that the following l_∞ form of MUSIC is quite effective for super-resolution microscopy:

$$p_\infty(\boldsymbol{\theta}) = \frac{1}{\|\mathbf{P_Q a}(\boldsymbol{\theta})\|_\infty}. \tag{4.11}$$

This is because that l_∞-norm is more effective in reducing the side-lobe for the non-target location. More specifically, thanks to the norm inequality, we can easily see that $\|\mathbf{P_Q a}(\boldsymbol{\theta})\|_\infty \geqslant \|\mathbf{P_Q a}(\boldsymbol{\theta})\|_2$ if $\boldsymbol{\theta}$ is not a correct target position, whereas $\|\mathbf{P_Q a}(\boldsymbol{\theta}^*)\|_\infty = \|\mathbf{P_Q a}(\boldsymbol{\theta})\|_2 = 0$ when $\boldsymbol{\theta}^*$ is the correct target location. Hence the contrast between non-target region and target region is higher in l_∞-MUSIC compared to l_2-MUSIC.

4.2 Speckle Illumination

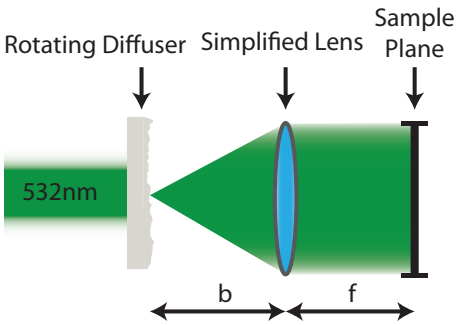

Figure 4.3: Simplified illumination optical geometry. The distances **b** and **f** are back focal length and front focal length, respectively. Such simplified optics represents modified Köller illuminator for a speckle field.

When the coherent source such as laser is reflected or transmitted from rough surface or turbid media, the randomized beam paths yield construction and destruction of light at random positions [63]. We first consider the measured signal model of electric field distribution of scattering and speckle fields. In Fig. 4.3, the illumination source is scattered in a diffusor plane, then the speckle field is generated on sample plane. More specifically, we consider the measured signal model from speckle illumination. The illumination source is scattered from a diffusor plane, then the speckle field is generated on specimen. Here, an image intensity measured at the detector position $\boldsymbol{\rho} = (x_d, y_d)$ is given by

$$y(\boldsymbol{\rho}; t) = \int \mathrm{PSF}_{det}(\boldsymbol{\rho}; \boldsymbol{\theta}) x_f(\boldsymbol{\theta}) \phi_s(\boldsymbol{\theta}; t) d\boldsymbol{\theta} \tag{4.12}$$

where $\mathrm{PSF}_{det}(\boldsymbol{\rho}; \boldsymbol{\theta})$ is a detector PSF when a point source is located in $\boldsymbol{\theta} = (x, y)$ on a sample plane, and $\phi_s(\boldsymbol{\theta}; t)$ denotes the speckle field from a diffusor on the specimen, and $x_f(\boldsymbol{\theta})$ is the fluorophore distribution on a specimen, which can be modeled as sum of dirac delta functions.

$$x_f(\boldsymbol{\theta}) = x_o \sum_{m=1}^{M} \delta(\boldsymbol{\theta} - \boldsymbol{\theta}_m), \tag{4.13}$$

where M denotes the number of fluorophores, and x_o is the intensity of each fluorophore. For speckle illumination, the speckle field on a specimen is given by

$$\phi_s(\boldsymbol{\theta}; t) = \int \mathrm{PSF}_{ill}(x - \alpha, y - \beta) e(\alpha, \beta; t) d\alpha d\beta \tag{4.14}$$

where $e(\alpha, \beta; t) = e_o \exp[j\phi_h(\alpha, \beta; t)]$ denotes the electric field distribution of scatter on the diffusor plane, whose cross-correlation is given by [63]

$$\begin{aligned}
\mathbf{R}_e(\alpha, \beta; \alpha', \beta') &= \overline{\langle e(\alpha, \beta; t) e^*(\alpha', \beta'; t - \tau) \rangle} \\
&= |e_o|^2 \boldsymbol{\mu}_e(\Delta\alpha, \Delta\beta) \\
&= |e_o|^2 e^{-\sigma_o^2 (1 - \mu_h(|(\Delta\alpha, \Delta\beta)|))} \\
&= |e_o|^2 \exp\left[-\sigma_o^2 (1 - e^{-(r/r_o)^2})\right] \\
&= \begin{cases} |e_o|^2 \exp(-\sigma_o^2), & r/r_o \to \infty \\ |e_o|^2 \delta(\Delta\alpha, \Delta\beta), & r/r_o \to 0 \end{cases}
\end{aligned} \tag{4.15}$$

where the normalized correlation function $\boldsymbol{\mu}_e = e^{-\sigma_o^2 [1 - \mu_h(\Delta\alpha, \Delta\beta)]}$ for a height correlation function μ_h where $\mu_h(r) = \exp[-(r/r_o)^2]$ for some constant r_o. Note that, the function $\exp(-\sigma_o^2)$ approaches zero as the phase variance σ_o^2 grows since it is proportional to the height variance σ_h^2. Here, $\sigma_o^2 = \frac{4\pi}{\lambda} \sigma_h^2$ denotes the phase variance related to surface height.

Under the assumption that diffusor is sufficiently rough, as two arbitrary points on diffusor apart further, they become statistical independence. In contrary to that, the distance of those points gets

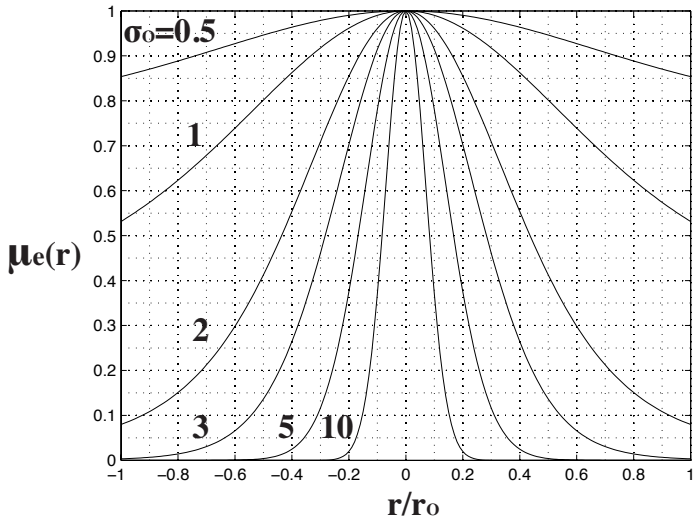

Figure 4.4: The normalized correlation function $\boldsymbol{\mu}_e(\Delta\alpha, \Delta\beta)$ for several different roughness of diffusor.

closer, the correlation increases. According to Fig. 4.4, the correlation function ($\mathbf{R}_e$) of the distance depends on the roughness (σ_0) of diffusor.

Then for fully developed speckle, $\mathbf{R}_e(\alpha,\beta\,;\alpha',\beta') = |e_o|^2\delta(\alpha-\alpha',\beta-\beta')$ [63]. Hence, the cross-correlation of the speckle illumination is given by

$$\begin{aligned}\mathbf{R}_\phi(\boldsymbol{\theta}_n,\boldsymbol{\theta}_m) &= <\overline{\phi_s(\boldsymbol{\theta}_n;t)},{\phi_s}^*(\boldsymbol{\theta}_m;t)> \\ &= \int\int \mathrm{PSF}_{ill}(\boldsymbol{\theta}_n-\boldsymbol{\theta})\mathbf{R}_e(\boldsymbol{\theta}_n,\boldsymbol{\theta}'_m)\mathrm{PSF}^*_{ill}(\boldsymbol{\theta}_m-\boldsymbol{\theta}')d\boldsymbol{\theta}d\boldsymbol{\theta}'. \end{aligned} \tag{4.16}$$

Therefore, for fully developed speckle, the cross-correlation of the measured intensity on detector plane is given by $\mathbf{R}_y = [r_{ij}]$

$$r_{ij} = \sum_{m=1}^{M}\sum_{n=1}^{N}\mathrm{PSF}_{det}(\boldsymbol{\theta}_i;\boldsymbol{\theta}'_n)\mathrm{PSF}^*_{det}(\boldsymbol{\theta}_j;\boldsymbol{\theta}'_m)\mathbf{R}_x(\boldsymbol{\theta}'_m-\boldsymbol{\theta}'_n) \tag{4.17}$$

where the cross-correlation function $\mathbf{R}_x(\boldsymbol{\theta}'_m-\boldsymbol{\theta}'_n)$ is given by

$$\mathbf{R}_x(\boldsymbol{\theta}'_m-\boldsymbol{\theta}'_n) = |e_o|^2|x_o|^2\int \mathrm{PSF}_{ill}(\boldsymbol{\theta}'_m-\boldsymbol{\theta})\mathrm{PSF}^*_{ill}(\boldsymbol{\theta}'_n-\boldsymbol{\theta})d\boldsymbol{\theta}. \tag{4.18}$$

Therefore, the signal correlation matrix does not have diagonal matrix due to the illumination optics (PSF_{ill}) from Eq. (4.18). As illustrated in Fig. 4.5, for 1000 speckle snapshots in Fig. 4.5(a), we calculate the mean and correlation matrix as Figs. 4.5((b) and (c)), respectively. This correlation matrix contains the effects of illumination and imaging optics. The profile in Fig. 4.5(d) is acquired by averaging off-diagonal element along with diagonal elements. The FWHM of this profile is almost same with diffraction limit ($\lambda_{ex}/2\mathrm{NA} = 204nm$).

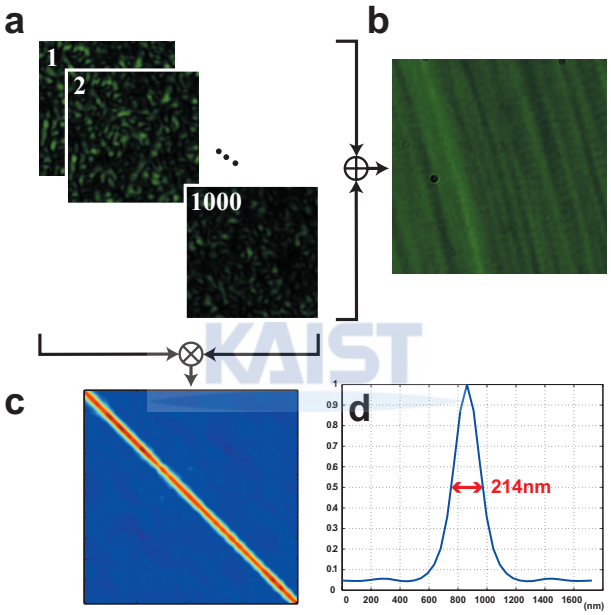

Figure 4.5: Measured speckle patterns and their characteristics. (a) Measured speckle patterns for 1000 snapshots, (b) and (c) mean and correlation matrix of measured speckle patterns, (d) averaged off-diagonal elements along with diagonal elements of (c).

Chapter 5. Fundamental Limit Characterization of Nano-MUSIC

5.1 Cramér-Rao bound

In previous Chapter, we investigated the nano-MUSIC algorithm to estimate the location of fluorescence probes from noisy measurement ($\mathbf{y}(t) = \mathbf{A}(\boldsymbol{\Theta})\mathbf{x}(t) + \mathbf{n}(t)$). To quantify the estimation accuracy, we assume that the unknown parameters represent random variables of probability density function (PDF) of estimation error, and the PDF as a function of unknown parameters is termed likelihood function. The accuracy of unbiased estimation of unknown parameters is relevant to the sharpness of the likelihood function, which is represented by negative of the second derivative of log-likelihood function. Here, the fundamental limit of the estimate accuracy is provided by Cramér-Rao lower bound (CRB) [28, 29, 31, 30]. The likelihood function of given noisy measurement model in Eq. (4.4) is as follows

$$\begin{aligned} &f(\mathbf{y}(1), \cdots, \mathbf{y}(N); \boldsymbol{\Theta}, \mathbf{x}(1), \cdots, \mathbf{x}(N)) \\ &= \frac{1}{(\pi\sigma^2)^{LN/2}} \exp\left(-\sum_{t=1}^{N} \frac{1}{\sigma^2} \|\mathbf{y}(t) - \mathbf{A}(\boldsymbol{\Theta})\mathbf{x}(t)\|^2 \right), \end{aligned} \tag{5.1}$$

where the variance of uncorrelated noise is $\sigma^2/2$ for the convenience of notation, and the log likelihood function is also given by

$$\ln f = -\frac{LN}{2} \ln \pi - LN \ln \sigma - \frac{1}{\sigma^2} \sum_{t=1}^{N} \|\mathbf{e}(t)\|^2. \tag{5.2}$$

Then variance of estimation error ($\boldsymbol{\Theta} - \hat{\boldsymbol{\Theta}}$) is given by

$$\mathrm{Var}(\hat{\boldsymbol{\Theta}}) = E[(\boldsymbol{\Theta} - \hat{\boldsymbol{\Theta}})(\boldsymbol{\Theta} - \hat{\boldsymbol{\Theta}})^H] \geqslant \mathrm{CRB}(\boldsymbol{\Theta}) \triangleq \mathbb{I}^{-1}(\boldsymbol{\Theta}) \tag{5.3}$$

where $\mathbb{I}(\boldsymbol{\Theta})$ is known as Fisher information matrix (FIM) defined by [31]

$$[\mathbb{I}(\boldsymbol{\Theta})]_{ij} = -E\left[\frac{\partial^2 \ln f(\mathbf{y}; \boldsymbol{\Theta})}{\partial\theta_i \partial\theta_j} \right]. \tag{5.4}$$

When we denote by

$$\frac{\partial f}{\partial \mathbf{x}} \overset{\text{def}}{=} \left[\frac{\partial f}{\partial x_1}, \frac{\partial f}{\partial x_2}, \cdots, \frac{\partial f}{\partial x_n} \right]^T, \tag{5.5}$$

the partial derivatives of log-likelihood function for the location of fluorophore ($\boldsymbol{\Theta} = [\boldsymbol{\theta}_1, \cdots \boldsymbol{\theta}_M]$) is given as follows

$$\frac{\partial \ln f}{\partial \boldsymbol{\Theta}} = \left[\left(\frac{\ln f}{\partial \boldsymbol{\theta}_1} \right)^T, \left(\frac{\ln f}{\partial \boldsymbol{\theta}_2} \right)^T, \cdots, \left(\frac{\ln f}{\partial \boldsymbol{\theta}_M} \right)^T \right]^T. \tag{5.6}$$

Theorem 1. *Let*

$$\mathbf{D} = \left[\frac{\partial \mathbf{a}(\boldsymbol{\theta}_1)}{\partial \theta_1}, \frac{\partial \mathbf{a}(\boldsymbol{\theta}_2)}{\partial \theta_2}, \cdots, \frac{\partial \mathbf{a}(\boldsymbol{\theta}_M)}{\partial \theta_M} \right] \tag{5.7}$$

$$\mathbf{P} = \frac{1}{N} \sum_{t=1}^{N} \mathbf{x}(t)\mathbf{x}^T(t), \tag{5.8}$$

then the CRB for enough snapshots is given by

$$\mathrm{CRB}^{-1}(\boldsymbol{\Theta}) = \frac{2N}{\sigma^2} \sum_{t=1}^{N} \Big\{ \left[\mathbf{D}^H(\boldsymbol{\Theta}) \left[\mathbf{I} - \mathbf{A}(\mathbf{A}^H\mathbf{A})^{-1}\mathbf{A}^H \right] \mathbf{D}(\boldsymbol{\Theta}) \right] \odot \mathbf{P}^T \Big\} \tag{5.9}$$

where $\odot$ denotes the Schur-Hadamard element by element matrix product.

Proof. Taking partial derivatives of $\ln f$, we acquire

$$\frac{\partial \ln f}{\partial \sigma} = -\frac{LN}{\sigma} + \frac{2}{\sigma^2} \sum_{t=1}^{N} \|\mathbf{e}(t)\|^2 \tag{5.10}$$

$$\frac{\partial \ln f}{\partial \mathbf{x}(t)} = \frac{2}{\sigma^2} \mathrm{Re}\left[\mathbf{A}^H(\boldsymbol{\Theta})\mathbf{e}(t) \right] \tag{5.11}$$

$$\frac{\partial \ln f}{\partial \boldsymbol{\theta}_i} = \frac{2}{\sigma^2} \sum_{t=1}^{N} \mathrm{Re}[x_i^H(t)\mathbf{D}_i^H(\boldsymbol{\theta}_i)\mathbf{e}(t)]^H \tag{5.12}$$

where $\mathbf{D}_i^H(\boldsymbol{\theta}_i)$ is defined as Eq. (5.7). Thus

$$\frac{\partial \ln f}{\partial \boldsymbol{\Theta}} = \frac{2}{\sigma^2} \sum_{t=1}^{N} [\mathbf{X}^H(t)\mathbf{D}^H(\boldsymbol{\Theta})\mathrm{e}(t)]^H \tag{5.13}$$

where $\mathbf{X}(t) = diag[\mathbf{x}(t)]$. Let

$$\mathbf{F} = \frac{2}{\sigma^2} \sum_{t=1}^{N} \mathbf{X}^H(t)\mathbf{D}^H(\boldsymbol{\Theta})\mathbf{D}(\boldsymbol{\Theta})\mathbf{X}(t) \tag{5.14}$$

$$\mathbf{G}(t) = \frac{2}{\sigma^2} \mathbf{A}^H(\boldsymbol{\Theta})\mathbf{D}(\boldsymbol{\Theta})\mathbf{X}(t) \tag{5.15}$$

$$\mathbf{H} = \frac{2}{\sigma^2} \mathbf{A}^H(\boldsymbol{\Theta})\mathbf{A}(\boldsymbol{\Theta}). \tag{5.16}$$

Then,

$$E\Big\{ \frac{\partial^2 \ln f}{\partial \sigma \partial \boldsymbol{\Theta}} \Big\} = E\Big\{ -\frac{4}{\sigma^3} \sum_{t=1}^{N} \mathrm{Re}\left[\mathbf{X}^H(t)\mathbf{D}^H(\boldsymbol{\Theta})\mathbf{e}(t) \right] \Big\} = \mathbf{0} \tag{5.17}$$

$$E\Big\{ \frac{\partial^2 \ln f}{\partial \theta_i \partial \theta_j} \Big\} = -\frac{2}{\sigma^2} \sum_{t=1}^{N} \mathrm{Re}\left[x_i^H(t)\mathbf{D}_i^H(\theta_i)\mathbf{D}_j(\theta_j)x_j(t) \right],$$

$$E\Big\{ \frac{\partial^2 \ln f}{\partial \boldsymbol{\Theta}^2} \Big\} = -\frac{2}{\sigma^2} \sum_{t=1}^{N} \mathrm{Re}\left[\mathbf{X}^H(t)\mathbf{D}^H(\boldsymbol{\Theta})\mathbf{D}(\boldsymbol{\Theta})\mathbf{X}(t) \right] = -\mathrm{Re}(\mathbf{F}). \tag{5.18}$$

And then we also take second partial derivatives of $\ln f$ with respect to $\mathbf{x}$,

$$E\Big\{ \frac{\partial^2 \ln f}{\partial \sigma \partial \mathbf{x}(t)} \Big\} = E\Big\{ -\frac{4}{\sigma^2} \mathrm{Re}\left[\mathbf{A}^H(\boldsymbol{\Theta})\mathbf{e}(t) \right] \Big\} = \mathbf{0} \tag{5.19}$$

$$E\Big\{ \frac{\partial^2 \ln f}{\partial \mathbf{x}(s) \partial \mathbf{x}(t)} \Big\} = -\frac{2}{\sigma^2} \mathrm{Re}(\mathbf{A}^H\mathbf{A})\delta_{st} = -\mathrm{Re}(\mathbf{H})\delta_{st} \tag{5.20}$$

$$E\Big\{ \frac{\partial^2 \ln f}{\partial \mathbf{x}(t) \partial \boldsymbol{\Theta}} \Big\} = -\frac{2}{\sigma^2} \mathrm{Re}\left[\mathbf{A}^H(\boldsymbol{\Theta})\mathbf{D}(\boldsymbol{\Theta})\mathbf{X}(t) \right] = -\mathrm{Re}\left[\mathbf{G}(t) \right]. \tag{5.21}$$

Therefore the CRB matrix known as Fisher information matrix is as follows [29]

$$\mathbb{I}(\boldsymbol{\Theta}, \mathbf{x}(1), \cdots, \mathbf{x}(L)) = \begin{bmatrix} \mathrm{Re}(\mathbf{H}) & \mathbf{0} & \cdots & \mathrm{Re}\left[\mathbf{G}(1)\right] \\ \mathbf{0} & \mathrm{Re}(\mathbf{H}) & \mathbf{0} & \vdots \\ \mathbf{0} & \mathbf{0} & \mathrm{Re}(\mathbf{H}) & \mathrm{Re}\left[\mathbf{G}(L)\right] \\ \mathrm{Re}\left[\mathbf{G}^H(1)\right] & \cdots & \mathrm{Re}\left[\mathbf{G}^H(L)\right] & \mathrm{Re}(\mathbf{F}) \end{bmatrix}. \tag{5.22}$$

From the CRB matrix we finally achieve the lower CRB for the DOA ($\boldsymbol{\Theta}$) using a matrix inversion formula for a partitioned matrix [64].

$$\mathrm{CRB}^{-1}(\boldsymbol{\Theta}) = \mathrm{Re}(\mathbf{F}) - \sum_{t=1}^{N} \mathrm{Re}\left[\mathbf{G}^H(t)\mathbf{H}^{-1}\mathbf{G}(t)\right] \tag{5.23}$$

where $\mathbf{F}$, $\mathbf{H}$, and $\mathbf{G}$ are defined in Eqs. (5.18), (5.20), and (5.21), and then for a sufficiently large N the CRB is given by

$$\mathrm{CRB}^{-1}(\boldsymbol{\Theta}) = \frac{2N}{\sigma^2}\mathrm{Re}\left[\mathbf{C} \odot \mathbf{P}^T\right] \text{ for } N \to \infty \tag{5.24}$$

where $\mathbf{C} = \mathbf{D}^H[\mathbf{I} - \mathbf{A}(\mathbf{A}^H\mathbf{A})^{-1}\mathbf{A}^H]\mathbf{D}$. The inversion of Eq. (5.24) is the lower bound of the estimation error of $\boldsymbol{\Theta}$ with respect to the noisy measurement model in Eq. (4.4). □

According to the previous works [28, 29], the best and worst conditions of CRB is relevant to the structure of signal correlation matrix ($\mathbf{P}$). Assuming that the powers of each signals are given and the signal parameters ($\boldsymbol{\Theta}$) are fixed, they summarized the criteria as follows:

KAIST

$C1$**:** The best (worst) case CRB is the one with all diagonal element minimum (maximum).

$C1_i$**:** The best (worst) case CRB is the one with its ith diagonal element minimum (maximum).

$C2$**:** The best(worst) case CRB is the one with minimum (maximum) determinant.

Note that $C1$ condition is stronger than $C1_i$ condition. The criteria convey the structure of CRB matrix. For example, let consider following example

$$\mathrm{CRB}_1 = \begin{bmatrix} 1 & 0 \\ 0 & 1 \end{bmatrix}, \mathrm{CRB}_2 = \begin{bmatrix} 1 & 1-\epsilon \\ 1-\epsilon & 1 \end{bmatrix} \tag{5.25}$$

where $0 < \epsilon \ll 1$. The diagonal elements of both cases are identical, but the scatter ratio of determinants is $(\det(CRB_2)/\det(CRB_1)) \approx 2\epsilon$, which is smaller than one. In general, $C1$ and $C2$ cannot describe the sufficient condition of the best(worst) case CRB alone. Thus in previous work [28], they derived sufficient conditions on the signal correlation matrix, which provides the best CRB condition [28]. We denote

$$\boldsymbol{\Pi} = \{\mathbf{Q} \in \mathbb{C}^{M\times M} : \ \mathbf{Q} \geqslant 0 \text{ and } Q_{ii} > 0 \text{ prespecified}\} \tag{5.26}$$

where $\boldsymbol{\Pi}$ is the set of non-negative definite Hermitian matrices with positive diagonal elements. Then, we start with following lemma.

Lemma 1. *Let* $\mathbf{K} \in \mathbb{C}^{M\times M}$, $\mathbf{K} > 0$, *and* $\mathbf{V}^{-1} = Re[\mathbf{K} \odot \mathbf{Q}]$. *Then* $\forall \mathbf{Q} \in \mathbf{\Pi}$

$$i)\ \mathbf{V}_{ii} \geqslant \frac{1}{\mathbf{Q}_{i|2,i|2}} \left\{ \left[Re(\mathbf{K}) \odot \mathbf{I}_{M\times M} \right]^{-1} \right\}_{ii},\ \textit{for } i = 1, \cdots, M. \tag{5.27}$$

$$ii)\ \det(\mathbf{V}) \geqslant \frac{1}{\left(\prod_{i=1}^{M} \mathbf{Q}_{ii}\right) \det\left[Re(\mathbf{K}) \odot \mathbf{I}_{M\times M} \right]} \tag{5.28}$$

with equality holding in both i) and ii) if the matrix $\mathbf{Q}$ *is diagonal.*

The proof of Lemma 1 is described in Yau and Bresler [28]. Then, we have the following result using Lemma 1.

Theorem 2. *Then the best condition CRB matrix according to either C1 or C2 is obtained satisfying the condition*

$$\mathbf{P}_{ij} = 0 \textit{ for } i \neq j \tag{5.29}$$

and is given by

$$CRB(\mathbf{\Theta}) = \frac{\sigma^2}{2N} [diag(\frac{1}{\sqrt{\mathbf{P}_{ii}}})] Re[\mathbf{C} \odot \mathbf{I}]^{-1} [diag(\frac{1}{\sqrt{\mathbf{P}_{ii}}})]. \tag{5.30}$$

Proof. Let $\mathbf{K} = (2N/\sigma^2)\mathbf{C}$ and $\mathbf{Q} = \mathbf{P}^T$. The best case CRB is obtained when $\mathbf{Q}_{ij} = \mathbf{P}_{ji} = 0$ for $i \neq j$. Then it provides the form of the CRB matrix in Eq. (5.24). □

Note that both criteria $C1$ and $C2$ are satisfied simultaneously in Theorem 2. It means that both bounds of estimation of individual signals and total scatter are minimized when the signals are uncorrelated. When the the signals are uncorrelated, $C1$ is also satisfied with all minimized diagonal elements. Thus Eq. (5.29) is a sufficient condition.. In this case the estimation multiple signals within likelihood function can decouples multiple single source estimation when *ith* and *jth* signals are independent.

5.2 Nano-MUSIC

We now state the asymptotical performance of MUSIC algorithm. According to the Stoica and Arye [30], the variance of the MUSIC estimation error $(\hat{\boldsymbol{\theta}}_i - \boldsymbol{\theta}_i)$ is stated and proved.

Theorem 3. *The variance of MUSIC estimation error is derived as*

$$\begin{aligned} \textsc{Var}_{MU}(\hat{\boldsymbol{\theta}}_i) &= \frac{\sigma^2}{2N} \frac{\sum_{k=1}^{M} \left(\frac{1}{\lambda_k - \sigma^2} + \frac{\sigma^2}{(\lambda_k - \sigma^2)^2} \right) |\mathbf{a}^H(\boldsymbol{\theta}_i)\mathbf{u}_k|^2}{\sum_{k=1}^{L-M} |\mathbf{d}^H \boldsymbol{\theta}_i \mathbf{q}_k|^2} \\ &= \frac{\sigma^2}{2N} \frac{\mathbf{a}^H \boldsymbol{\theta}_i \left(\mathbf{U}\mathbf{\Lambda}\mathbf{U}^H + \sigma^2 \mathbf{U}\mathbf{\Lambda}^{-2}\mathbf{U}^H \right) \mathbf{a}\boldsymbol{\theta}_i}{\mathbf{d}^H \boldsymbol{\theta}_i \mathbf{Q}\mathbf{Q}^H \mathbf{d}(\boldsymbol{\theta}_i)}, \end{aligned} \tag{5.31}$$

where $\mathbf{U} = [\mathbf{u}_1 \cdots \mathbf{u}_M]$ *and* $\mathbf{Q} = [\mathbf{q}_1 \cdots \mathbf{q}_{L-M}]$ *are defined in Eq.* (4.6), $\mathbf{d}(\boldsymbol{\theta}) = \mathbf{da}(\boldsymbol{\theta})/\mathbf{d}\boldsymbol{\theta}$, *and* $\mathbf{\Lambda} \triangleq \mathbf{\Lambda}_s - (\sigma^2)\mathbf{I}$, *where* $\mathbf{\Lambda}_s$ *is also defined in Eq.* (4.6).

From Eq. (4.6), we can write as

$$\mathbf{R}_y = \mathbf{A}\mathbf{P}\mathbf{A}^H + \sigma^2\mathbf{I} = \mathbf{U}\mathbf{\Lambda}_s\mathbf{U}^H + \sigma^2\mathbf{Q}\mathbf{Q}^H = \mathbf{U}\mathbf{\Lambda}\mathbf{U}^H + \sigma^2\mathbf{I} \tag{5.32}$$

which implies

$$\mathbf{A}\mathbf{P}\mathbf{A}^H = \mathbf{U}\mathbf{\Lambda}\mathbf{U}^H \tag{5.33}$$

$$\mathbf{A}\mathbf{P}\mathbf{A}^H\mathbf{A}\mathbf{P}\mathbf{A}^H = \mathbf{U}\mathbf{\Lambda}^2\mathbf{U}^H, \tag{5.34}$$

and therefore

$$(\mathbf{U}^H\mathbf{A})\mathbf{P}(\mathbf{A}^H\mathbf{U}) = \mathbf{\Lambda} \tag{5.35}$$

$$(\mathbf{U}^H\mathbf{A})\mathbf{P}(\mathbf{A}^H\mathbf{A})\mathbf{P}(\mathbf{A}^H\mathbf{U}) = \mathbf{\Lambda}^2. \tag{5.36}$$

Since the columns of $\mathbf{A}$ lie in the column space of $\mathbf{U}$, and $\mathbf{A}$ has full rank, it means that the matrix $\mathbf{U}^H\mathbf{A}$ is non-singular and

$$\mathbf{U}\mathbf{U}^H = \mathbf{A}(\mathbf{A}^H\mathbf{A})^{-1}\mathbf{A}. \tag{5.37}$$

The non-singular of $\mathbf{U}^H\mathbf{A}$ implies that

$$(\mathbf{A}^H\mathbf{U})\mathbf{\Lambda}^{-1}(\mathbf{U}^H\mathbf{A}) = \mathbf{P}^{-1} \tag{5.38}$$

$$(\mathbf{A}^H\mathbf{U})\mathbf{\Lambda}^{-2}(\mathbf{U}^H\mathbf{A}) = \mathbf{P}^{-1}(\mathbf{A}^H\mathbf{A})^{-1}\mathbf{P}^{-1}. \tag{5.39}$$

Using above equations, we acquire

$$\text{VAR}_{MU}(\hat{\boldsymbol{\theta}}_i) = \frac{\sigma^2}{2N}\frac{\left[\mathbf{P}^{-1}\right]_{ii} + (\sigma^2)\left[\mathbf{P}^{-1}(\mathbf{A}^H\mathbf{A})^{-1}\mathbf{P}^{-1}\right]_{ii}}{h(\boldsymbol{\theta}_i)}, \tag{5.40}$$

where $\mathbf{h}(\boldsymbol{\theta}) = \mathbf{d}^H(\boldsymbol{\theta})\left[\mathbf{I} - \mathbf{A}(\mathbf{A}^H\mathbf{A})^{-1}\mathbf{A}^H\right]\mathbf{d}(\boldsymbol{\theta})$, and from Eq. (5.24) CRB is given by

$$\text{VAR}_{CR}(\hat{\boldsymbol{\theta}}_i) = \frac{\sigma^2}{2N}\left[\left\{\left[\mathbf{D}^H\left[\mathbf{I} - \mathbf{A}(\mathbf{A}^H\mathbf{A})^{-1}\mathbf{A}^H\right]\mathbf{D}\right] \odot \mathbf{P}^T\right\}^{-1}\right]_{ii}. \tag{5.41}$$

Finally, in uncorrelated signal case where $\mathbf{P}$ is diagonal matrix, Eqs. (5.40) and (5.41) are reduced to

$$\text{VAR}_{MU}(\hat{\boldsymbol{\theta}}_i) = \frac{1}{2N\cdot\text{SNR}_i}\left[1 + \frac{\left[(\mathbf{A}^H\mathbf{A})^{-1}\right]_{ii}}{\text{SNR}_i}\right] \Big/ h(\boldsymbol{\theta}_i), \tag{5.42}$$

$$\text{VAR}_{CR}(\hat{\boldsymbol{\theta}}_i) = \left(\frac{1}{2N\cdot\text{SNR}_i}\right)/h(\boldsymbol{\theta}_i). \tag{5.43}$$

where $\text{SNR}_i = \mathbf{P}_{ii}/\sigma^2$. From the MUSIC variances and CRB, the efficiency of MUSIC algorithm is written as follows

$$\frac{\text{VAR}_{MU}(\hat{\boldsymbol{\theta}}_i)}{\text{VAR}_{CR}(\hat{\boldsymbol{\theta}}_i)} = 1 + \frac{\left[(\mathbf{A}^H\mathbf{A})^{-1}\right]_{ii}}{\text{SNR}_i}, \tag{5.44}$$

and when the diagonal elements of signal correlation matrix ($\mathbf{P}$) are large values, the performance of MUSIC algorithm achieves the CRB.

We investigated the best efficiency case of MUSIC algorithm in Eq. (5.44). As shown in CRB conditions in Eq. (5.30), when the target signals are uncorrelated, the performance of MUSIC algorithm approaches CRB, and under this condition, the fundamental limit of CRB also attains the best case CRB. According to previous Chapter, the signal correlation matrix in the nano-MUSIC system is not perfect diagonal matrix. Even though the correlation of scattering field of diffusor has delta correlation, it is blurred by illumination optics from Eq. (4.16). Thus, fluorescence signal correlation matrix corresponding to excitation field on specimen has off-diagonal elements, and it does not satisfy the best conditions of MUSIC and CRB. However, as shown in previous Chapter, the proposed l_∞-MUSIC increase the performance compared to conventional l_2-MUSIC in nanoscopic imaging. We can reduce the effect of illumination optics in some other ways too. Nano-MUSIC system based on conventional optical microscopy exploits far-field illumination optics as well as imaging optics. If we implement near-field optical techniques such as TIRFM, the effect of illumination optics should be reduced, since the illumination fields to excite fluorescence probes are within sub-diffraction limit.

KAIST

Chapter 6. Experimental Results

6.1 Implementation

The proposed nano-MUSIC system can easily be implemented by modifying conventional epi-fluorescence microscopy. The epi-illumination microscopy is suitable for the generation of a diffraction limited speckle pattern because of the identical optics in illumination and detection. To obtain a speckle pattern in illumination optics, we applied a rotatable diffusor with a rough surface on motorized rotation stage. As shown in Fig. 4.3, by changing the rotation angle of a static diffusor in the epi-illuminator, dynamic randomized speckle patterns can be generated on the sample plane.

Figure 6.1 illustrates a nano-MUSIC system using Olympus IX71 microscopy by modifying the epi-fluorescence illuminator. In this figure, a low power 532nm continuous wave diode pumped solid state laser (SDL-532-500, Shanghai Dream Lasers Technology) was used to generate a speckle pattern on samples through a ND filter. The excitation laser is illuminated to the rotatable diffusor through an expansion lens (herein, $L_I = -25mm$), and the scattered light collected by a pair of lenses (L_1 and L_2) was passed through the excitation filter (BP530-550, Olympus), and then focused on the back focal plane of the objective lens 100X oil-immersion lens with 1.30 NA(UIS2, Olympus) reflected by a dichroic mirror (DM570, Olympus). The fluorescence emission light was collected by the identical objective lens, and the collected light was filtered by a dichroic mirror (DM570, Olympus) and an emission high-pass filter (BA575IF, Olympus). Using a function generator (AFG310, Tektronix), we controlled the synchronization between the rotation of the diffusor (1000 pulse per revolution) and the imaging acquisition time of the EM-CCD camera (Luca-S, Andor) that has the $10\mu m$ pitch. The frame rate of the camera was 10 Hz; so for 1000 snapshots, the total acquisition time was about two minutes. We prevented lateral and axial directional drifts of the specimen by locking a handmade screw to the coaxial fine focusing knob of the microscopy. In front of the camera, either 1X or 1.6X tube lens (L_T) for IX71 with a camera adaptor lens (U-TV1X-2 with U-CMAD3, Olympus) was used. To acquire 62.5nm (31.25nm by post-processing) pitch per a pixel, we adjusted the magnifications of the optics to 160X.

For confocal imaging, we used a confocal laser scanning microscope (CLSM) (LSM510; Carl Zeiss; Jena, Germany) with a 40X/0.90 NA multi-immersion objective lens (water, oil, glycerin; PLAN NEOFLUAR; Carl Zeiss).

6.2 Methods and Materials

6.2.1 Phantom preparation

Nano particle

For quantitative analysis, we prepared specimens of fluorescent silica shelled nanoparticles (CELL STALKER™CSR, Biterials) which contain rhodamine B isothiocyante (RITC, Ex/Em = 515nm / 578nm). Moreover, SEM (scanning electron microscope) images were obtained with grid patterned substrate (μ-Dish^{35mm} grid-500 ibiTreat, Ibidi) on coverslip-like thickness. The grid structure has 400 squares of $500\mu m$ side length with $40 \pm 5\mu m$ grooves. The grid was designed to localize the nanoparticles. To achieve the uniform dispersion of the nanoparticles, the substrate was rinsed with distilled water, dried by filtered dry air and treated by oxygen plasma (60sec at medium power of Harrick Scientific plasma cleaner) for a hydrophilic surface with a low contact angle. Then, we mounted the substrate vertically and let flow the diluted nanoparticle solution over the substrate(1:9, nanoparticle (2mg/ml) in DI water) by pipetting it.

Nano pattern

Radial nanowires with fluorescent dyes were prepared to evaluate the optical lateral resolution. A hydrogen silsesquioxane (HSQ, negative tone electron-beam resist) was firstly mixed with Rhodamine 6G dyes and then spin-coated on a glass substrate. The radial patterns with 100nm line width are defined by electron-beam lithography.

Table 6.1: Specifications of radial nano-patterns

	Nano-pattern 1	Nano-pattern 2	Nano-pattern 3
Line width	$100nm$	$100nm$	$100nm$
Min. distance	$120nm$	$80nm$	$60nm$
Max. distance	$500nm$	$500nm$	$500nm$
Number of lines	15	19	21

6.2.2 HeLa cell preparation

Reagents and Constructs

Antibodies against Cytochrome-c and Tom20 (for Mitochondria) and Calnexin (for ER) were purchased from BD Biosciences. Phalloidin-TRITC (for F-actin), Fluor 594-conjugated goat anti-mouse, and goat anti-rabbit IgG were purchased from Molecular Probes (Eugene, OR, USA). DsRed-Mito and DsRed-ER were used as probes specific for mitochondria and ER.

Immunofluorescences

HeLa cells were grown in Dulbecco's complete medium (JBI) supplemented with 10% heat-treated

fetal calf serum (Invitrogen), 100 U/mL penicillin, and 100 µg/mL streptomycin. For immunostaining, cells grown in the culture dish with cover glasses were fixed with 4% paraformaldehyde for 15 min at room temperature, permeabilized with 0.15% Triton X-100 in PBS for 15 min at room temperature, and then blocked with 3% bovine serum albumin in PBS for 45 min at room temperature. The cover glasses with cells were incubated for 2 hr with indicated primary antibodies on figures. After washing with PBS, the glasses were incubated for 1 hr with goat anti-IgG conjugated with 594 as the secondary antibody. The cover glasses were mounted with fluorescent mounting medium (Dako). For analysis of bio-fluorescence, the cells grown in the culture dish with cover glasses were transfected with DsRed-ER and DsRed-Mito plasmid by Effectene reagent (Qiagen, Hilden, Germany), respectively. After 15 hr, cells were fixed with 4% paraformaldehyde for 15 min at room temperature. After washing with PBS, The cover glasses were mounted with fluorescent mounting medium (Dako).

6.3 Reconstruction results

For quantitative analysis to characterize the resolution, we prepared ultra-structures using nano particles and nano patterns. To verify the reconstruction results, we also acquired scanning electron microscopy (SEM) images of the phantoms.

KAIST

In Fig. 6.2, we performed experiments using $50nm$ silica fluorescence nano-particles. To acquire a mono layered structure, we prepared the nano particles as described in previous Section. In Fig. 6.2(a), along with dashed lines 1-3, the distance between aggregated particles are $70nm$, $83nm$, and $55nm$. The locations of each structure can be confirmed by the profiles in Fig. 6.2(d-f). Compared with a conventional image in Fig. 6.2(b), nano-MUSIC reconstructed the structures more clearly. In Fig. 6.3(a), there exists an empty space surrounded by nano particles. Along with dashed line 2, the width of the empty space is $\sim 170nm$ and the the widths of other two fluorophores are $174nm$ and $65nm$, respectively. As illustrated in Fig. 6.4(d), nano-MUSIC resolved the empty space as well as the $65nm$ fluorophore probe, whereas the space is not revealed in an conventional microscopy image. In Fig. 6.4, we again observed that nano-MUSIC outperforms the conventional fluorescence microscopy. Additionally, in Fig. 6.5, the reconstructed large field-of-view of randomly aggregated $50nm$ nano particles is presented. In the magnified images (Fig. 6.5(d-f)) of white boxes in left columns, we reconstructed the single particle indicated by dashed line. The actual size of the single particle is roughly $100nm$ which is manually measured from SEM image, and the reconstructed size of the particle is $90nm$. Based on the aforementioned nano particle experimental results, nano-MUSIC achieved $65nm$ lateral resolution and 3.4-fold resolution improvement over the diffraction limit ($\lambda_{em}/2\mathrm{NA}_{oil}$).

Next, we prepared three types of radial nano-patterns that have different specifications as illustrated in Table 6.1. We firstly reconstructed the patterns that have a $120nm$ minimum distance. As illustrated

in Fig. 6.6(c), 15 patterns are placed equi-angularly. Compared with the conventional image in Fig 6.6(a), the nano-MUSIC image in Fig. 6.6(b) reveals 15 patterns more clearly as seen by the SEM image. To quantify the reconstruction result, Figs. 6.6((d) and (e)) illustrates the profiles along dashed arcs 1 and 2, respectively. The distances in each arc are $166nm$ and $376nm$, respectively. In the latter case ($m = 376nm$), the patterns are well resolved in both conventional and nano-MUSIC images since the distance is longer than the diffraction limit. However, in the former case ($m = 166nm$), the patterns are not resolved in the conventional image, whereas nano-MUSIC resolved patterns directed by arrows in Fig. 6.6(d). Additionally, in Fig. 6.7, 19 patterns are radially equi-spaced. Similar to the first results, the profiles corresponding to dashed arc 1 and 2 are illustrated in Figs. 6.7((d) and (e)), respectively. In Fig. 6.7(e), nano-MUSIC well resolved the patterns with the distance ($m = 178nm$) while conventional patterns are not revealed. For a more closed distance case ($m = 134nm$), nano-MUSIC still resolved patterns directed by the arrow in Fig. 6.7(d).

Finally, we experimented the last radial nano pattern which has the minimum distance ($60nm$). The profiles along dashed arc 1 and 2 are illustrated in Figs. 6.8((d) and (e)), respectively. In the arc 1 case ($m = 125nm$), nano-MUSIC can still resolve it as shown in Fig. 6.8(d). Based on the radial nano-pattern experimental results, the minimum resolvable distance between patterns is $125nm$.

Next, we visualized the sub-cellular structure of a HeLa cell such as actin filament (F-actin), endoplasmic recticulum (ER) (Fig. 6.9), and mitochondrial network (Fig. 6.10) using nano-MUSIC. The detailed preparation is described in previous Section.

The F-actin as a polymerization of actin proteins forms the cytoskeleton of eukaryotic cells such as HeLa cells [65, 66]. The F-actin of 7nm diameter is organized as a fiber bundle or a mesh structure with an actin-binding protein. As shown in Fig. 6.11, the fiber bundles of F-actin are widely distributed on the cytoplasm of a cell. To observe the overall structure of the cell, we acquired the measurements of the specimen stained by Phalloidin at a low magnification objective lens (40X, 0.75NA). To compare the reconstruction result, we also acquired the same area by confocal microscopy as shown in Fig. 6.11(b). As shown in the inset image in Fig. 6.11(b), the resolution of confocal microscopy is better than conventional fluorescence microscopy in Fig. 6.11(a). However, l_2-MUSIC and l_∞-MUSIC results in Figs. 6.11((c) and (d)) provide better resolution images than confocal image and reveal detailed structures of a F-actin bundle. In this experimental results, the reconstruction results of l_∞-MUSIC (Fig. 6.11(c)) and l_2-MUSIC (Fig. 6.11(d)) provide similar results due to the small NA lens. When we observe F-actin in filopodia using an oil-immersion lens (100X, 1.30NA) that is stretched to the outside of the cell, we can find that the blurred structure of F-actin is well resolved in our reconstruction images as shown in the insets of Fig. 6.12(a-c). Moreover, the result of l_∞-MUSIC provide more detailed structural information than that of l_2-MUSIC.

The ER is constituted by a network of branched tubules and flattened sacs in cytosol as shown in Fig. 6.9 [65, 66]. Since they are interconnected and convolut each other continuously, the conventional

image of ER looks like a diffused structure as shown in Figs. 6.13(a) and 6.14(a). We first stained Calnexin in ER with a fluorescent dye. Compared to conventional fluorescence microscope images, l_2 and l_∞-nano-MUSIC provides more accurate structural information as shown in Figs. 6.13((b) and (c)), and 6.14((b) and (c)). In Figs. 6.13(a-c), even though the ER network nearby nucleus (white line box) is more diffused than the outside (white dash line box) in fluorescence microscope images, accurate structures are also visible in the nano-MUSIC images. More detailed structures can be found in magnified images in Figs. 6.13(g-i). In ER reconstruction results, we also verified that l_∞-MUSIC is better than l_2-MUSIC. Additionally, when we applied to the fluorescence protein (DsRed-ER) stained case in Fig. 6.14, the reconstruction image also provided valuable structural information of ER.

The Mitochondrion has a diameter of $200 \sim 400nm$, and also has a matrix structure surrounded by inner membrane as shown in Fig. 6.10 [65, 66]. To visualize the mitochondrial network of a HeLa cell, we first stained Tom20 of the translocase of the mitochondrial outer membrane (TOM) complex. The reconstruction images in Figs. 6.15((b) and (c)) for outer membrane reveal sub-diffraction limited resolution of the outer membrane network, and the detailed structures are shown in Figs. 6.15(d-i).

Next, we stained inner membrane as a red fluorescence protein (DsRed-mito). The reconstruction image in Figs. 6.16((b) and (c)) reveals the accurate structure of mitochondria comparing with the conventional image (Fig. 6.16(a)). In magnified images (Figs. 6.16(d) and (e)) of the conventional image, the inner structure of mitochondria looks like a smooth tubule whereas the reconstruction images in Figs. 6.16(f-i) show uneven structures of a tubule due to the matrix structure in the inner membrane. Finally, we stained cytochrome-c as a peripheral protein, which is attached on the outer surface of the inner membrane. The magnified images (Figs. 6.17((f) and (j)) for l_∞-nano-MUSIC and Figs. 6.17((g) and (k)) for l_2-nano-MUSIC) show rough tubule structures comparing to the conventional (Figs. 6.17(d) and (h)) and confocal (Figs. 6.17(e) and (i)) results. The reconstruction images (Figs. 6.16 and 6.17) of mitochondrial experiments provide a detailed structure of the inner membrane. Based on the experimental results, we can see that nano-MUSIC can be applied to any types of fluorescent probes, proteins, or staining methods.

Additionally, speckle illumination was also implemented for optical sectioning and quasi-confocal microscopy [37, 38, 39, 40] by exploiting the incoherency of speckle fields between focus and out-of-focus planes. According to the previous work, applying the randomized speckle patterns achieved quasi confocal optical sectioning performance with the axial resolution of $5.4n\lambda/NA^2$. When applied oil-immersion 100X lens with 1.30 NA, the corresponding axial resolution is about $1.85 \sim 2.8\mu m$ for $n = 1 \sim 1.5$. Moreover, when the dynamic speckle patterns are formed by a translation stage, they achieved better axial resolution than randomized patterns. Using this, they achieved near-confocal microscopy performance. Comparing with previous optical sectioning performance, we can see nano-MUSIC can also increase the axial resolution. Using a manually controlled stage, we increased the focal plane $1\mu m$ step by step. The reconstruction results are shown in Fig. 6.18, and the projection images of stacked images are also

shown in Fig. 6.19. In Fig. 6.18, left, center and right columns are conventional, variance and l_2-nano-MUSIC images, respectively. Compared to the conventional and variance images, nano-MUSIC removes the defocused effects and presents F-actin connections more clearly. From this result, we assume that F-actin either grows up by itself or covers up an existing structure. Based on the anatomy of a eukaryotic cell in Fig. 1.1, we suggest that F-actin is growing up by surrounding the nucleus, which has the height of $\sim 4\mu m$. While the quasi-confocal microscopy does not provide perfect optical sectioning, nano-MUSIC clearly removes interference from other layers. Based on the optical sectioning result, we can readily extend nano-MUSIC to 3-dimensional imaging by using the motorized precision z-axis stage.

KAIST

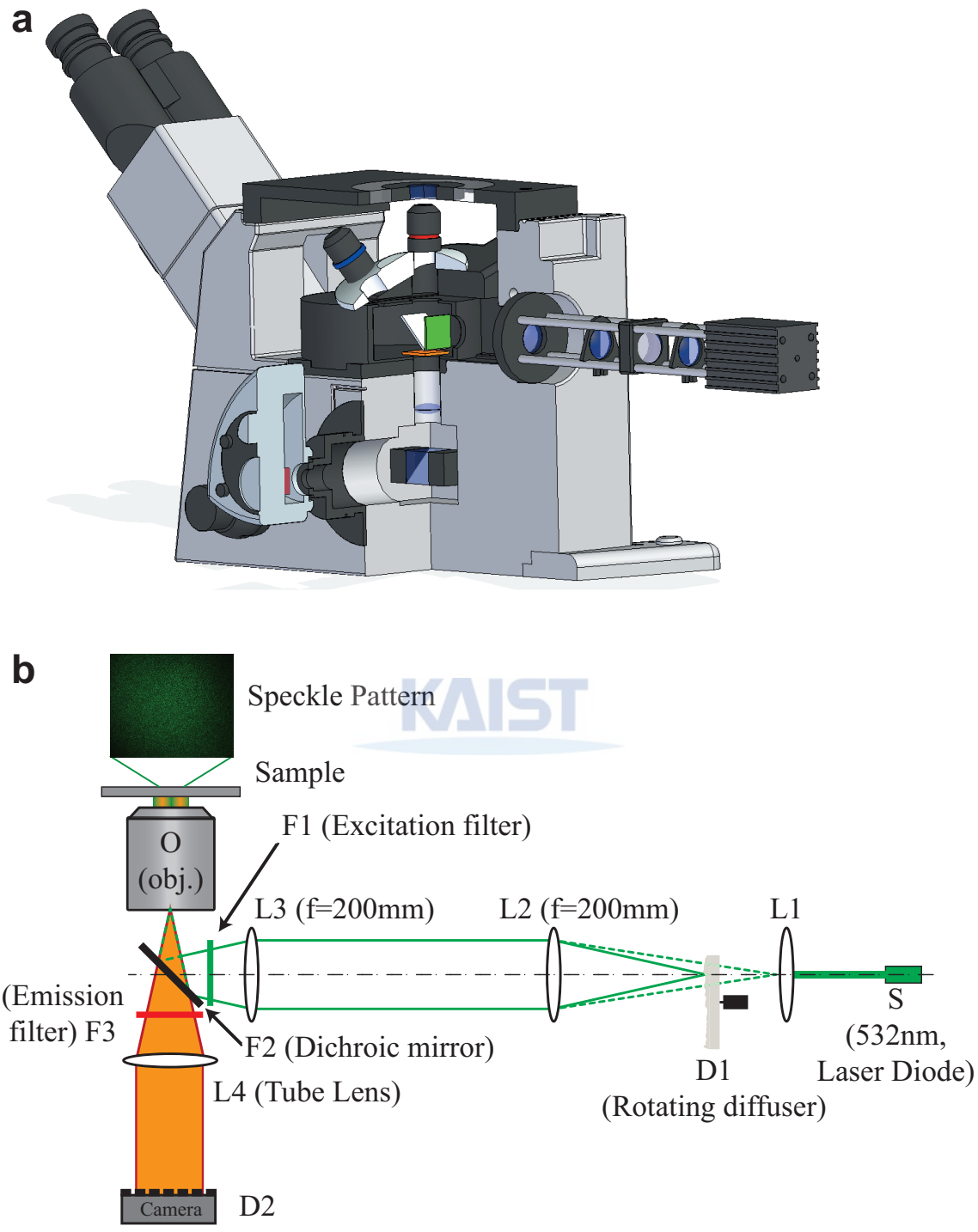

Figure 6.1: The proposed optical system of modified epi-fluorescence microscopy. (a) The implementation of nano-MUSIC on conventional epi-fluorescence microscopy. (b)An excitation laser (S) is scattered by the diffusor (D1) in front of illumination optics (L1-L3), and then the scattered light is focused on the sample plane by the objective lens (O). The emission fluorescence signal is going back through the dichroic mirror (F2) and emission filter (F3) set and also magnified with the tube lens (L4) in front of the detector (D2).

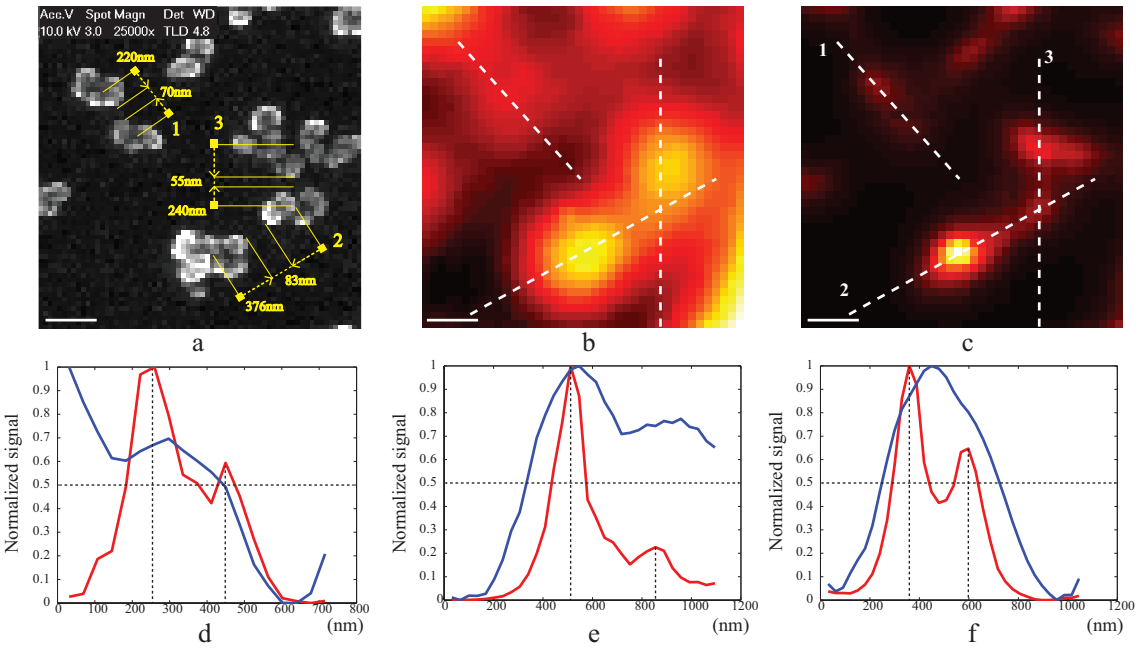

Figure 6.2: Experimental result of silica nano-particles with RITC. (a-c) SEM, conventional, and nano-MUSIC images of phantom 1, respectively, (d-f) blue and red line profiles represent line numbers 1-3 in (b) and (c), respectively. Scale bars in (a-c) are 200nm.

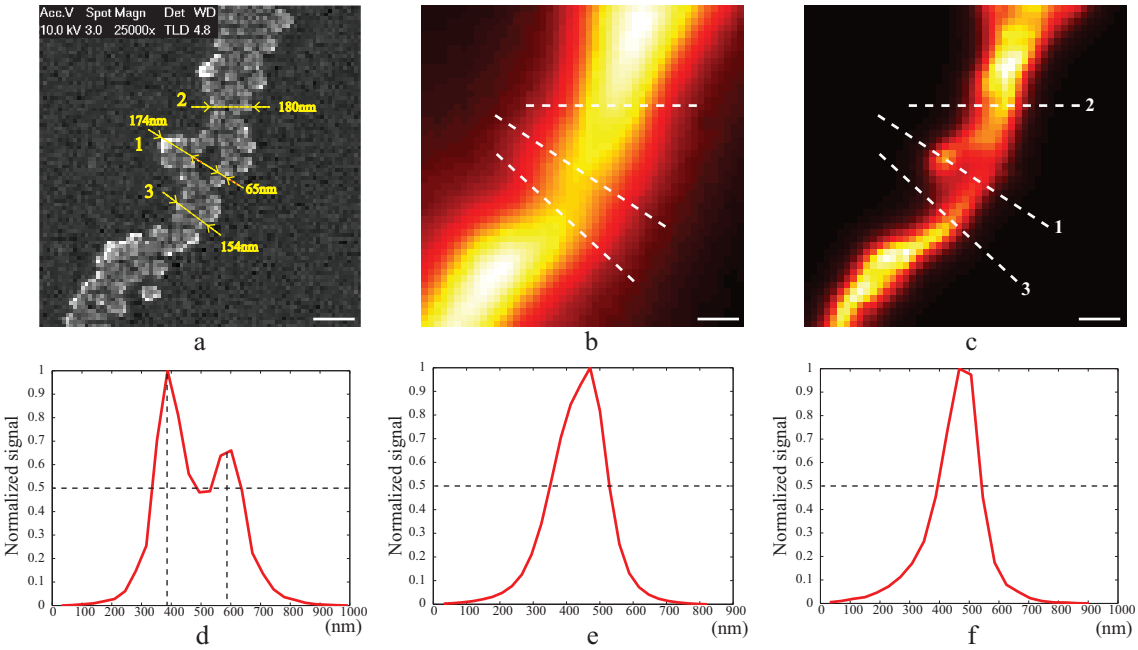

Figure 6.3: Experimental result of silica nano-particles with RITC. (a-c) SEM, conventional, and nano-MUSIC images of phantom 2, respectively, (d-f) line profiles represent line numbers 1-3 in (c), respectively. Scale bars in (a-c) are 200nm.

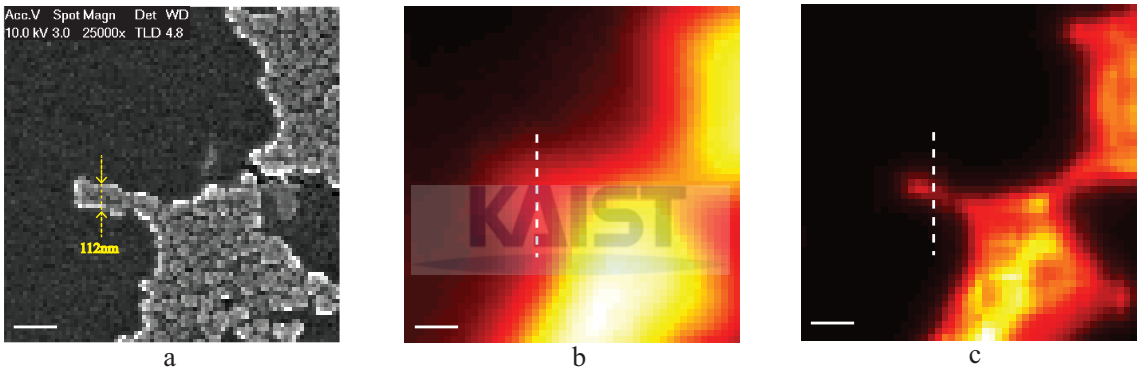

Figure 6.4: Experimental result of silica nano-particles with RITC. (a-c) SEM, conventional, and nano-MUSIC images of phantom 3, respectively. Scale bars in (a-c) are $200nm$.

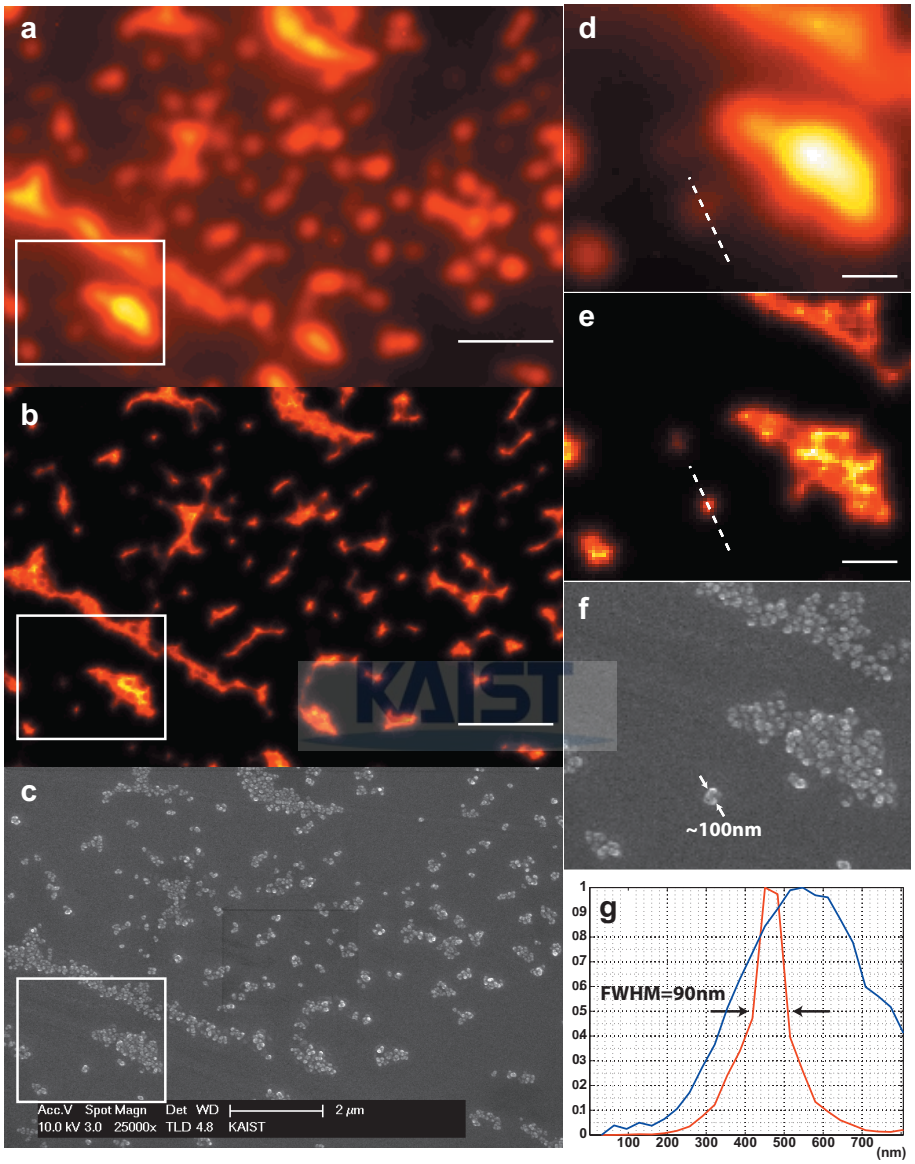

Figure 6.5: Experimental result of silica nano-particles with RITC. (a-c) Conventional, nano-MUSIC, and SEM images of randomly scattered nano particles, (d-f) magnified images of the white line box in (a-c), respectively, (g) line profile of dashed lines in (d) and (e). Blue and red lines represent conventional and nano-MUSIC results, respectively. The FWHM of the single particle is measured $\sim 90nm$ where the real size of this particle is $\sim 100nm$ in SEM image (f). Scale bars in (a-b) and (d-e) are $2\mu m$ and $500nm$, resepectively.

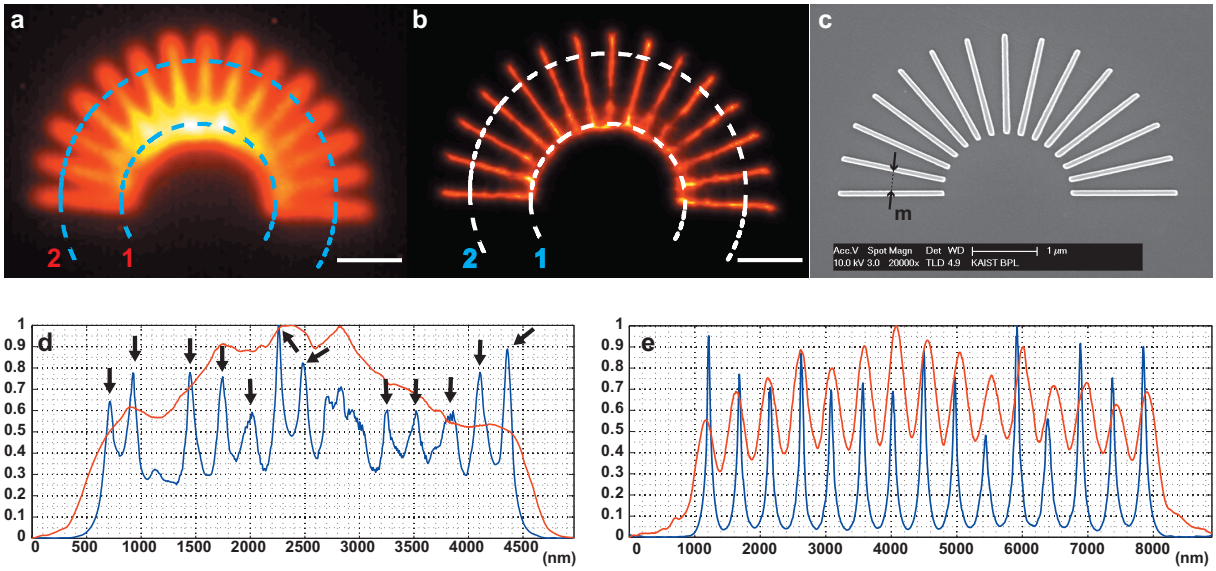

Figure 6.6: Experimental result of a nano pattern with a minimum distance (m) of $120nm$. (a-c) Conventional, nano-MUSIC, and SEM images, respectively, (d-e) arc profiles along the character 1-2 in (a) and (b). Red and blue lines are conventional and nano-MUSIC profiles, respectively. Scale bars in (a-b) are $1\mu m$

KAIST

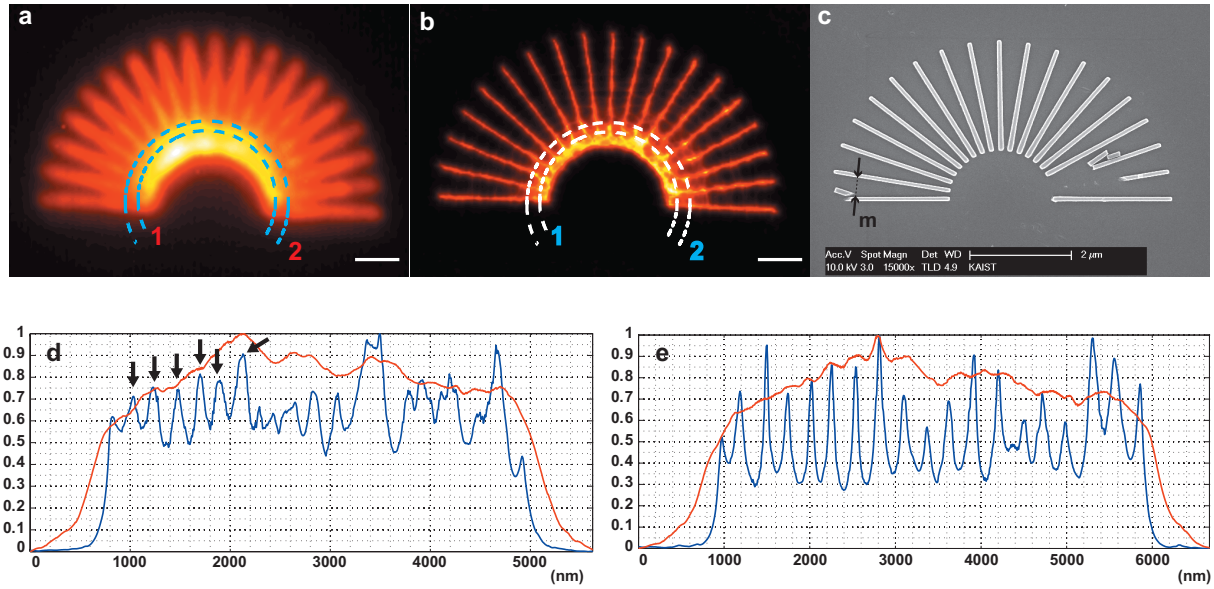

Figure 6.7: Experimental result of a nano pattern with a minimum distance (m) of $80nm$. (a-c) Conventional, nano-MUSIC,SEM images, respectively, (d-e) arc profiles along the character 1-2 in (a) and (b). Red and blue lines are conventional and nano-MUSIC profiles, respectively. Scale bars in (a-b) are $1\mu m$

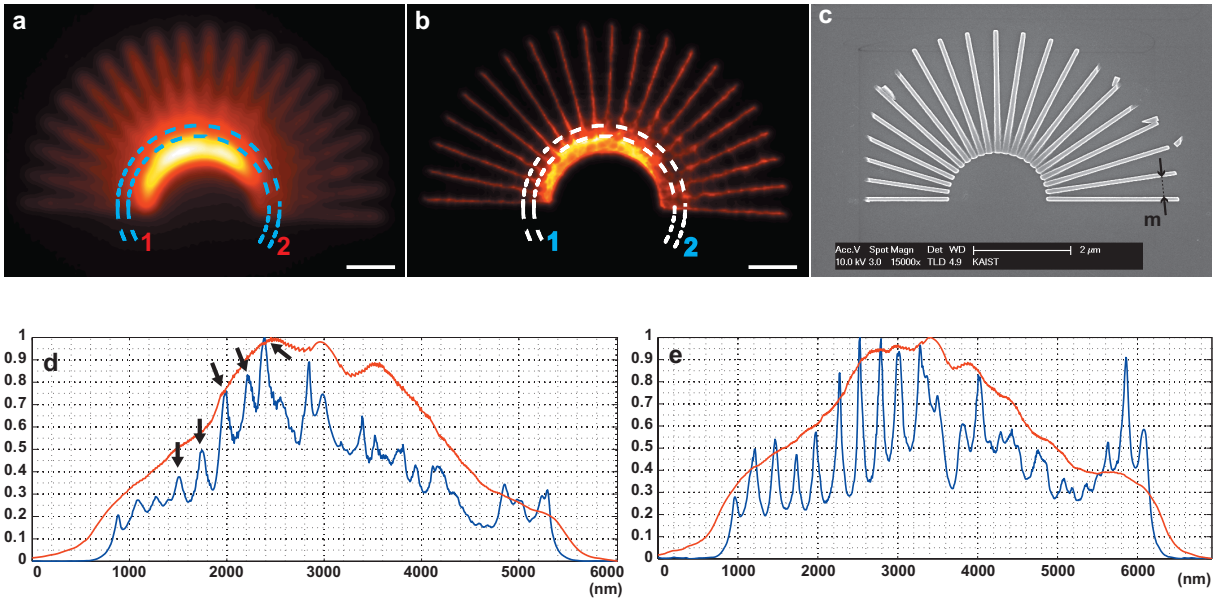

Figure 6.8: Experimental result of a nano pattern with a minimum distance (m) of $60nm$. (a-c) Conventional, nano-MUSIC, SEM images, respectively, (d-e) arc profiles along the character 1-2 in (a) and (b). Red and blue lines are conventional and nano-MUSIC profiles, respectively. Scale bars in (a-b) are $1\mu m$

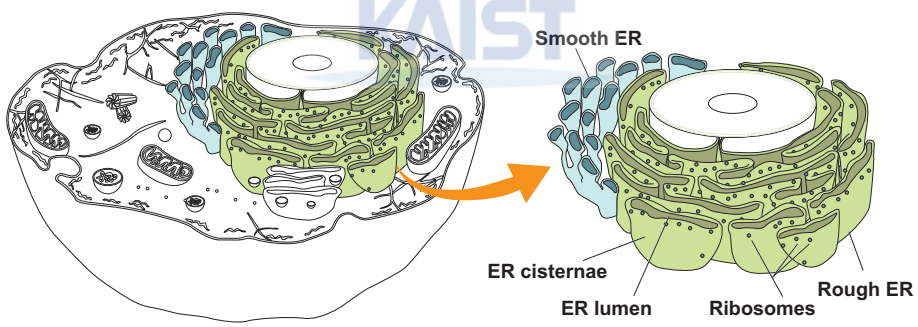

Figure 6.9: Structures of smooth and rough endoplasmic recticulum consist of ER cisternae, ER lumen, and ribosomes.

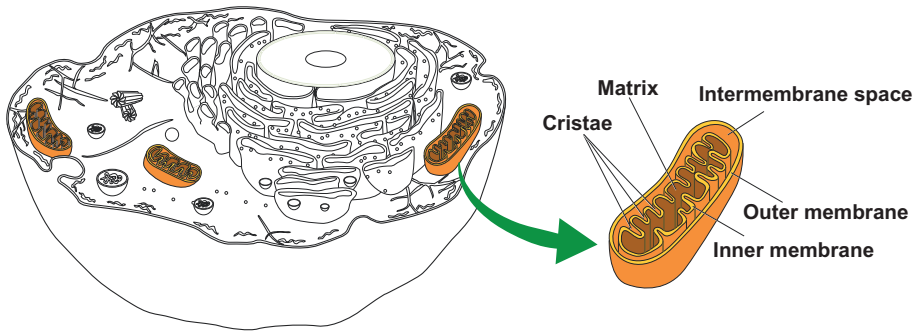

Figure 6.10: A mitochondrion structure consist of outer and inner membrane, inter-membrane space, and matrix.

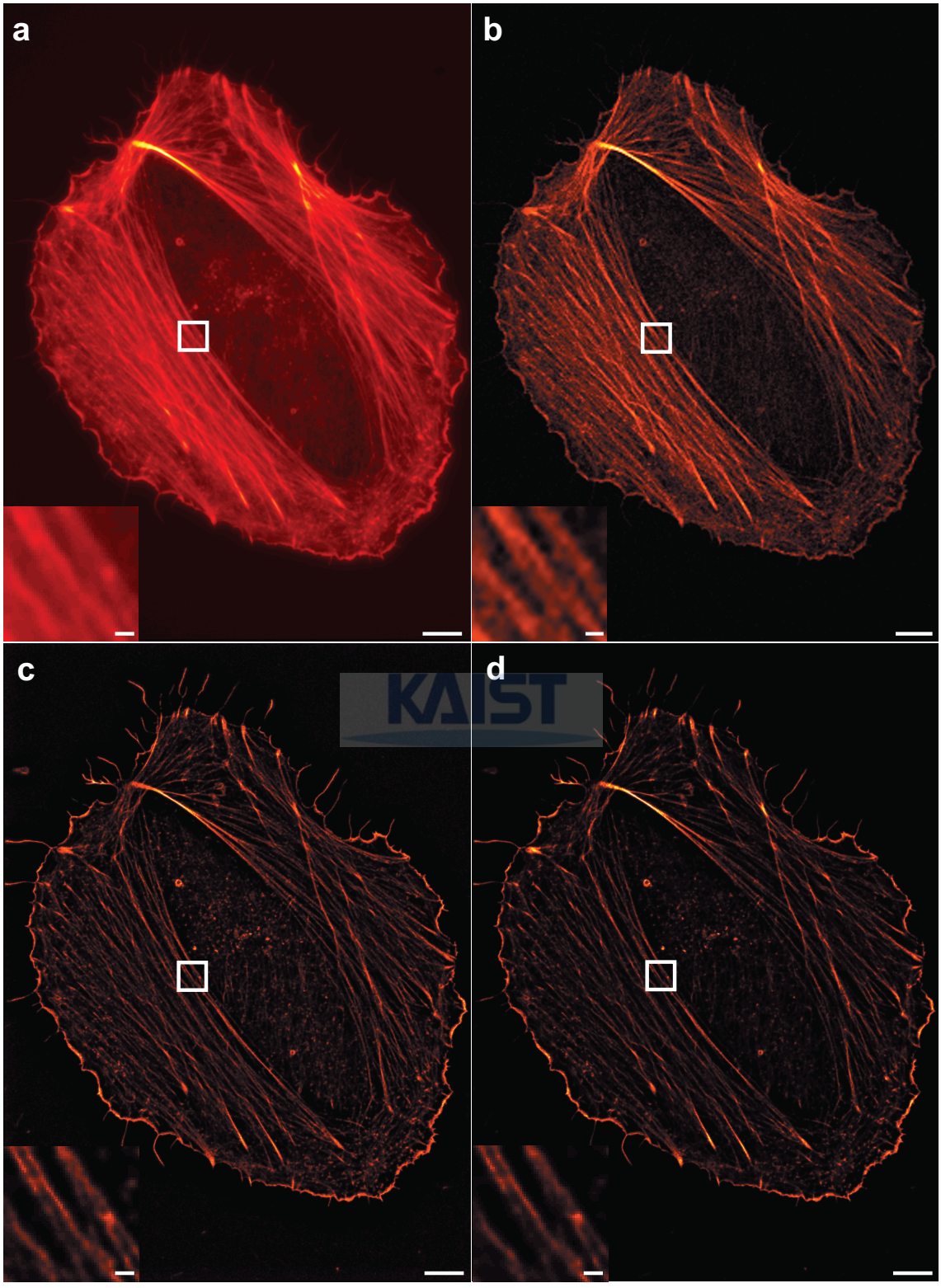

Figure 6.11: The experimental result of F-actin stained with a fluorescent dye. (a) Conventional image generated by a mean image of measured snapshots. (b) Confocal image of (a). (c) l_∞-MUSIC reconstruction image of (a). (d) l_2-MUSIC reconstruction image of (a). The white boxes in (a-d) are magnified in the inset images of (a-d). Scale bars in (a-d) and insets of (a-d) are $10\mu m$ and $1\mu m$, respectively.

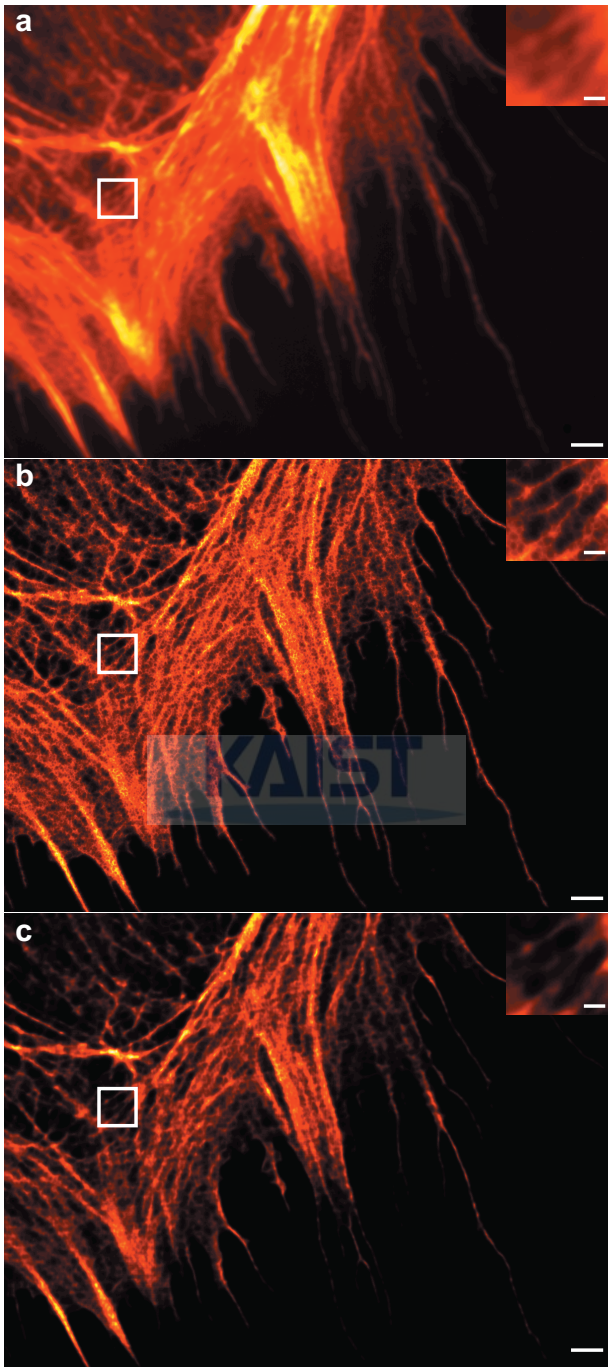

Figure 6.12: The experimental result of F-actin in filopodia stained with a fluorescent dye. (a) Conventional image generated by a mean image of measured snapshots. (b) l_∞-MUSIC reconstruction image of (a). (c) l_2-MUSIC reconstruction image of (a). The white boxes in (a-c) are magnified in the inset images of (a-c), respectively. Scale bars in (a-c) and insets of (a-c) are $2\mu m$ and $500nm$, respectively.

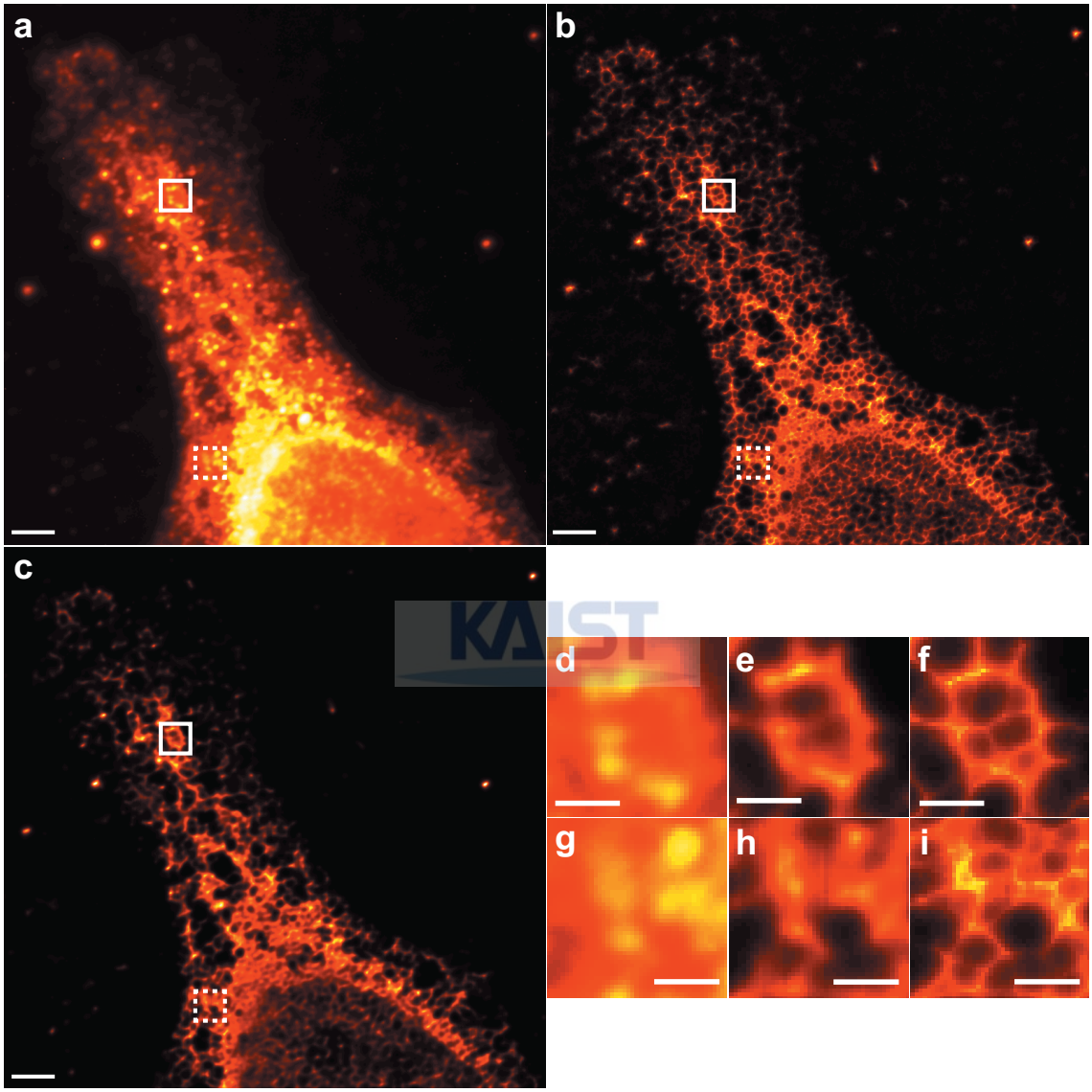

Figure 6.13: The experimental result of ER stained with a fluorescent dye. (a) Conventional image generated by a mean image of measured snapshots. (b) l_∞-MUSIC reconstruction image of (a). (c) l_2-MUSIC reconstruction image of (a). (d-f) Magnified images of the white line boxes in (a-c). (g-i) Magnified images of the white dash line boxes in (a-c). Scale bars in (a-c) and (d-i) are $2\mu m$ and $500nm$, respectively.

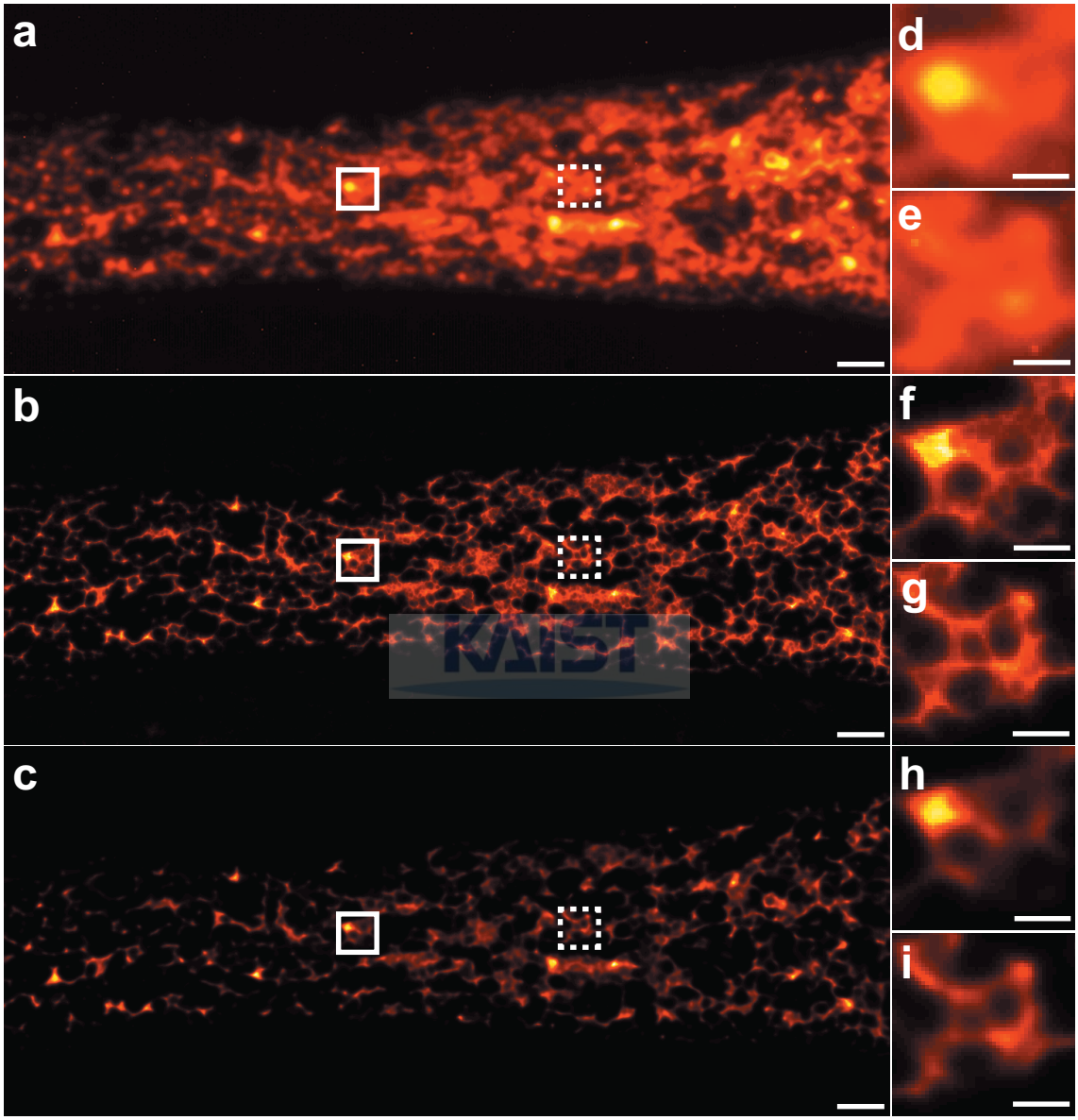

Figure 6.14: The experimental result of ER stained with a fluorescent protein (DsRed-ER). (a) Conventional image generated by a mean image of measured snapshots. (b) l_∞-MUSIC reconstruction image of (a). (c) l_2-MUSIC reconstruction image of (a). (d, f, and h) Magnified images of the white line boxes in (a-c). (e, g, and i) Magnified images of the white dash line boxes in (a-c). Scale bars in (a-c) and (d-i) are $2\mu m$ and $500nm$, respectively.

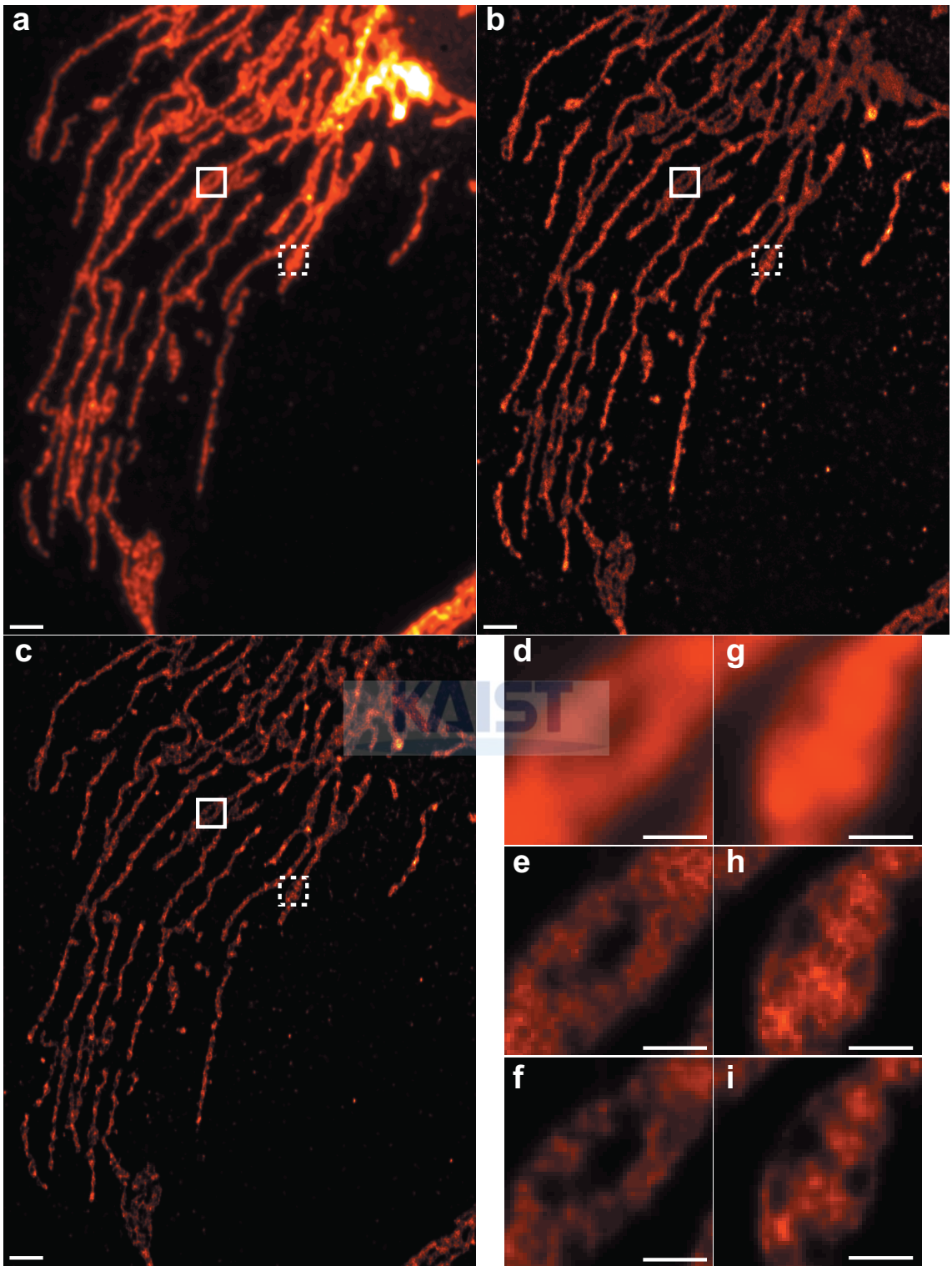

Figure 6.15: The experimental result of mitochondria stained of Tom20 with a fluorescent dye. (a) Conventional image generated by a mean image of measured snapshots. (b) l_∞-MUSIC reconstruction image of (a). (c) l_2-MUSIC reconstruction image of (a). (d-f) Magnified images of the white line boxes in (a-c). (g-i) Magnified images of the white dash line boxes in (a-c). Scale bars in (a-c) and (d-i) are $2\mu m$ and $500nm$, respectively.

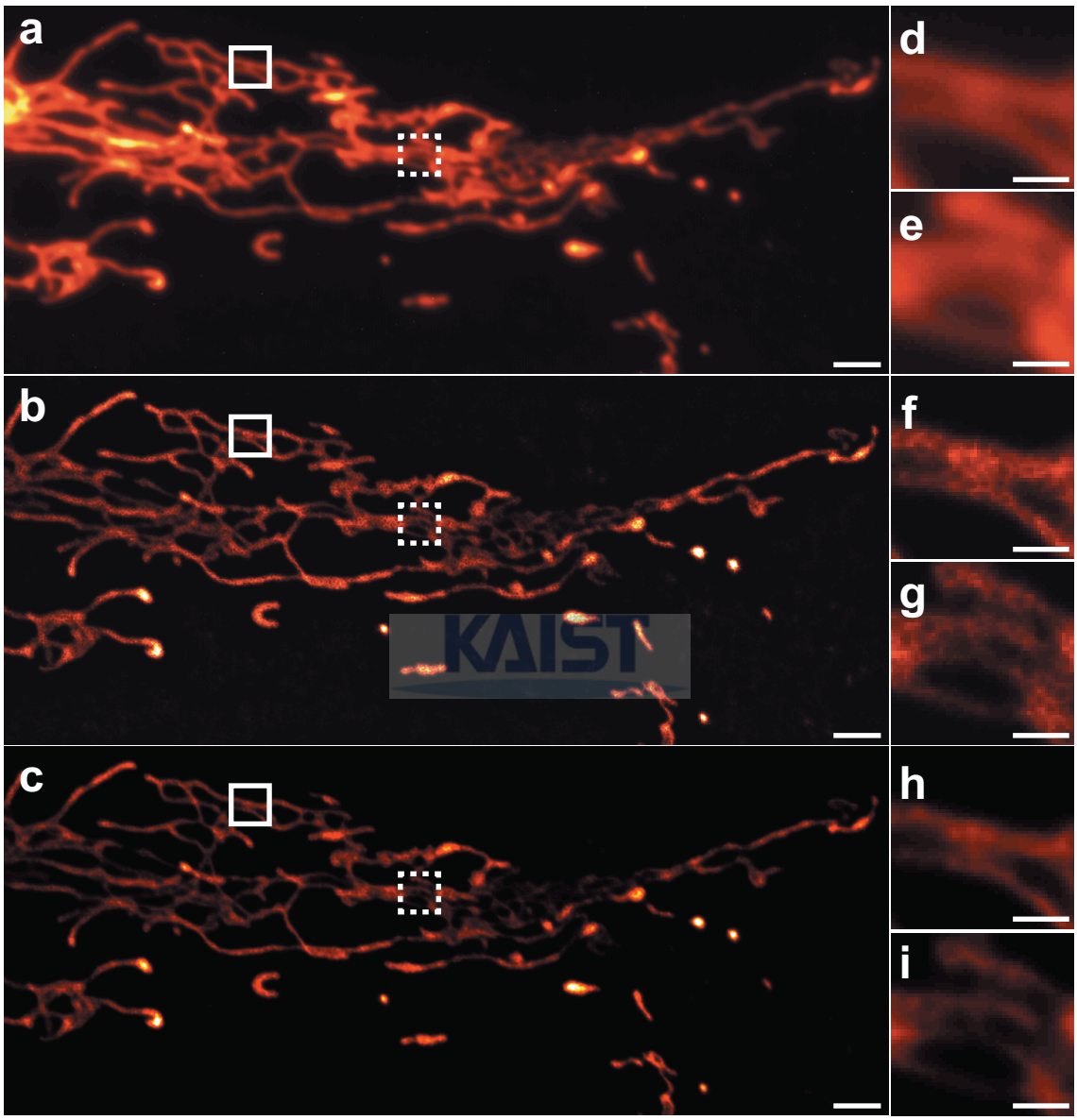

Figure 6.16: The experimental result of mitochondria stained of inner membrane with a fluorescent protein (DsRed-mito). (a) Conventional image generated by a mean image of measured snapshots. (b) l_∞-MUSIC reconstruction image of (a). (c) l_2-MUSIC reconstruction image of (a). (d, f, and h) Magnified images of the white line boxes in (a-c). (e, g, and i) Magnified images of the white dash line boxes in (a-c). Scale bars in (a-c) and (d-i) are $2\mu m$ and $500nm$, respectively.

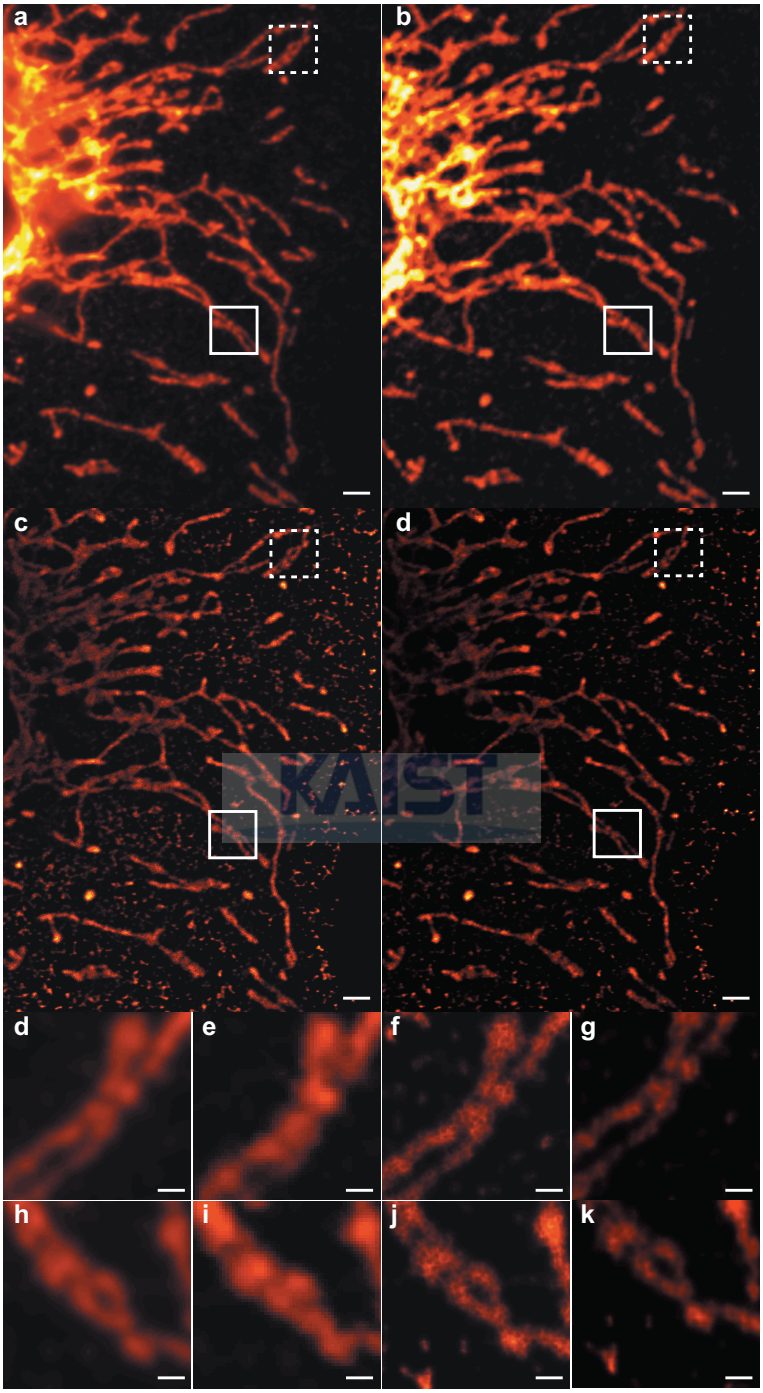

Figure 6.17: The experimental result of mitochondria stained of cytochrome-c with a fluorescent dye. (a) Conventional image generated by a mean image of measured snapshots. (b) Confocal image of (a). (c) l_∞-MUSIC reconstruction image of (a). (d) l_2-MUSIC reconstruction image of (a). (d-g) Magnified images of the white line boxes in (a-d). (h-k) Magnified images of the white dash line boxes in (a-d). Scale bars in (a-d) and (d-k) are $2\mu m$ and $500nm$, respectively.

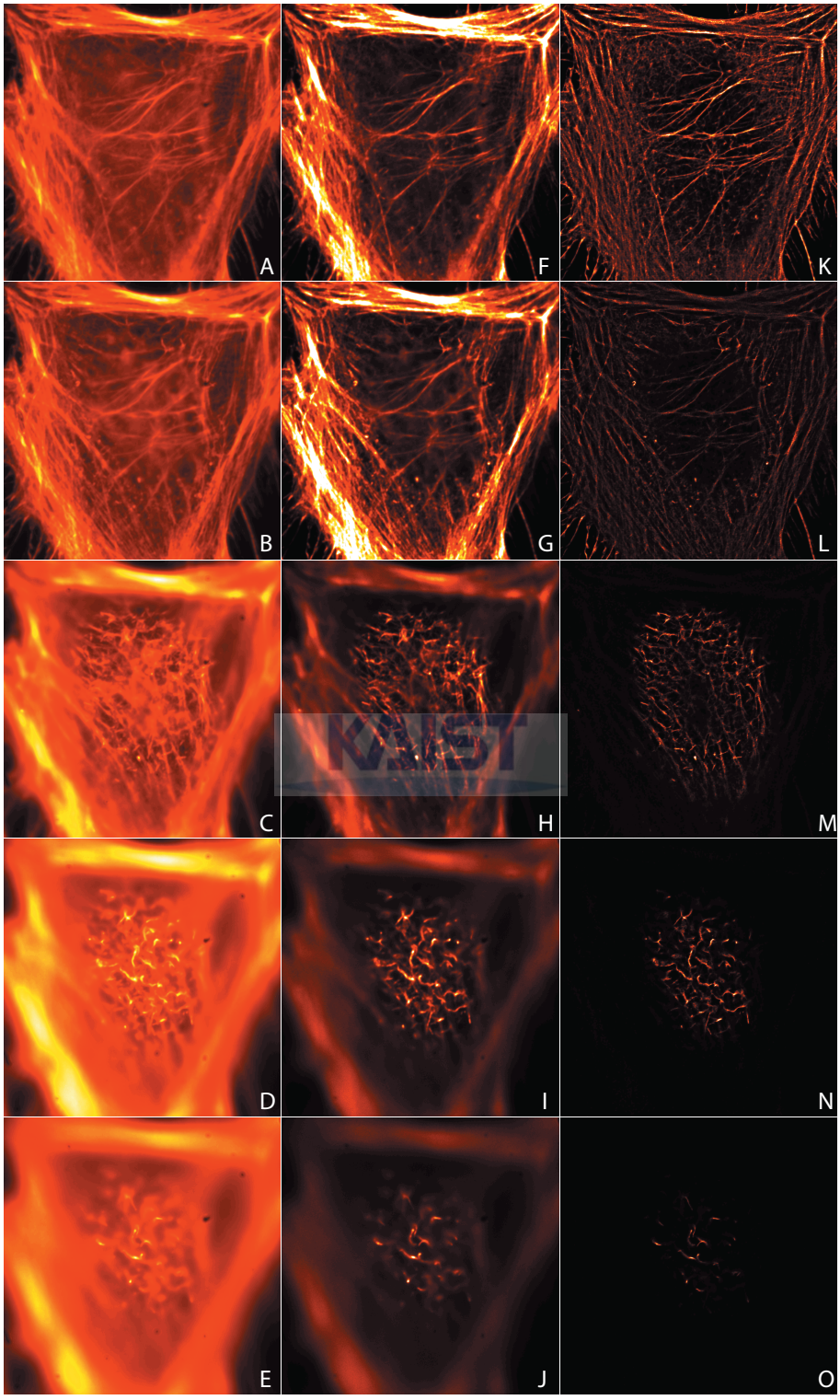

Figure 6.18: The experimental result of F-actin stained with a fluorescent dye. (A-E) Conventional image from $1\mu m$ z-axis scanning. (F-J) Conventional image generated by variance from $1\mu m$ z-axis scanning. (K-O) l_2-MUSIC reconstruction image of (A-E).

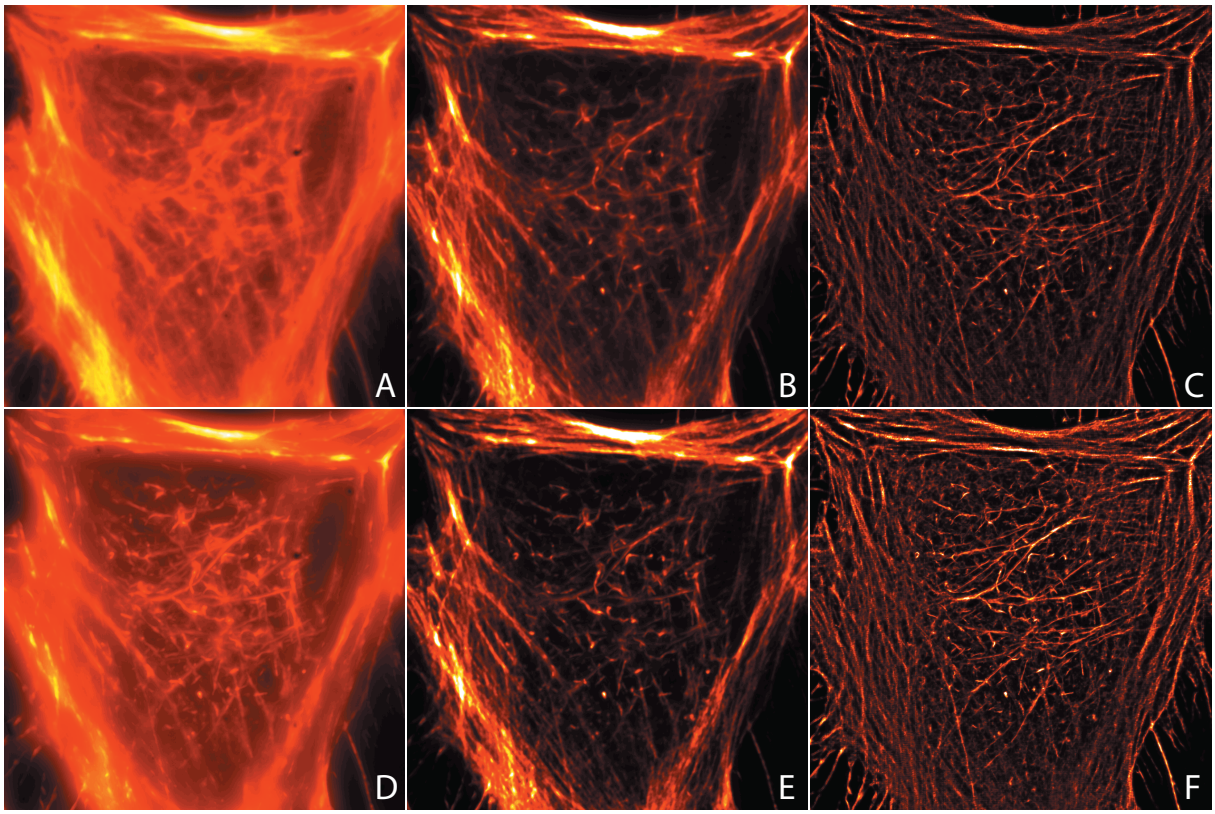

Figure 6.19: The experimental result of F-actin stained with a fluorescent dye. (A-C) Conventional image generated by mean of stack images. (D-F) Projection image generated by maximum of stack images.

KAIST

Chapter 7. Conclusion

7.1 Summary

In this thesis, we developed nanometer resolution microscopy for cellular imaging. Depending on the imaging physics of cells, we proposed a novel quantitative phase imaging microscopy and nanometer resolution fluorescence microscopy. To acquire accurate quantitative phase imaging, we developed a novel self-reference interferometry using extended depth-of-focus optics. To minimize heterogeneous phase noise in the conventional interferometric optics, we proposed a novel self-reference interferometry modifying the Michelson interferometry. The reference field was generated by inverting the relative position of the sample and the background images. Based on the proposed self-reference interferometry, two types of optical setup, PSI and HPM, were developed. Our PSI setup allowed quantitative phase measurements for an increased depth-of-field without scanning the objective lens or the specimen, whereas our HPM setup significantly reduced the phase noise thanks to the two simultaneously measured phase maps. We demonstrated the proposed quantitative phase microscopy using polymer beads, RBCs, and bovine embryos.

KAIST

Table 7.1: Characteristics of the conventional nanoscopy [67] and Nano-MUSIC

	STED	SSIM	PALM/STORM	Nano-MUSIC
Lateral Resolution	20-100nm	50nm	20-50nm	65nm
Image acquision time	$<$ 10 min ($\propto$ image size)	$<$ 10 min ($\propto$ no. of patterns)	$<$ 10 min ($\propto$ no. of probes)	$<$ 2 min (1000 images)
Multi-color imaging	2	1	2	Unlimited
Fluorescence dye	Photostable	Photostable	Photoswitchable	Unlimited
Compatible microscopy	STED microscopy	Interferometry	TIRFM	Conventional Microscopy
Laser	Ultra high power (100$\sim$1000MW)	High power ($\sim$50MW)	High power ($\sim$30W)	Low power ($<$100mW)
Photobleaching	Yes	Yes	Yes	No
Postprocessing	No	Yes	Yes	Yes

We presented a novel far-field nanoscopy using speckle illumination and multiple signal classification (nano-MUSIC). Nano-MUSIC has achieved sub-diffraction imaging without non-linear properties of optical elements or fluorescence phenomena that are applied for the conventional nanoscopy. Unlike the localization based nanoscopy, nano-MUSIC does not require photoswitchable dyes since the tempo-

ral separation of fluorescence emission can be obtained by spatial incoherence of speckle illumination. Moreover, we have additional advantages compared to the conventional nanoscopy summarized in Table 7.1. STED microscopy and SSIM are representative methods by using a PSF shaping method, and PALM/STORM are based on single molecule imaging technique. We demonstrated sub-diffraction resolution up to $65nm$ with the conventional fluorescent probes and proteins for biological and non-biological samples. Although STED microscopy achieved $20nm$ lateral resolution, it needs a $1GW/cm^2$ ultra high power laser for de-excitation, and PALM/STORM have to apply photoswitchable dye and TIRFM to achieve $20nm$ lateral resolution. These imaging physics of the conventional nanoscopy techniques damaged the fluorescence dyes due to the high laser power or multiple acquisition. Moreover, multi color imaging of STED microscopy and PALM/STORM is realized with two colors, but further extension to three colors is restricted by requirement of non-overlapping fluorescence spectrums such as excitation, emission, and de-excitation bands.

Nano-MUSIC is implemented by simply modifying the conventional epi-fluorescence optical microscopy and applying a signal array processing method. From multiple snapshots we separated the fluorescence emission of fluorescence probes within the diffraction limit, where for each imaging cycle, the rotatable diffusor forms incoherent speckle patterns. However, these patterns blurred when they passed through illumination optics, and then the fluorescence probes are excited proportional to speckle patterns. Thus, the signal correlation matrix does not satisfy the best CRB condition, and therefore we proposed l_∞-MUSIC algorithm to improve the resolution. To demonstrate nano-MUSIC, we applied nano particles, nano-patterns, and biological samples such as F-actin, ER, and mitochondrial networks of HeLa cells. Based on nano-particle experimental results, we resolved a $65nm$ single particle that is the minimum resolvable size until now. In ER, we could reveal ultra structures that were not seen using the conventional microscopy.

7.2 Future directions

7.2.1 Multi-color imaging

One of the advantages of the conventional fluorescence microscopy finds out the relationship of various organelles or proteins showing a variety of fluorescence color images. This is also true for nanoscopy and has become one of the major issues. As illustrated in previous Chapter we reconstructed mitochondria networks of the outer and the inner membranes. We did not confirm any relationship between the outer and the inner membranes since we only achieved single color images for the outer and the inner membranes, separately. To overcome the limitation of a single color imaging, STED, SIM, and PALM/STORM realized multi-color imaging systems [59, 60, 62]. As illustrated in Fig. 7.1, to achieve nanometer resolution image, STED and PALM/STORM have to apply non-linear properties of fluorescence probes, which need four-color lasers for two-color image due to the saturation and excitation

processes of each fluorescence probes. In visible light range, their extension could be restricted by the requirements of non-overlapping fluorescence spectrums such as excitation, emission, and de-excitation bands.

In the nano-MUSIC, it is easy to extend multi-color imaging since it does not require specialized fluorescence dyes. Thus, as illustrated in Fig. 7.2, nano-MUSIC can acquire nanometer resolution multi-color image by adding multi-color lasers with dichromatic mirrors, and then the number of observable multi fluorescence color images is equal to the number of the conventional fluorescence microscopy.

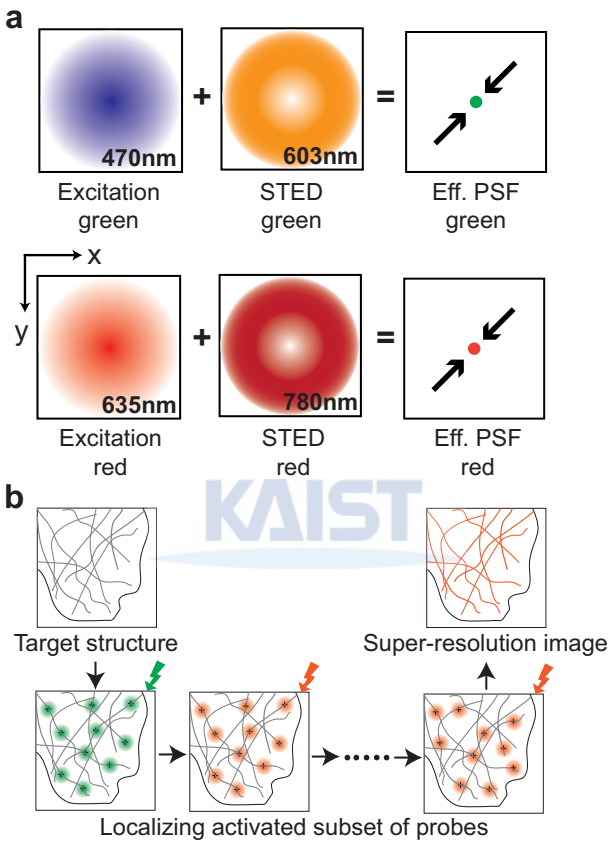

Figure 7.1: (a) STED needs four color laser systems to acquire two-color images, (b) PALM/STORM needs two-color laser systems for a single fluorescence color image.

7.2.2 Multi-dimensional imaging

The temporal resolution of optical microscopy limits the dynamic information of a cellular process. In the conventional nanoscopy, the total image acquisition time is slower than the conventional optical microscopy. First, STED has a nanoscale PSF up to $16nm$ in lateral and $50nm$ in axial resolutions and inherently takes longer time than confocal microscopy for scanning through the same area of specimen. To increase the imaging speed, STED restricted the field of view to a few micrometer. Westphal and his colleagues [68] have observed Brownian motion of a dense suspension of nano particles with rate of 80 fps (frames per second) using STED microscopy. Recently, they have demonstrated video rate (28

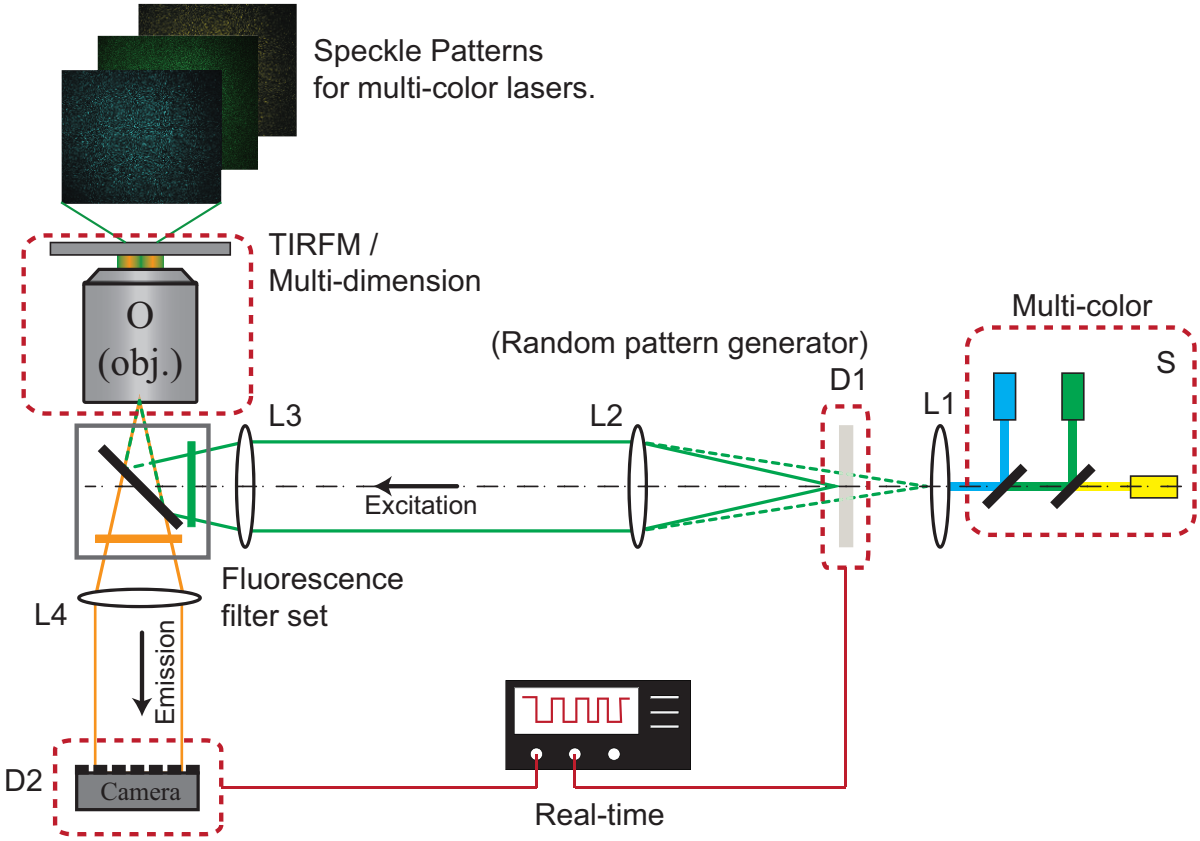

Figure 7.2: Nano-MUSIC system can further extends to multi-color, multi-dimension and real-time imaging systems. Moreover, by exploiting near-field illumination optics such as TIRFM, we can improve the resolution of the system.

fps) imaging speed in a $2.5\mu m \times 1.8\mu m$ field of view visualizing live hippocampal neurons and individual synaptic vesicles within $60 \sim 80nm$ resolution [69]. Single molecule localization approaches such as PALM/STORM take a few minutes of total image acquisition time in general since the final super resolution image is reconstructed from few thousand images mapping of single fluorophore positions. A temporal resolution of $25 \sim 60$ seconds per frame was obtained to acquire focal adhesion proteins in live cells [70], and in this case, approximately 103 fluorescence probes were observe in $1\mu m \times 1\mu m$ area with $60 \sim 70nm$. Consequently, the temporal resolution in the conventional nanoscopy is highly dependent on the characteristics of specimen such as field of view and the number of fluorescence probes.

The temporal resolution of nano-MUSIC can be further improved. Until now, our system took almost two minutes for 1000 snapshots. In the nano-MUSIC system, if we apply a fast camera and electrical diffusor, we can achieve total imaging acquisition time of a few seconds. The electrical diffusors can be obtained using a spatial light modulator (SLM) and a digital micro-mirror device (DMD). The recent technology of DMD has achieved the switching speed up to 8kHz. Based on this, the imaging frame rate is highly dependent on the detector performance. Recently, high speed EMCCDs are introduced with the frame rate of 513Hz. If we apply these instruments, we can achieve total imaging acquisition

time of a few seconds without reduction of field-of-view ($19\mu m \times 19\mu m$ in 160X magnification). Thus compared to the conventional nanoscopy, the imaging speed of nano-MUSIC is highly dependent on the performance of instruments such as diffusor and detector. As mentioned earlier, nano-MUSIC does not have any limitations on *in-vivo* imaging since we do not need specialized fluorescence dyes. Then, if we increase imaging speed, we can observe dynamic characteristics of cells.

Most cellular structures are 3-dimensional, and the optical resolution to resolve an axial direction is also limited by diffraction limit. Therefore, the improvement of axial resolution is important to visualize the cellular structures. In STED, the aligned two beams formed the nanoscale effective PSF in lateral resolution. In addition, the dual lens optical imaging systems called iso-STED is realized to achieve maximum $20nm$ axial resolution [58]. In this case, the precise aligned two STED beams are focused on specimen passing through two opposite objective lenses. The complexity of this optical system is higher than the conventional STED system. Three dimensional imaging using the single-molecule localization approach such as STORM was also realized by optical technique, and was first implemented using the astigmatism method for axial localization. This technique inserts a cylindrical lens in the imaging optics so that the observed image is focused differently on the lateral directions. The image of a fluorescence probe becomes elliptic shape estimating its axial location from the ellipticity and the lateral location from the centroid of the elliptic. Consequently, it has achieved a lateral localization accuracy up to 25 nm and an axial localization accuracy up to 50 nm. SSIM was only demonstrated in two dimensions up to date, while the linear SIM was implemented to achieve $100nm$ lateral and $300nm$ axial resolutions, simultaneously.

In the nano-MUSIC, we now demonstrated a nanometer resolution imaging in a lateral direction. To achieve a 3-D imaging mode, we confirmed the performance of optical sectioning as show in Fig. 6.18. It was obtained by manually manipulating of mechanical stage by $1\mu m$ increments. The reconstruction results outperformed compared to the conventional microscopy and the conventional optical sectioning method using speckle illumination [37, 38, 39, 40]. The conventional optical sectioning microscopy using speckle illumination is based on incoherency of speckle pattern in axial direction. They calculated the effect of incoherency of random speckle patterns, and then removed the coherence effects by subtraction of measured images. Its performance is measured and calculated as $\sim 2\mu m$ in big NA lens with high refractive index materials. Nano-MUSIC improved the axial resolution up to $1\mu m$ in current nano-MUSIC system. According to the nano-MUSIC reconstruction results, we expect the axial resolution of nano-MUSIC can be achieved higher than $1\mu m$ since array signal processing technique removes the interference from out-of-focus planes. Therefore, to characterize axial resolution of nano-MUSIC, we have to exploit the motorized precision z-axis stage. The ultimate performance of axial resolution in the nano-MUSIC is also achieved to reduce the coherence of speckle pattern in axial direction. To achieve it, we can exploit various techniques such as near-field illumination or dual-lens optics. In the conventional nanoscopy, dual lens optical systems such as $\mathbf{I}^5\mathbf{M}$ or 4Pi is often combined with interferometric configurations to

achieve nanometer axial resolution. In 4Pi configuration, it extends the concept of confocal microscopy by having two precisely aligned identical objective lenses act as a single lens to achieve $80nm$ axial resolution [71, 72]. Similar to 4Pi, $\mathbf{I}^5\mathbf{M}$ microscopy achieved $< 100nm$ due to the double sided illumination and detection by opposing objective lenses in wide-field microscopy [72, 73]. Although these methods need extremely precise alignment of optical system, it can significantly reduce the axial point spread function. The effect of near-field illumination will be discuss in next Section.

7.2.3 Resolution improvement

As we discussed in Chapter 5, the performance of MUSIC algorithm is dependent on the structure of signal correlation matrix. When the fluorescence emissions of fluorophores are uncorrelated, the correlation matrix becomes diagonal matrix, and then the performance approaches to the single molecule imaging technique. Specifically PALM/STORM satisfies the condition $\overline{< \mathbf{x}_i(t), \mathbf{x}_j(t) >} = 0$ for $i \neq j$ due to the non-overlapping photoswitching fluorophores and total internal reflection (TIR) illumination. Single molecule localization approaches generally exploit TIR illumination techniques with weak illumination. Hence, when the signal correlation matrix is diagonal, the arrays signal processing theory guarantees that its fundamental performance limitation approaches to that of single target detection; hence it approaches the accuracy of single molecule imaging. These approaches require specialized fluorescence dye or proteins to generate the diagonal signal correlation matrix.

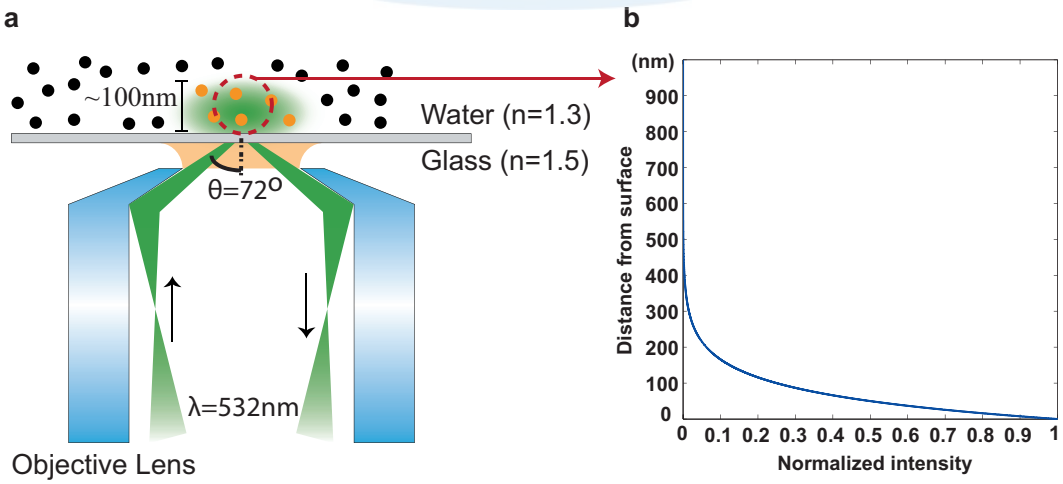

Figure 7.3: (a) Objective lens type of TIR illumination, (b) the normalized intensity along with perpendicular distance from glass surface. If we exploit the TIRFM instead of far-field optical system in Fig. 7.2, the effect of signal correlation matrix should be reduced in the nano-MUSIC.

In total internal reflection microscopy (TIRFM), the evanescent wave at near-field is generated by total internal reflection phenomena. TIR illumination can be implemented by objective lens as shown in Figs. 7.3(a). To occur total internal reflection, the incident angle (θ) should be larger than critical angle

($\theta_c = \sin^{-1}(n_{water}/n_{glass}) = 60^o$). The intensity distribution of evanescent wave is simply defined [56] :

$$I(z) = I(0)e^{-z/d}, \tag{7.1}$$

where

$$d = \frac{\lambda}{4\pi}(n_{glass}^2 \sin^2(\theta) - n_{water}^2)^{-1/2}, \tag{7.2}$$

where z and θ are the perpendicular distance from surface and an incident angle, respectively. The intensity profile of evanescent wave for the conditions of Fig 7.3(a) is exponentially decreased along with perpendicular distance from glass surface as illustrated in Fig. 7.3(b). The limited illumination depth ($\ll \lambda$) is helpful to excite surface bounded fluorescence dyes [56] and achieves very low unwanted fluorescence signals from background and defocused planes.

In the nano-MUSIC, the signal correlation matrix has off-diagonal elements due to the diffraction limit of the far-field illumination optics as described in Chapter 4. When the fully uncorrelated speckle patterns are passing through the illumination optics in the conventional microscopy, the patterns are convolved with point spread function of the illumination optics and disturb the ultimate performance of nano-MUSIC. Thus to improve nano-MUSIC performance in lateral and axial directions, near-field illumination techniques such as TIR should be implemented. Even though we proposed l_∞-MUSIC algorithm to overcome the limitation of the conventional MUSIC algorithm in the nano-MUSIC system, its performance is still affected by the structure of signal correlation matrix. Since in TIR illumination as shown in Fig. 7.3 the speckle patterns from the evanescent wave should be sub-diffraction limit, TIRFM can reduce the off-diagonal size in the signal correlation matrix to achieve fundamental lower bound characterized by single molecule imaging.

KAIST

References

[1] Hooke, R., [*Micrographia*], Octavo (1998).

[2] Leeuwenhoek, A., [*The Select Works of Antony Van Leeuwenhoek: Containing His Microscopical Discoveries in Many of the Works of Nature*], Translated by Samuel Hoole. New York: Arno Press (1977).

[3] Murphy, D. B., [*Fundamentals of Light Microscopy and Electronic Imaging*], Wiley-Liss, 1st ed. (2001).

[4] Popescu, G., Deflores, L. P., Vaughan, J. C., Badizadegan, K., Iwai, H., Dasari, R. R., and Feld, M. S., "Fourier phase microscopy for investigation of biological structures and dynamics," *Opt. Lett.* **29**(21), 2503–2505 (2004).

[5] Ikeda, T., Popescu, G., Dasari, R. R., and Feld, M. S., "Hilbert phase microscopy for investigating fast dynamics in transparent systems," *Opt. Lett.* **30**(10), 1165–1167 (2005).

[6] Warger, II, W. C. and Dimarzio, C. A., "Computational signal-to-noise ratio analysis for optical quadrature microscopy," *Optics Express* **17**, 2400–2422 (2009).

[7] Marquet, P., Rappaz, B., Magistretti, P. J., Cuche, E., Emery, Y., Colomb, T., and Depeursinge, C., "Digital holographic microscopy: a noninvasive contrast imaging technique allowing quantitative visualization of living cells with subwavelength axial accuracy," *Opt. Lett.* **30**(5), 468–470 (2005).

[8] Popescu, G., Ikeda, T., Dasari, R. R., and Feld, M. S., "Diffraction phase microscopy for quantifying cell structure and dynamics," *Opt. Lett.* **31**(6), 775–777 (2006).

[9] "Milestones in light microscopy," *Nature Cell Biology* **11**(10), 1165 (2009).

[10] Heimstädt, O., "Das fluoreszenzmikroskop," *Z Wiss Mikrosk* **28**, 330–337 (1911).

[11] Ellinger, P. and Hirt, A., "Mikroskopische Beobachtungen an lebenden Organen mit Demonstrationen (Intravitalmikroskopie)," *Naunyn-Schmiedeberg's Archives of Pharmacology* **147**(1), 63–63 (1929).

[12] Ploem, J. S., "The use of a vertical illuminator with interchangeable dichroic mirrors for fluorescence microscopy with incident light," *Z. Wiss. Mikrosk.* **68**(3), 129–142 (1967).

[13] Coons, A. H., Creech, H. J., and Jones, R. N., "Immunological properties of an antibody containing a fluorescent group," *Proc Soc Exp Biol Med* **47**, 200–202 (1941).

KAIST

[14] Chalfie, M., Tu, Y., Euskirchen, G., Ward, W. W., and Prasher, D. C., "Green fluorescent protein as a marker for gene expression," *Science* **263**(5148), 802 (1994).

[15] Matz, M. V., Fradkov, A. F., Labas, Y. A., Savitsky, A. P., Zaraisky, A. G., Markelov, M. L., and Lukyanov, S. A., "Fluorescent proteins from nonbioluminescent Anthozoa species," *Nature Biotechnology* **17**(10), 969–973 (1999).

[16] Abbe, E., "Beiträge zur Theorie des Mikroskops und der mikroskopischen Wahrnehmung," *Archiv für Mikroskopische Anatomie* **9**(1), 413–418 (1873).

[17] Klar, T. A., Jakobs, S., Dyba, M., Egner, A., and Hell, S. W., "Fluorescence microscopy with diffraction resolution barrier broken by stimulated emission," *Proceedings of the National Academy of Sciences of the United States of America* **97**(15), 8206–8210 (2000).

[18] Gustafsson, M. G. L., "Nonlinear structured-illumination microscopy: Wide-field fluorescence imaging with theoretically unlimited resolution," *Proceedings of the National Academy of Sciences of the United States of America* **102**(37), 13081 (2005).

[19] Cheezum, M. K., Walker, W. F., and Guilford, W. H., "Quantitative comparison of algorithms for tracking single fluorescent particles," *Biophysical Journal* **81**(4), 2378–2388 (2001).

[20] Thompson, R. E., Larson, D. R., and Webb, W. W., "Precise nanometer localization analysis for individual fluorescent probes," *Biophysical Journal* **82**(5), 2775–2783 (2002).

[21] Yildiz, A., Forkey, J. N., McKinney, S. A., Ha, T., Goldman, Y. E., and Selvin, P. R., "Myosin v walks hand-over-hand: single fluorophore imaging with 1.5-nm localization," *Science* **300**(5628), 2061 (2003).

[22] Lidke, K., Rieger, B., Jovin, T., and Heintzmann, R., "Superresolution by localization of quantum dots using blinking statistics," *Optics Express* **13**(18), 7052–7062 (2005).

[23] Dertinger, T., Colyer, R., Iyer, G., Weiss, S., and Enderlein, J., "Fast, background-free, 3D super-resolution optical fluctuation imaging (SOFI)," *Proceedings of the National Academy of Sciences of the United States of America* **106**(52), 22287 (2009).

[24] Betzig, E., Patterson, G. H., Sougrat, R., Lindwasser, O. W., Olenych, S., Bonifacino, J., Davidson, M. W., Lippincott-Schwartz, J., and Hess, H. F., "Imaging intracellular fluorescent proteins at nanometer resolution," *Science* **313**(5793), 1642 (2006).

[25] Rust, M. J., Bates, M., and Zhuang, X., "Sub-diffraction-limit imaging by stochastic optical reconstruction microscopy (STORM)," *Nature Methods* **3**(10), 793–796 (2006).

[26] Krim, H. and Viberg, M., "Two decades of array signal processing research: the parametric approach," *IEEE Signal Processing Magazine* **13**(4), 67–94 (1996).

KAIST

[27] Schmidt, R., "Multiple emitter location and signal parameter estimation," *IEEE Transactions on Antennas and Propagation* **34**(3), 276–280 (1986).

[28] Yau, S. and Bresler, Y., "Worst case Cramer-Rao bounds for parametric estimation of superimposed signals with applications," *IEEE Transactions on Signal Processing* **40**(12), 2973–2986 (1992).

[29] Yau, S. and Bresler, Y., "A compact Cramer-Rao bound expression for parametric estimation of superimposed signals," *Signal Processing, IEEE Transactions on* **40**(5), 1226–1230 (1992).

[30] Stoica, P. and Arye, N., "MUSIC, maximum likelihood, and Cramer-Rao bound," *IEEE Transactions on Acoustics, Speech and Signal Processing* **37**(5), 720–741 (1989).

[31] Kay, S. M., [*Fundamentals of statistical signal processing: estimation theory*], Prentice-Hall Signal Processing Series (1993).

[32] Waterman-Storer, C. M. and Salmon, E. D., "Actomyosin-based retrograde flow of microtubules in the lamella of migrating epithelial cells influences microtubule dynamic instability and turnover and is associated with microtubule breakage and treadmilling," *The Journal of Cell Biology* **139**(2), 417 (1997).

[33] Waterman-Storer, C. M. and Salmon, E. D., "How microtubules get fluorescent speckles," *Biophysical Journal* **75**(4), 2059–2069 (1998).

[34] Danuser, G. and Waterman-Storer, C. M., "Quantitative fluorescent speckle microscopy: where it came from and where it is going," *Journal of Microscopy* **211**(3), 191–207 (2003).

[35] Rodriguez, O. C., Schaefer, A. W., Mandato, C. A., Forscher, P., Bement, W. M., and Waterman-Storer, C. M., "Conserved microtubule–actin interactions in cell movement and morphogenesis," *Nature Cell Biology* **5**(7), 599–609 (2003).

[36] Hu, K., Ji, L., Applegate, K. T., Danuser, G., and Waterman-Storer, C. M., "Differential transmission of actin motion within focal adhesions," *Science* **315**(5808), 111 (2007).

[37] Walker, J. G., "Non-scanning confocal fluorescence microscopy using speckle illumination," *Optics Communications* **189**(4-6), 221–226 (2001).

[38] Ventalon, C. and Mertz, J., "Quasi-confocal fluorescence sectioning with dynamic speckle illumination," *Optics Letters* **30**(24), 3350–3352 (2005).

[39] Ventalon, C. and Mertz, J., "Dynamic speckle illumination microscopy with translated versus randomized speckle patterns," *Optics Express* **14**(16), 7198–7209 (2006).

[40] Ventalon, C., Heintzmann, R., and Mertz, J., "Dynamic speckle illumination microscopy with wavelet prefiltering," *Optics Letters* **32**(11), 1417–1419 (2007).

[41] Choi, W., Fang-Yen, C., Badizadegan, K., Oh, S., Lue, N., Dasari, R. R., and Feld, M. S., "Tomographic phase microscopy," *Nature Methods* **4**, 717–719 (Sept. 2007).

[42] Su, Y.-D., Chen, S.-J., and Yeh, T.-L., "Common-path phase-shift interferometry surface plasmon resonance imaging system," *Opt. Lett.* **30**(12), 1488–1490 (2005).

[43] Botcherby, E., Juskaitis, R., Booth, M., and Wilson, T., "An optical technique for remote focusing in microscopy," *Optics Communications* **281**(4), 880 – 887 (2008).

[44] Hwang, H., Kang, G., Yeon, J. H., Nam, Y., and Park, J.-K., "Direct rapid prototyping of PDMS from a photomask film for micropatterning of biomolecules and cells," *Lab Chip* **9**, 167–170 (2009).

[45] Bliss, C. L., McMullin, J. N., and Backhouse, C. J., "Rapid fabrication of a microfluidic device with integrated optical waveguides for DNA fragment analysis," *Lab Chip* **7**, 1280–1287 (2007).

[46] Valadão, G. and Bioucas-Dias, J., "CAPE: combinatorial absolute phase estimation," *J. Opt. Soc. Am. A* **26**(9), 2093–2106 (2009).

[47] El-Ali, J., Sorger, P. K., and Jensen, K. F., "Cells on chips," *Nature* **442**, 403–411 (2006).

[48] Dittrich, P. S. and Manz, A., "Lab-on-a-chip: microfluidics in drug discovery," *Nat Rev Drug Discov* **5**, 210–218 (2006).

KAIST

[49] Lee, S., Lee, J. Y., Yang, W., and Kim, D. Y., "Autofocusing and edge detection schemes in cell volume measurements with quantitative phase microscopy," *Opt. Express* **17**(8), 6476–6486 (2009).

[50] Karlsson, A., He, J., Swartling, J., and Andersson-Engels, S., "Numerical simulations of light scattering by red blood cells," *IEEE Transactions on Biomedical Engineering* **52**(1), 13–18 (2005).

[51] Kim, M. S., Bae, C. Y., Wee, G., Han, Y.-M., and Park, J.-K., "A microfluidic *in vitro* cultivation system for mechanical stimulation of bovine embryos," *Electrophoresis* **30**(18), 3276–3282 (2009).

[52] Warger, II, W. C., Newmark, J. A., Warner, C. M., and DiMarzio, C. A., "Phase-subtraction cell-counting method for live mouse embryos beyond the eight-cell stage," *Journal of Biomedical Optics* **13**(3), 034005 (2008).

[53] Edidin, M., "Near-field scanning optical microscopy, a siren call to biology," *Traffic* **2**(11), 797–803 (2001).

[54] Walker, K., Doak, S., and Dunstan, P., "Mechanisms of cell-cell adhesion identified by immunofluorescent labelling with quantum dots: A scanning near-field optical microscopy approach," *Ultramicroscopy* (2011).

[55] Lewis, A., Radko, A., Ami, N. B., Palanker, D., and Lieberman, K., "Near-field scanning optical microscopy in cell biology," *Trends in cell biology* **9**(2), 70–73 (1999).

[56] Axelrod, D., "Total internal reflection fluorescence microscopy in cell biology," *Traffic* **2**(11), 764–774 (2001).

[57] Hofmann, M., Eggeling, C., Jakobs, S., and Hell, S., "Breaking the diffraction barrier in fluorescence microscopy at low light intensities by using reversibly photoswitchable proteins," *Proceedings of the National Academy of Sciences of the United States of America* **102**(49), 17565 (2005).

[58] Schmidt, R., Wurm, C., Jakobs, S., Engelhardt, J., Egner, A., and Hell, S., "Spherical nanosized focal spot unravels the interior of cells," *Nature methods* **5**(6), 539–544 (2008).

[59] Donnert, G., Keller, J., Wurm, C., Rizzoli, S., Westphal, V., Schönle, A., Jahn, R., Jakobs, S., Eggeling, C., and Hell, S., "Two-color far-field fluorescence nanoscopy," *Biophysical journal* **92**(8), L67–L69 (2007).

[60] Schermelleh, L., Carlton, P. M., Haase, S., Shao, L., Winoto, L., Kner, P., Burke, B., Cardoso, M. C., Agard, D. A., Gustafsson, M. G. L., et al., "Subdiffraction multicolor imaging of the nuclear periphery with 3d structured illumination microscopy," *Science* **320**(5881), 1332 (2008).

[61] Huang, B., Jones, S. A., Brandenburg, B., and Zhuang, X., "Whole-cell 3D STORM reveals interactions between cellular structures with nanometer-scale resolution," *Nature Methods* **5**(12), 1047–1052 (2008).

[62] Bates, M., Huang, B., Dempsey, G., and Zhuang, X., "Multicolor super-resolution imaging with photo-switchable fluorescent probes," *Science* **317**(5845), 1749 (2007).

[63] Goodman, J. W., [*Speckle phenomena in optics: theory and applications*], Roberts & Company (2007).

[64] Kailath, T., [*Linear systems*], vol. 1, Prentice-Hall Englewood Cliffs, NJ (1980).

[65] Cooper, G. M. and Hausman, R. E., [*The cell: a molecular approach*], Sinauer Associates Inc (2007).

[66] Becker, W. M., Kleinsmith, L. J., Hardin, J., and Bertoni, G. P., [*The world of the cell*], Benjamin-Cummings Pub Co (2008).

[67] Schermelleh, L., Heintzmann, R., and Leonhardt, H., "A guide to super-resolution fluorescence microscopy," *The Journal of cell biology* **190**(2), 165 (2010).

[68] Westphal, V., Lauterbach, M. A., Di Nicola, A., and Hell, S. W., "Dynamic far-field fluorescence nanoscopy," *New Journal of Physics* **9**, 435 (2007).

[69] Westphal, V., Rizzoli, S. O., Lauterbach, M. A., Kamin, D., Jahn, R., and Hell, S. W., "Video-rate far-field optical nanoscopy dissects synaptic vesicle movement," *Science* **320**(5873), 246 (2008).

KAIST

[70] Shroff, H., Galbraith, C. G., Galbraith, J. A., and Betzig, E., "Live-cell photoactivated localization microscopy of nanoscale adhesion dynamics," *Nature Methods* **5**(5), 417–423 (2008).

[71] Egner, A., Verrier, S., Goroshkov, A., Soling, H., and Hell, S. W., "4pi-microscopy of the golgi apparatus in live mammalian cells," *Journal of structural biology* **147**(1), 70–76 (2004).

[72] Bewersdorf, J., Schmidt, R., and Hell, S. W., "Comparison of i5m and 4pi-microscopy," *Journal of microscopy* **222**(2), 105–117 (2006).

[73] Gustafsson, M. G., Agard, D. A., and Sedat, J. W., "I5m: 3d widefield light microscopy with better than 100 nm axial resolution.," *Journal of microscopy* **195**(Pt 1), 10 (1999).

KAIST

Summary

Nanometer Resolution Fluorescence Microscopy using Speckle Illumination and Array Signal Processing

본 논문은 세포 영상화를 위한 광학 현미경에 대한 것으로서 기존 광학계의 한계를 넘고자 한다. 세포를 명시야에서 관찰해보면 투명해서 구조를 관찰하기 힘들고 소기관들은 수백 나노미터이하 크기로 되어있어서 이를 관찰하기에는 광학계의 회절한계에 부딪히게 된다. 기존 광학 현미경에서 세포를 관찰하는 방법은 위상 현미경과 형광 현미경을 이용하여 관찰이 가능하다. 위상 현미경의 경우 세포 내부의 굴절률이 균일하지 않고 각 기관의 크기 및 세포의 두께가 균일하지 못해서 발생하는 위상차를 염색을 하지 않고 실시간으로 관찰 가능하다는 장점이 있다. 하지만 기존 위상 현미경의 경우 정성적인 영상만을 제공하기 때문에 최근에 정량적 위상 현미경에 대한 연구가 활발히 이루어지고 있다. 간섭계를 기반으로 하는 정량적 위상 현미경의 경우 시편에 의한 위상 지연이 광학계의 정밀도에 의존하게 된다. 따라서 광학적 구성이 간단하여 빛의 경로차에 따른 잡음 발생이 최소화되는 자기기준을 가지는 간섭계를 이용하여 새로운 정량적 위상차 현미경을 제안하였다. 제안된 방법은 확장된 심도의 구현이 가능하여 초점이 맞지 않는 시편의 영상을 원거리에서 보정하여 깨끗한 정량적 위상 영상을 구현할 수 있다. 제안된 방법을 검증하기 위해서 마이크로 비드, PDMS 패턴과 마이크로 채널 내부에 존재하는 다양한 세포를 이용하였다. 형광 현미경은 세포 내부의 소기관이나 특정 단백질을 면역형광염색 방법을 이용하여 영상화한다. 특정 소기관 혹은 단백질에 대한 영상화가 가능하므로 세포내부에서 이러한 물질의 위치를 확인할 수 있으나 확인 가능한 크기는 회절한계를 넘어서지 못한다. 최근 10년간의 연구에서 이러한 회절한계를 뛰어넘는 초고해상도 영상화 기법들이 소개되었다. 대표적으로 STED 이나 PALM/STORM과 같은 방법들이 있으며 이러한 방법들은 세포 내부의 구조적 혹은 기능적 영상들을 수십나노미터의 해상도로 제공하였다. 하지만 이런한 방법들은 공통적으로 형광물질의 비선형적인 상태천이가 가능하거나 가능하게 만들기 위한 조건이 필수적이고 일반적이지 않은 광학계의 구성을 필요로 한다. 따라서 이러한 초고해상도 현미경이 널리 사용되기 위해서 일반적인 형광 물질 및 단백질과 기존의 형광 현미경을 활용한 방법이 요구된다. 제안한 스페클 조명과 배열 신호처리를 이용한 초고해상도 나노현미경은 이러한 조건들을 만족한다. 비선형 상태 천이를 가지는 형광물질들의 통계적 특성은 동적 스페클 조명을 이용하여 구현된다. 충분한 측정 영상들로부터 각 형광 신호들의 상관관계를 이용하여 배열 신호 처리 기법중 MUSIC 방법을 활용하여 신호원의 위치를 추정하므로서 영상 문제를 신호 검출 문제로 생각할 수 있게 하였다. 초고해상도 영상에서 발생할 수 있는 추정 오류를 보정하기 위해 l_∞-MUSIC을 제안하였고 제안한 나노현미경은 다양한 나노패턴과 세포들을 이용하여 검증하였다. 형광물질의 사용에 제한이 없으므로 다양한 면역염색방법과 형광 단백질들을 사용할 수 있었고 최대 65nm의 크기를 가지는 물체가 복원가능하다는 것을 보여주었다.

핵심어: 초고해상도, 나노스코피, 스페클, 배열신호처리